Resonant pickups for non-destructive single-particle detection in heavy-ion storage rings and first experimental results

DISSERTATION

zur Erlangung des Doktorgrades

der Naturwissenschaften

vorgelegt beim Fachbereich Physik
der Johann Wolfgang Goethe-Universität

von

Mohammad Shahab SANJARI

aus Kermanshah

Frankfurt am Main 2013
(D30)

Vom Fachbereich Physik
der Johann Wolfgang Goethe-Universität als Dissertation angenommen.

Dekan	:	Prof. Dr. Joachim Stroth
Gutachter	:	Prof. Dr. Alwin Schempp
	:	PD Dr. Peter Hülsmann
	:	Prof. Dr. Oliver Kester
Ext. Gutachter	:	Prof. Dr. Thomas Stöhlker
Datum der Disputation	:	26-04-2013

Contents

Kurzfassung

Resonante Pickups für zerstörungsfreien Nachweis einzelner Teilchen in Schwerionenspeicherringen und die ersten experimentellen Ergebnisse

Ein resonantes Pickup wurde konstruiert und im Experimentierspeicherring ESR an der GSI Darmstadt im Jahr 2010 installiert, ein ähnliches wurde im CSRe des Instituts für moderne Physik (IMP) in Lanzhou (China) eingebaut. Einzelteilchen mit 400 MeV pro Nukleon wurden erfolgreich mit dem GSI-Pickup nachgewiesen. Ähnliche Experimente sind für CSRe geplant. Diese Arbeit befasst sich mit der Theorie, Aufbau, Messung und Anwendung des Detektors in der Speicherring-Physik.

Motivation

In der nuklearen Astrophysik spielen Kenntnisse über Massen und Lebensdauer der Nuklide eine zentrale Rolle in der exakten Bestimmung der Reaktionsketten und Elementsynthese in den Sternen. Die Elementsynthese findet weit entfernt von der Region der stabilen Elemente statt, wo die meisten Nuklide kurzlebig sind.

Die Zerfallszeiten dieser Nuklide liefern Informationen über den weiteren Verlauf der Reaktionskette und sind daher astrophysikalisch von großer Bedeutung. Die meisten kurzlebigen Nuklide sind bereits gut erforscht. Die noch kurzlebigeren, die heute von großem Interesse sind, kann man jedoch nur mit Hilfe aufwendiger Prozesse herstellen, da sie nur in geringen Mengen produziert werden können und entsprechend eine kleine Statistik liefern. Das wiederum setzt voraus, dass der Detektor auch schnell und empfindlich genug ist, um Messungen durchzuführen.

Beschreibung des Experiments

Die kurzlebigen Nuklide werden in Form von hochgeladenen Schwerionen im Fragmentseparator FRS mittels Fragmentation oder Spaltung mit geringer Intensität hergestellt. Diese werden dann in den Speicherring ESR weitergeleitet und gespeichert. In IMP, übernimmt eine ähnliche Maschine (RIBLL2) die Erzeugung der Fragmente, bevor diese anschließend in CSRe gespeichert werden. Mit stochastischer und Elektronenkühlung wird die Geschwindigkeitsunschärfe der Teilchen reduziert. Mit 400 MeV pro Nukleon sind die Umlauffrequenzen der Teilchen etwa 2 MHz und proportional zur ihren Masse-Ladungs-Verhältnissen.

Diese Frequenzen werden kontinuierlich mittels zeitaufgelöster Schottky-Spektroskopie beobachtet. Eine plötzliche Änderung der Umlauffrequenz eines instabilen Teilchens ist möglicherweise ein Zeichen seines Zerfalls. Ob dies der Fall ist, muss anhand verschiedener Kriterien in der Datenanalyse festgestellt werden. Die Zeitpunkte dieser Zerfälle können anschließend für die Bestimmung der Lebensdauer des Teilchen verwendet werden.

Seit 1991 wird ein kapazitives Pickup im Speicherring ESR für zeitaufgelöste Schottky-Spektroskopie verwendet. Dieses Pickup kann bereits Einzelteilchen nachweisen, benötigt jedoch über 10 s Mittelung in der Zeit, um Nuklide mit $Z \sim 50$ zu zeigen. Um diese Zeit zu reduzieren, muss die Empfindlichkeit des Pickups erhöht werden.

Funktionsweise des Pickups

Die von den Teilchen induzierten elektromagnetischen Felder können resonante Moden in HF-Kavitäten anregen. Die Geometrie des Pickups und das verwendete Material spielen eine wesentliche Rolle in der Gestaltung der Feldbilder. Die Schottky Signale werden mittels einer Antenne ausgekoppelt und an einen Spektrumanalysator angeschlossen. Für die

Spektralschätzung des resultierten stochastischen Signals können verschiedene Methoden wie z.B. das Multi-Taper verwendet werden.

Motivation

Ein hohes Masse-Ladungs-Verhältnis setzt eine hohe Frequenzauflösung voraus, diese setzt eine Grenze der möglichen Messzeit fest. Sowohl die Abstände zwischen den Schottky-Frequenzbändern als auch ihre Breiten erhöhen sich mit der harmonischen Zahl, so dass das Verhältnis $\Delta f / f$ immer konstant bleibt. Mischt man eines dieser Bänder ins Basisband unter Beachtung des Nyquist-Kriteriums herunter, erzielt man ein größeres $\Delta f / f$. Je höher das ausgewählte Schottky-Band liegt, desto höher ist die Frequenzauflösung im Basisband. Eine höhere Frequenzauflösung impliziert eine kürzere Messzeit. Dies ist ein sehr interessantes Merkmal für die Analyse kurzlebiger Kerne.

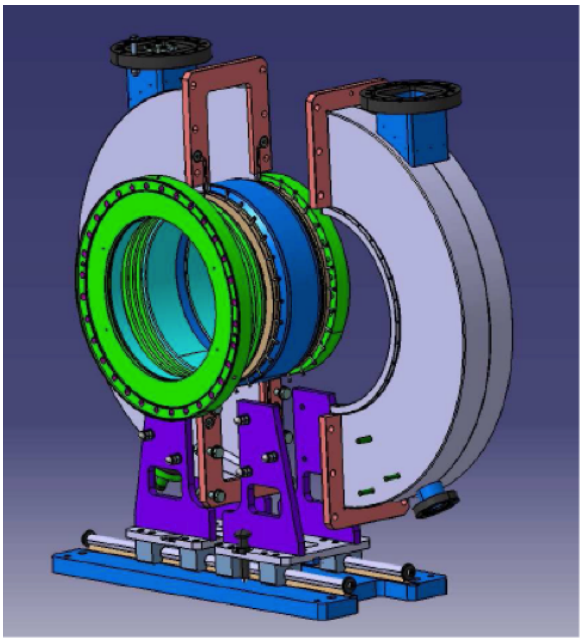

Mechanisches Model des Pickups. Bild: I. Schurig @ GSI

Es existiert jedoch folgendes Problem: Die spektrale Schottky-Rauschleistung bleibt in allen Bändern konstant. Die Aufteilung der Leistung auf größere Frequenzbereiche aufgrund der wachsenden harmonischen Zahl hat zur Folge, dass die Spitzenleistung, die für die Analyse interessant ist, immer kleiner wird und irgendwann im thermischen Hintergrundrauschen verschwindet. Durch das Resonanzverhalten kann das Pickup genau diese Schwäche kompensieren und sogar größere Signalpegel liefern.

Simulation und Entwurf

Der Entwurf des Pickups basiert auf einer Pillbox-Kavität mit Strahlrohren. Zwei von innen mit Kupfer beschichtete Halbzylinder formen einen luftgefüllten Hohlraum um ein Keramik-Gap, das im Strahlrohr mit Ultrahochvakuum installiert ist. Die Halbzylinder sind auf Schienen montiert und können auseinander geschraubt werden, falls sie nicht

benötigt werden, ein Kurzschluss des Gaps notwendig ist oder falls der Ring geheizt werden muss. Fernsteuerbare Kupfer-Tauchkolben können die Resonanzfrequenz des Pickups verstimmen. Der Durchmesser des Strahlrohrs war eine feste Vorgabe des Entwurfs und hatte einen wesentlichen Einfluss auf die Eigenschaften des Pickups.

Die Simulationen der elektromagnetischen Eigenschaften und des Transit-Time-Factors wurden mit SUPERFISH and CST-Microwave Studio® durchgeführt. Die charakteristische Impedanz wurde mit der Störkörpermethode gemessen und liegt bei etwa 42 Ohm. Dieser Wert ist nur abhängig von der Geometrie des Pickups und kann mit dem Energieverlust des Teilchens in Verbindung gebracht werden. Der unbelasteter Q-Wert liegt bei 1130 und die Resonanzfrequenz bei etwa 244 MHz.

Anwendung in Speicherringexperimenten

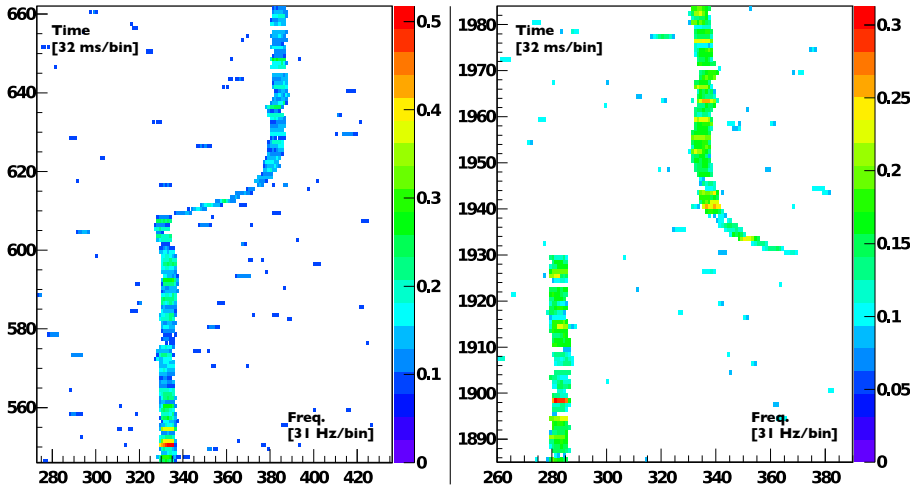

Einteilchenzerfall (nuklearer (orbitaler) Elektroneneinfang) $^{142}_{61}\mathrm{Pm}\rightarrow^{142}_{60}\mathrm{Nd}+\nu_e$ bei der harmonischen Zahl ≈ 124 und Frequenz $\approx 245\ [MHz]$. Die Farbkodierung der Signalleistung hat beliebige Einheiten.

Das Pickup wurde in mehreren Experimenten im Speicherring ESR verwendet. Im Mai 2010 wurde als Fortsetzung einer Reihe von Experimenten zur Bestimmung der Lebensdauer hochgeladener Ionen der orbitaler Elektroneneinfang wasserstoffähnlicher und heliumähnlicher Promethium-Ionen ($^{142}_{61}\mathrm{Pm}\rightarrow^{142}_{60}\mathrm{Nd}+\nu_e$) untersucht. Mit dem Pickup ist es gelungen, einzelne Teilchen mit 400 MeV pro Nukleon mit einer Zeitauflösung von 32 ms zu beobachten. Dies war ebenso die Zeitauflösung, mit der die Kernzerfallszeiten beobachtet wurden.

Das Pickup kann als ein sehr empfindlicher Stromsensor eingesetzt werden, wobei eine

externe Kalibration in diesem Fall notwendig ist. Im Jahr 2012 wurden intensive Uranstrahlen mit niedriger Energie im ESR gespeichert. Die Messzeiten waren lang genug, um mehrere Größenordnungen Teilchenverlust zu beobachten. Der Einschußstrom wurde mit dem ESR DC-Transformator gemessen und als Referenz für die Schottkyleistung verwendet. Das Pickup lieferte Signale in den Bereichen, in denen der DC-Transformator nicht mehr empfindlich ist.

Fazit und Ausblick

Das Pickup ist ein schneller, empfindlicher und zerstörungsfreier Detektor für Umlaufzeiten und Intensität des Schwerionenstrahls. Der GSI-Detektor wurde erfolgreich in Experimenten eingesetzt, der IMP-Detektor wurde in den CSRe installiert und wird für in-ring Experimente vorbereitet.

Mit dem Pickup können künftig isochrone oder nicht-isochrone Massenspektrometrien, sowie Studien kurzlebiger isomerer Zustände angestrebt werden. Verbessert werden kann die Intensitätsmessung durch einen präziseren DC-Transformator. Das Pickup kann ebenso für CR in FAIR und RI-RING in RIKEN interessant sein.

Das Pickup liefert Informationen bezüglich der longitudinalen Komponente des elektrischen Feldes. Ein Entwurf, der z.B. Dipolfelder nutzt, würde eine vollkinematische Studie des Rückstoßteilchens erlauben, was im speziellen Fall des o.g. Elektroneneinfangs, vollkinematische Informationen über das ausgestoßene Neutrino liefern würde.

Teile dieser Arbeit wurden in [S$^+$12], [NHL$^+$11] and [Z$^+$11] und GSI Scientific Reports [S$^+$11] und [NHL$^+$10] veröffentlicht.

Abstract

Nuclear astrophysics studies on highly charged radionuclides benefit from accelerator facilities with storage rings, where exotic nuclides produced with small yields can be efficiently investigated. Currently there are two accelerator facilities capable of storing highly charged heavy ions, GSI in Darmstadt and IMP in Lanzhou. Non-destructive detection methods are often used for in-flight measurements based on frequency analysis. The sensitivity of such detection systems are of primary importance specially when number of stored ions is small. Furthermore, since the exotic nuclides of interest are as a rule short-lived, the detectors must be fast.

One common form of such detectors are parallel plate SCHOTTKY monitors, on which particles induce a mirror charge at each passage. This method has been successfully used at ESR experimental storage ring of GSI since 1991 [Sch91]. In this work we describe a new resonant SCHOTTKY pickup operating as a high sensitive cavity current monitor which was mounted and commissioned in the ESR early 2010. It was successfully used in several storage ring experiments. A very similar pickup was mounted in CSRe at IMP Lanzhou in 2011. First in-ring tests have been performed and new experimental results are pending. The spectral analysis of acquired signals by the new detector has enabled a broad range of new physics experiments. The theory of operation and first experimental results and future perspectives will be presented in this thesis. Part of this thesis was published in [S$^+$12], [NHL$^+$11] and [Z$^+$11] and GSI Scientific Reports [S$^+$11] and [NHL$^+$10].

In the Name of God, The Compassionate, The Merciful.

CHAPTER 1

INTRODUCTION

The knowledge about the structure of matter and its fundamental interactions is crucial for our understanding of the laws of nature. Starting with the postulation of atoms in the ancient Greece the search for fundamental constituents of the matter is still going on. The discovery of electron and the alpha particle was followed by a series of successful experiments in nuclear and particle physics. At first, the main source of particles for experiments were radioactive material and cosmic rays. Later as ever higher energies were required, a way to increase the energy was necessary, so the accelerator era started. Ever since, accelerator physics has established itself as a separate branch of physics with concepts reaching far into the theoretical and applied physics. Apart from its applications in high energy physics, medical sciences have also profited from accelerators where they play a central role in developing modern therapy methods.

1.1. Particle Accelerators and Beam Monitors

An electric field is "a region of space characterized by the existence of a force generated by electric charge"[1]. This electric field surrounds every electrically charged particle. The force acts equally on other charged particles that are anywhere in that field as well as on the source charge itself. This force and the electric field are related as in $\vec{F} = q\vec{E}$. The electric field of a rapidly moving electric charge changes the properties of the surrounding space in such a way that according to special relativity theory, it may be interpreted as a *magnetic field* in the lab frame. Thus a time varying electric field (e.g. that of a particle passing an observer in the rest frame) generates a magnetic field. The magnetic field applies a

[1] The American Heritage Dictionary of the English Language.

transversal force on a charged particle only if it is moving so that $\vec{F} = q(\vec{v} \times \vec{B})$. So for a positive charge q, the direction of the force vector can be obtained from the right-hand rule. Together, these relations constitute the LORENTZ law of force:

$$\vec{F} = q(\vec{E} + \vec{v} \times \vec{B}) \tag{1.1.1}$$

This is one of the fundamental relations in the classical electrodynamics that enables many experiments in modern physics and governs the operation of world's most sophisticated accelerator facilities. Since the force caused by the magnetic field is perpendicular to the displacement vector, the work done by the magnetic field is zero, therefore the magnetic field can not contribute to a change in particle's energy. While an electric field can accelerate a particle as well as cause a change in its trajectory, a magnetic field can only deflect an already moving charge. The work done by the LORENTZ force is equal to the change in the kinetic energy of the particle:

$$\Delta\mathscr{E} = W = \int_{\vec{r_1}}^{\vec{r_2}} \vec{F} \cdot d\vec{r} = q \int_{\vec{r_1}}^{\vec{r_2}} \vec{E} \cdot d\vec{r} = q\,U \tag{1.1.2}$$

where $\vec{r}$ is the position vector and U is the electric potential difference between two arbitrary points in the electric field. For instance, an electron of charge $q = -e\,[C]$ gains $\Delta\mathscr{E} = 1\ [eV] \approx 1.602\,10^{-19}\,[J]$ of energy whenever it passes an electric potential difference of $U = -1\,[V]$.

A typical accelerator consists of sources, accelerating sections, targets and detectors. The type of experiment and requirements define how each of these sections may be designed. The most essential part of these is the evacuated beam pipe through which the particles travel. This makes vacuum technology one of the most important companions of accelerator physics.

In the source section, a plasma is made from a stable source material and the positively (or negatively) charged ions are directed towards the beam pipe. These can then be accelerated in many subsequent sections. The simplest of all accelerators is a design that generates a huge constant electric field in the direction of the beam pipe[2]. The first accelerator of this type was designed by J. D. COCKCROFT and E. T. S. WALTON in 1932 [CW32] based on a multiplier circuit designed by H. GREINACHER in 1919. Around the same time a design by R. VAN DE GRAAFF gained popularity and is still in use in many research centres.

[2] A detailed description of particle accelerators can be found in [LB62] and [Wil96] or its English translation. Historical notes in this chapter are adapted form [Bry10].

These accelerator types provide energies up to 10 MeV for singly charged ions or electrons. The demand for higher energies brought the idea of letting the particle pass an accelerator section several times. A first attempt was the *tandem van de Graaff* accelerator where the voltage was used twice. Energies beyond that can hardly be realised using constant electric fields. An increase in the energy of the particle is obviously possible only if the applied force is present at the time the particle enters the acceleration section. A realistic analogy is a mother, pushing her child on a swing, intuitively waiting for the moment just after the maximum deflection of the swing. For particles this can be realised by a periodic electric field whose amplitude is maximum at the time the particle enters the acceleration section. This idea was first suggested by G. ISING in 1924 [Isi24]. After leaving the accelerator section, the particle doesn't see the electric field until next time it enters the accelerating section. Obviously as the energy of the particle increases, the sooner it will arrive again, so the sooner the electric field must be applied. There are two choices, given a fixed frequency of the electric field, the field free travelling path of the particle must be longer, or if the path is fixed, then the frequency must be increased. The first choice leads to the concept of *linear accelerators* or in short *linacs* and their circular counterpart, the *cyclotron*. The second choice is the fundamental idea governing the operation of *synchrotrons*.

The first linac was built by R. WIDERÖE in 1928 followed by E. O. LAWRENCE in 1929 and L. W. ALVAREZ in 1946. Cyclotrons are in contrast to linacs more compact in size so medium and small sized cyclotrons can be found in many medical applications. The first cyclotron was built by S. LIVINGSTON in 1931. In a cyclotron a magnetic field is needed to keep the particle on a circular path. A constant magnetic field is generated using a *dipole magnet*. A particle with mass m, charge q and velocity v will be bent on a circular path of radius ϱ where the centripetal force equals the magnetic field force so that $F = qvB = mv^2/\varrho$ and we have:

$$B\varrho = v\frac{m}{q} \tag{1.1.3}$$

where $B\varrho$ is called the *magnetic rigidity* of the dipole magnet and is measured in units of [Tm], while $B = |\vec{B}|$. This feature of magnetic dipoles makes them suitable devices for *mass spectroscopy* since particles with different *mass to charge ratios* will have different speed and hence different revolution frequencies.

As in cyclotrons, dipole magnets are needed in synchrotrons as well, but since the flight path of particles is fixed in the form of a single round tube, the magnetic field intensity must be synchronously increased or *ramped up* to keep the particle on the flight path as the particles gain energy; hence the name synchrotron. This puts higher technical demands on the control electronics to achieve the highest efficiency. Nowadays the accelerator or the

machine is controlled all digitally using board-level digital control algorithms and computer based digital signal processing. In the annual *beam time* plan of many accelerator facilities, several hours are dedicated to the so called *machine experiments* with the goal of optimization of the operation of the accelerator. A common feature of synchrotrons (as well as linacs) are the ion optical elements that are responsible to keep the particle transversally in a certain region. These consist of quadrupole and sextupole magnets. A special type of synchrotrons are the *storage rings*. Storage rings are primarily used to store and observe a beam for a long time up to several hours or days.

Apart from fixed target experiments linacs and synchrotrons are also used for colliding experiments where two counter-moving beams of particles collide. This was again pioneered by R. WIDERÖE in 1943. Colliding experiments have the advantage that the center of mass energy is twice the energy of the beam $\mathscr{E}_{c.m.} = \sqrt{4\mathscr{E}_1\mathscr{E}_2}$. For fixed target experiments $\mathscr{E}_{c.m.} = \sqrt{2m_t\mathscr{E}_b}$, where m_t is the mass of target and $\mathscr{E}_b$ is the beam energy, but the overall yield of the fixed target experiments are higher. In nuclear astrophysics experiments where one is interested in the production of *radioactive ion beams* (RIB), a fixed target operates as a *production target*. The thickness of the target material is one of the main parameters of interaction. Two major methods are common: the so called *isotope separation on line* (ISOL) (e.g. the ISOLDE facility in CERN [Lin03]) with a very thick target, where particle beam is completely stopped, and the *in-flight fragment separation* (FRS) where the beam penetrates through a thin target while producing many fractions.

Particle detectors are essential parts in accelerator based experiments as they provide the means of obtaining measurement results of the experiment. Depending on which physical phenomenon is used for beam observation[3], particle detectors are based on different working principles and according to that, they are placed in different positions in the the accelerator. Generally, particle detectors can be divided into two categories, destructive and non-destructive detectors. In the destructive particle detector, a particle is lost sooner or later after it interacts with the matter inside the detector. These are for example semiconductor or gas-filled detectors that are usually installed around the target area to detect reaction particles.

Destructive particles detectors may also be used in the vacuum tube along the path of the flight. Some examples are FARADAY cups, scintillators, time of flight detectors (TOF) and particle counters. Scintillators are used to measure the beam profile. They feature a scintillating material that shines whenever it is brought into the flight path of the particles. Particle counters and TOF detectors are placed somewhat off the flight path and are reachable

[3]The reader is referred to [H^+89] for more information on physical phenomena used in beam observation.

only by those particles that leave their usual circulation orbit. Such change in the orbit can be a consequence of a change in mass or charge of the particles due to a nuclear reaction, decay or capture process. FARADAY cups are usually made of copper and are inserted into the ring using pneumatic or electric actuators. Apart from beam current measurements, they can be used to clear off the storage ring by collecting all particles.

Non-destructive particle detectors are sometimes referred to as *beam monitors*. Cutting the beam pipe, placing a resistor with a fixed value in between and measuring the voltage drop across it with a voltmeter can in principle provide a means for beam current measurement, resulting in a *beam current monitor* (BCM) or specifically a *DC current transformer (DCCT)* (WCM)[4]. The induced charge on the beam pipe can also be used to determine the transversal position of the beam in the beam pipe. These are the so called *beam position monitors* (BPM). In this type of detectors the signal of four pairwise parallel plates is subtracted to measure how far the beam has been from each. This information is then fed back to the digital control system to achieve optimized beam parameter adjustment.

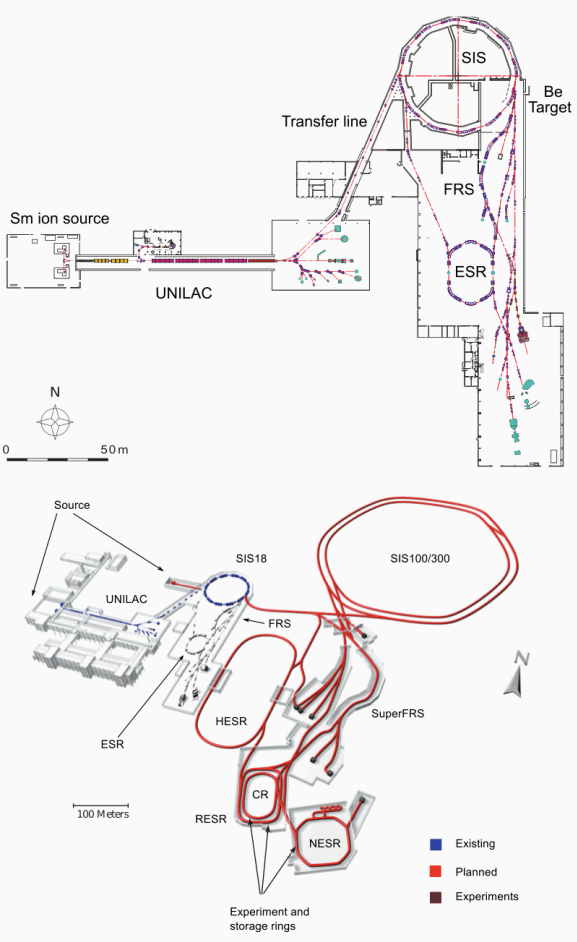

Figure 1.1: The existing GSI and future FAIR facility.

The same principle of image currents is used in the so called SCHOTTKY detectors. The presence of the particle induces a charge on the plates causing a periodic current that is further processed using FOURIER analysis.

Finally *resonant Schottky pickups* are used both as intensity and position monitors. In the former case, they are also known as *cavity current monitors*. They can be made to have much higher sensitivity than parallel plate SCHOTTKY detectors, but need external

[4]More information on DC current transformers can be found in [Web00]

calibration for accurate beam current measurements[5].

A whole new set of nuclear physics experiments are possible with parallel plate SCHOTTKY detectors and specially with resonant SCHOTTKY pickups in the storage rings. Short lived ion species can be stored long enough so that their decay can be observed directly. Due to high sensitivity, revolution frequency of a few down to a single particle can be measured so that by knowing the ion optical properties of the ring, masses of highly charged nuclides can be measured with high accuracy.

The GSI facility and the future FAIR project

GSI Helmholtzzentrum für **S**chwer**i**onenforschung GmbH (GSI Helmholtz Centre for Heavy Ion Research GmbH) was founded in 1971. It features three ion sources, a heavy ion linear accelerator LINAC, the synnchrotron SIS18, the storage ring ESR, the fragment separator FRS, the super heavy ion trap SHIPTRAP and many spectrometer magnets. GSI is the host to many experiments and international collaborations. Apart from many achievements in fundamental physics, GSI has contributed to hadron therapy. Facility for anti proton and ion research, FAIR was founded in 2010 as an extension to the existing facility. It is based on a large international collaboration and will host many experiments [Hen04]. A schematic of the existing GSI and future FAIR facility is depicted in figure 1.1. The experimental storage ring ESR (see figure 1.2 and [Fra85]) features a high quality vacuum, an electron cooler [Fra87] and a stochastic cooler [N$^+$00]. Many detectors, particle counters and experiment specific targets are installed in the ring. The petawatt laser device PHELIX is planned to operate at ESR [N$^+$05]. Apart from nuclear physics, the storage ring enables outstanding experiments in atomic physics such as dielectronic recombination in highly charged heavy ions [Bra00].

Other related facilities

Apart from the existing ESR at GSI and CSRe in Lanzhou ([X$^+$02]) and the future FAIR project, plans are also made to move the TSR storage ring from Heidelberg to CERN and to install it at HIE-ISOLDE. This will enable storage ring physics at an ISOL-type facility [G$^+$12]. The CRYRING from the Swedish MANNE SIEGBAHN Laboratory is also planned to be transferred to GSI for deceleration of anti-protons and highly charged ions at FLAIR in

[5]More information on detectors can be found in [Lam86], [Lam89], [Tay91] [GL92].

the future FAIR facility [D$^+$06]. Other future plans for storage rings for radioactive ion beams are the Rare-RI Ring at RIKEN [Y$^+$08] and the HIAF facility in China.

1.2. Motivation

Storage rings offer a possibility to perform experiments on highly charged ions (HCI) or radionuclides (HCR). Such studies are indispensable for nuclear astrophysics, where the nuclei involved in stellar nucleosynthesis are as a rule highly ionized. Often the exotic nuclides of interest can only be stored, due to small production cross sections, as single ions. This puts high demands on the sensitivity of detection systems. Furthermore, short half-lives of such nuclides constrain the timing properties of the detectors. In such experiments, non-destructive SCHOTTKY spectroscopy is one of the frequently used techniques.

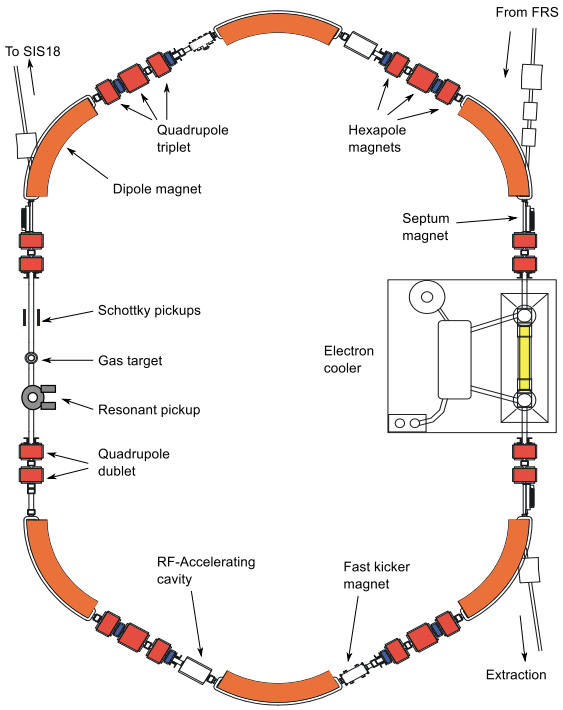

Figure 1.2: The ESR storage ring.

However, in experiments where single or few particle beams in a storage ring need to be investigated, conventional non-destructive methods may come short. The signal gained by conventional parallel plate monitors from low intensity beams is not sufficiently large. An alternative is to use radio frequency cavities as pickups. In a cavity resonator, after each excitation, fields can build up to make a larger signal allowing detection of even single particles. This work reports the design of a more sensitive resonant pickup for the ESR at GSI Darmstadt and for the CSRe, which is the heavy ion storage ring at the institute for modern physics in Lanzhou, China.

1.2.1 Previous works

A parallel plate Schottky beam monitor was designed by U. SCHAAF in 1991 and was built into the ESR ring at GSI Darmstadt [Sch91]. It operates at 60 MHz and has ever since been used in many successful experiments with higher beam currents. Specifically, it was successfully used in nuclear mass measurements [Sch97], study of beta decay of highly charged ions, for example [Win09] and [LB11] and observation of bound state beta decay in ^{187}Re-^{187}Os system [B^{+}96] which led to new results in estimation of galactic age.

Other examples of SCHOTTKY monitors are the 21 MHz resonant detector made by D. MARTIN et. al. [M^{+}89] and the 1.7 GHz slotted wave guide Schottky detector made by , R. J. PASQUINELLI et. al. for Tevatron.

In 1976 W. SCHNELL, L. THORNDAHL and their colleagues designed a rectangular resonant cavity for the ICE storage ring at CERN in order to detect stored anti-protons [Tho11]. This resonator had dimensions of 70cm x 70cm and 20 cm in the direction of beam pipe, it was made of 1cm thick aluminium plates tightly fastened with screws. Since the resonator was air-filled, the two upper and lower halves could be easily mounted around a ceramic gap which separated the vacuum pipe which had a diameter of about 150mm. A large number of metal fingers contacts were used for RF shielding. The resonant frequency was about 129 MHz and could be tuned via a rotatable metal paddle in the cavity. About 80 anti-protons were observed in the ICE storage ring with that detector [B^{+}74] and [M^{+}79].

Another cavity monitor was made for Tevatron by D. A. GOLDBERG and colleagues [G^{+}87]. It used a deformed rectangular geometry with two separate modes (TM210 and TM120) to detect the transversal particle position at 2 GHz.

J.-C. DENARD and colleagues built a high accuracy beam current monitor for CEBAF [D^{+}01] using two cylindrical cavities each tuned on TE010 mode at 1947 MHz with high temperature stability. These were calibrated using a commercial parametric current transformer (PTC) that was placed in between the two cavities.

Another resonant Schottky pickup for longitudinal and transversal analysis is currently under development for the collector ring CR in FAIR as a part of a PhD thesis at Technische Universität Darmstadt [H^{+}12].

1.2.2 Structure of this work

The theoretical background will be discussed in chapter 2. In this part I discuss the figures of merit and parameters that are needed to be considered for designing a resonant pickup. Following that, I will present design aspects, simulations results and bench-top measurements on the device in chapter 3. The results obtained in storage ring experiments using the pickup will be presented in chapter 4. Chapter 5 concludes this work. Some detailed complementary information is provided in appendix A.

CHAPTER 2

THEORETICAL DESCRIPTION

In this chapter the underlying theoretical aspects of the resonant pickup is discussed. The aim is to cover different topics that are crucial to understanding the operation of the resonant pickup and what should be expected from it when used in experiments as a measurement tool.

2.1. Cavity Resonators

Classical electromagnetism is a framework that provides solutions to many different real life problems. It has successfully allowed for numerous advances in fundamental physics and technology in modern times, from particle accelerators and digital computing to communications and transportation. With such advances, even more complicated experiments became possible, with which fundamental laws of nature and even electromagnetism itself were put to higher precision tests. Construction of large scale particle accelerators became almost exclusively possible on the basis of classical electromagnetic theory.

From the point of view of modern physics though, electromagnetism can be described by the quantum theory of massless spin one fields. Quantum electrodynamics (QED) can in principle lead to results predicted by classical electrodynamics (CED) in classical limits. It has not always been possible or easy to find a QED equivalent of all phenomena that are described within the CED. A prominent difficulty is the radiation reaction force of the a moving charged particle [Roh07]. Classical electrodynamics remains a challenging field of theoretical physics.

The reader may be referred to many excellent books on classical theory of electromagnetic

fields[1]. For a rather brief review, section A.1.1 can be consulted. There, I have tried to explain the steps that are necessary to describe the field patterns in a RF cavity resonator. In section A.1.4 a review of the concept of resonance is provided. There it is shown that RF cavities can be described as a superposition of many resonant systems. Using these two descriptive approaches, we can further investigate other properties of cavity resonators.

The simplest form of a resonant cavity is closed ideal pillbox cavity which is described in the following section.

The pillbox cavity

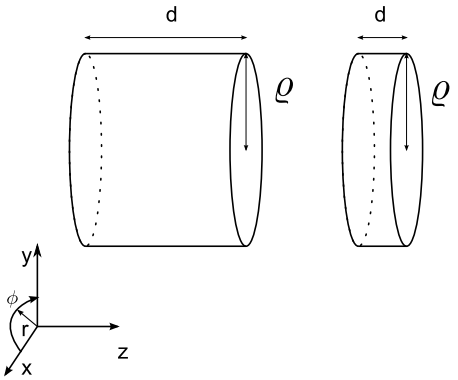

Figure 2.1: A cylindrical and a pillbox cavity.

A pillbox cavity is a short cylindrical cavity with $d < \varrho$ as shown in figure 2.1. As long as $d < 2.03\varrho$ the fundamental mode will be the TM010[2] [Jac98]. This can also be verified by solving the set of equations A.1.41 and A.1.42. In this case the equation A.1.44 reduces to

$$f_{010}^{\mathrm{TM}} = \frac{j_{01}}{2\pi\sqrt{\mu\varepsilon}\varrho} \tag{2.1.1}$$

which is independent of d. This is an advantage since in this type of cavity the resonance frequency can be *tuned* to a desired value easily by changing the geometry in the radial direction, i.e. reducing or increasing ϱ at a wall section. This is done by putting a small conducting object, usually a motor driven *plunger* into the cavity. This procedure is called *cavity perturbation*. Of course any kind of cavity perturbation must be very small, otherwise the mode geometry changes and hence *hybrid modes* appear. On the other hand, by an intentional perturbation at a certain position, mode geometry can be shaped to a desired pattern so that some modes can be suppressed and others enhanced. For instance, higher order modes can be suppressed and extremely high Q values can be achieved. This is the idea behind the so called *evanescent mode cavities*[3]. Any deviation from the perfectly cylindrical shape is already too complicated to be calculated analytically. Fortunately numerical methods come in handy in this

[1] Such as [Che89], [Col00], [Gri99], [Jac98], [Kli10], [PP05], [Pur85], [Sim93] and [Ung02]
[2] Otherwise TM111 will be the fundamental mode.
[3] A short description is provided in the outlook in section 5.2

case and we will make use of such methods in the simulation section 3.2. As we will see in chapter 3.3.2, cavity perturbation proves to be useful in actually measuring cavity features. For the fundamental mode, equations A.1.41 and A.1.42 reduce to

$$E_z(r,\varphi,z) = C\frac{1}{i\omega_0\varepsilon}\left(\frac{j_{01}}{\varrho}\right)^2 J_0\left(\frac{j_{01}}{\varrho}r\right) \tag{2.1.2a}$$

$$H_\varphi(r,\varphi,z) = C\frac{j_{01}}{\varrho}\,J_1\left(\frac{j_{01}}{\varrho}r\right) \tag{2.1.2b}$$

According to equation A.1.87, in order to find an expression for the Q value of each mode, apart from the stored energy we must have a means to quantify the power loss. The field expressions in equations A.1.41 and A.1.42 and the resulting field geometry are valid for a cavity resonator with infinitely conductive walls. In reality good conductors have finite conductivities. With finite conductivities, the wave number will be complex valued (cf. equation A.1.18) and the modes are not pure TM or TE any more. So those expressions can not be used for estimation of power loss, but it is possible to use the ideal field patterns for high conductive material as a good approximation. This is known as *power loss method* (PLM) in the literature. Similar to equation A.1.91, the stored energy in a pillbox cavity can be computed as twice the energy stored in the electric field in volume V that it encloses

$$W = 2W_e = 2\times\frac{1}{4}\varepsilon_0\varepsilon_r\int_V |\vec{E}|^2\,dV \tag{2.1.3}$$

The lost power is a result of the tangential component of the magnetic field at the surface of non ideally conducting walls due to induced currents.

$$P_L = \frac{1}{2}R_A\oiint |\vec{H}_t|^2 dA \tag{2.1.4}$$

where

$$R_A = \sqrt{\frac{\mu\omega}{2\sigma}} = \frac{1}{\sigma\delta} \tag{2.1.5}$$

is the frequency dependent surface resistance, σ is the conductivity of the surface and δ is the skin depth from equation A.1.20. The integration is over all wall surfaces. Using these expressions, following relations can be derived for the Q value of different modes [Ung89]

$$Q_{mn0}^{TM} = \frac{\eta j_{mn}}{2R_A\left(1+\frac{\varrho}{d}\right)} \tag{2.1.6a}$$

$$Q_{mnp}^{TM} = \frac{\eta\left[j_{mn}^2+\left(\frac{p\pi}{d}\varrho\right)^2\right]^{1/2}}{2R_A\left(1+2\frac{\varrho}{d}\right)} \tag{2.1.6b}$$

$$Q_{mnp}^{TE} = \frac{\eta\left[j_{mn}'^2+\left(\frac{p\pi}{d}\varrho\right)^2\right]^{3/2}\left(j_{mn}'^2-m^2\right)}{2R_A\left[\left(\frac{mp\pi}{d}\varrho\right)^2+j_{mn}'^4+\frac{2R}{d}\left(\frac{p\pi}{d}\varrho\right)^2\left(j_{mn}'^2-m^2\right)\right]} \tag{2.1.6c}$$

where η was introduced in equation A.1.17.

For the calculation of the integral in equation 2.1.4 for a pillbox all sides must be considered. Two integral identities are needed which are listed in section A.1.5. Some of the first modes of a pill box with $\varrho = 30\ [cm]$ and $d = 9\ [cm]$ are listed in table 2.1 with their corresponding resonant frequency and Q value computed using equations A.1.44 and 2.1.6 with m, n and p indexes running up to 10. Apart from the lowest indexes, other mode frequencies may appear in between the computed ones if higher index numbers are used. Note that the first TE mode appears at a much higher frequency. The field pattern of the first four modes are depicted in figure 2.2 computed using equations A.1.41.

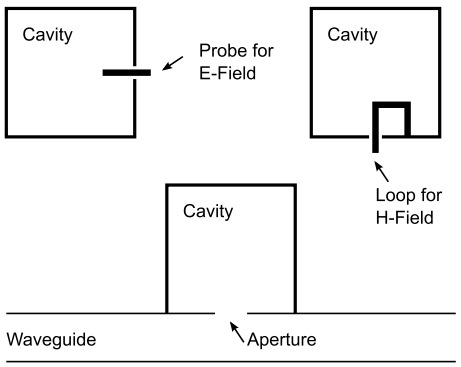

Figure 2.3: Electric, magnetic or electromagnetic coupling.

In order to use resonant cavities in RF circuits or accelerator physics, power must be delivered to or taken away from the cavity via a coupling mechanism (see figure 2.3). Coupling can be achieved either to the magnetic field or to the electric field or by letting a portion of a propagating electromagnetic field penetrate through an aperture into a cavity. Some pioneering work in this topic has been done by BETHE [Bet44]. The cavity can then be *excited* and brought to oscillation. Length of the probe for electric, surface of the loop for magnetic and size of the opening of the aperture for the electromagnetic coupling are important fac-

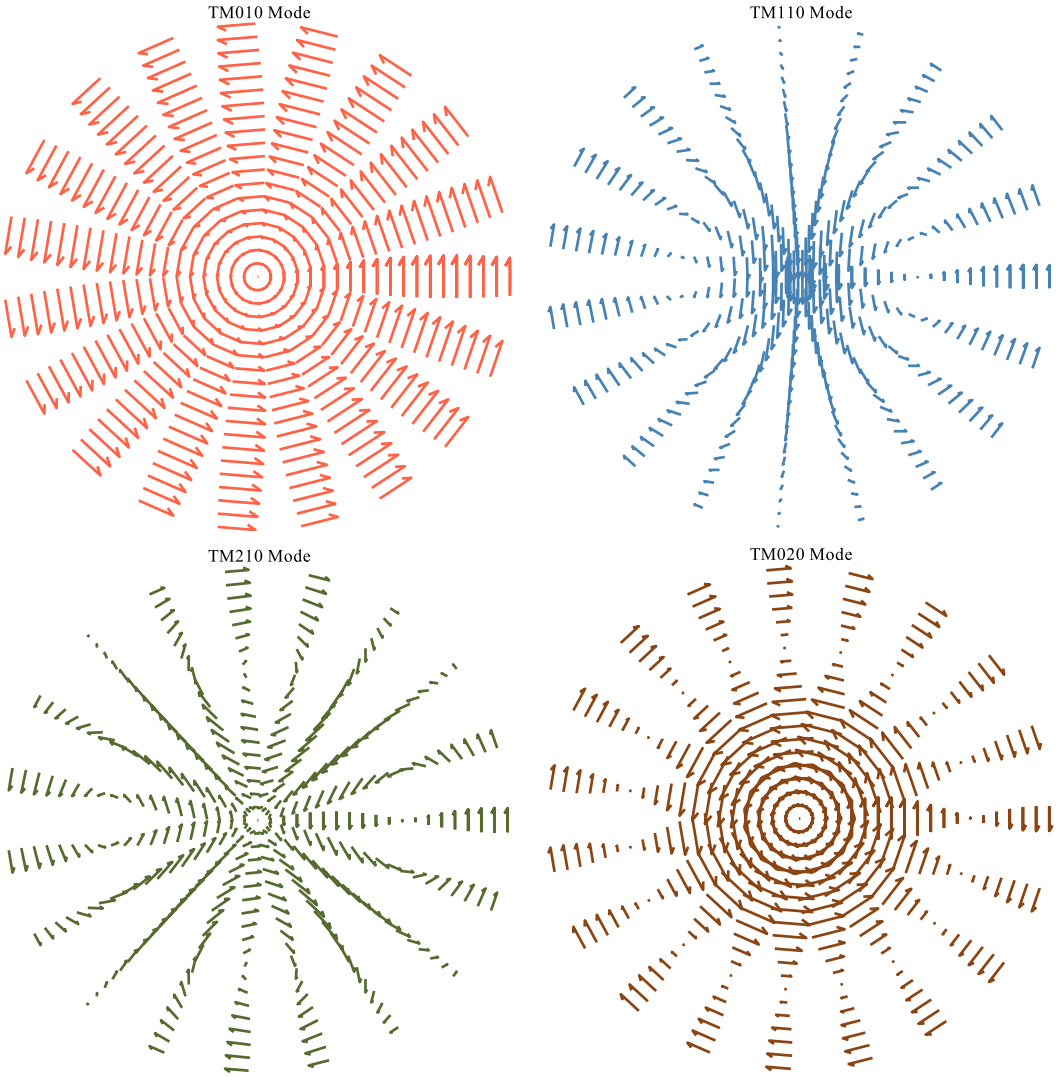

Figure 2.2: Magnetic field patterns for the first 4 modes of a pillbox with $d = 0.09\ [m]$ and $\varrho = 0.3\ [m]$. Depicted are r and φ axes, z is perpendicular to paper.

tors that allow adjustment for optimal coupling. In the case of loop coupling, the surface normal to the flow of time dependent magnetic field is the key factor (see first MAXWELL's equation A.1.1). This surface can be reduced by changing the angle between it's normal vector and the magnetic field vectors buy just turning it, hence allowing a very simple mechanical way to find an optimal coupling.

A cavity may have not only one, but *as many* coupling mechanisms as needed for a design concept. Although mathematically there are no limitations on the number of coupling ports, more complex systems can only be solved using numerical code. Any of such coupling mechanisms can allow *coupling into* or *coupling out* of the cavity. A cavity with

Mode	f_0 $[MHz]$	Q	Mode	f_0 $[MHz]$	Q
TM010	382.475	20768.4	TM320	1552.44	41841.7
TM110	609.413	26215.5	TM610	1580.29	42215.3
TM210	816.794	30350	TM130	1618.04	42716.6
TM020	877.94	31465.5	**TE111**	1691.06	27365.4
TM310	1014.73	33828.1	TM011	1708.87	24812.6
TM120	1115.79	35472.7	TE211	1734.91	27487.5
TM410	1206.89	36892.3	TM420	1759.78	44548.4
TM220	1338.72	38855	TM710	1763.23	44592
TM030	1376.33	39397	TM111	1773.51	25277.5
TM510	1395.06	39664.2	TE011	1773.51	32312.1

Table 2.1: Fundamental and 19 higher order modes of an ideal pill box cavity with 30 $[cm]$ radius and 9 $[cm]$ depth.

one coupling loop is a single port circuit. The whole cavity acts as a complex valued impedance Z. A cavity with two coupling mechanisms is equivalent to a complex valued transformer.

Pillbox cavities with beam pipe

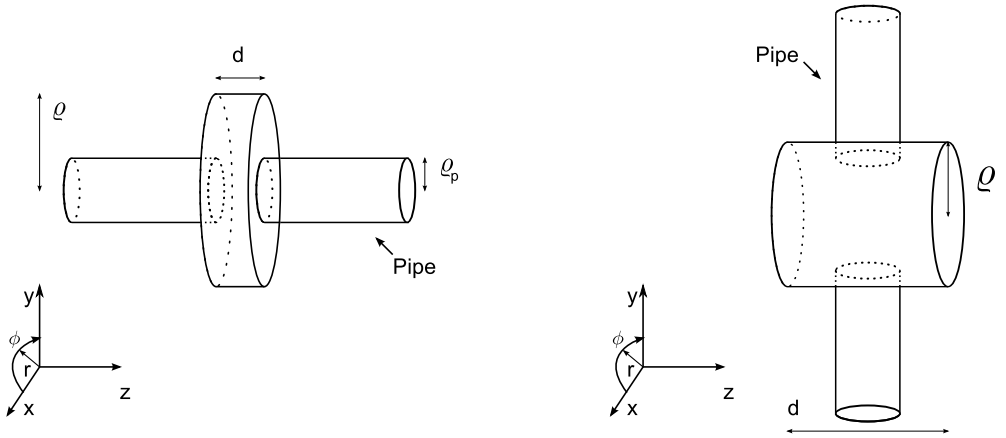

(a) (b)

Figure 2.4: Cylindrical resonators with beam pipe.

The resonant pickup that is the subject of this work is basically of the type shown in figure 2.4(a), a modified pillbox with beam pipes attached. Like the aperture in figure 2.3, electromagnetic modes couple to the cavity through the *gap*. A magnetic loop is installed on the wall side as a second coupler. In such a construction, if power is provided to the loop,

modes inside the tube can be excited and if electromagnetic waves flow through the tube, then power can be extracted from the loop. In the latter case, as stated in the previous section, we are dealing with a complex valued transformer.

In accelerator physics, the pipe is not primarily used as a wave guide, but as an evacuated beam pipe. Electromagnetic power that is actually being transformed originates from charged particles. Electromagnetic modes inside a resonator with beam pipe differ from those of an ideal pill box in the sense that it is not possible to describe them in terms of pure cavity modes since they are a superposition of different cavity modes and wavegudie modes. For larger values of ϱ/ϱ_p modes are more cavity-like and for smaller values modes are more waveguide-like. Hence, the resonator-pipe system acts more like a wave guide the larger the openings are, in which case less resonant behaviour is expected.

Only a certain number of resonator modes lie below the tube cutoff frequency and actually contribute in resonance behaviour. Propagating waves in the tube that excite these resonant modes are sometimes said to be *trapped* inside the resonator. A field component that has a phase velocity close to that of the particle is called *synchronous*. If the phase θ_s of a particle with respect to that of field is such that $\sin(\theta_s) > 0$ then the particle is accelerated otherwise the field will gain amplitude from particle [ZK98]. In the former case we deal with an *accelerating cavity* which needs external drive and in the latter case the cavity can operate as a pickup. So charged particles can excite resonant modes in the cavity which in turn couples to the magnetic loop. Then the power induced by the particle can be extracted out say to an instrument. Those modes that are below the pipe cut-off frequency, extend into the beam tube. Due to the larger surface, larger losses are present, so that the overall Q value for trapped modes are significantly less than comparable modes inside an ideal pill box.

The cut-off frequency of the beam pipe is the same as the expression in equation 2.1.1 but for the radius of the pipe ϱ_P [Wei08]. For a beam pipe with radius $\varrho_P = 125\ [mm]$ the cut-off frequency is $f_c \approx 918\ [MHz]$.

2.1.1 Wake fields and impedance

Fields of a moving charge

In the co-moving reference, a point like charge will have static electric fields lines symmetrically distributed in the radial direction, so they don't result in magnetic fields. In the lab frame on the other hand, the electric field of a moving charge appears to be time depen-

dent and hence causes a magnetic field. This electromagnetic field surrounds the constantly moving charge. Any mechanism (such as an antenna) that is put in the neighbourhood of that field in order to extract energy from it will act back or *react* on the particle itself. The particle will continuously interact (get or take energy) with the antenna, thereby loosing energy itself. In other words it will experience the presence of the antenna and the antenna is said to be in the *reactive region*. The extent of this region depends on the wavelength of the component of the electromagnetic field in question. This analogy is similar to the mechanism used in electric transformers.

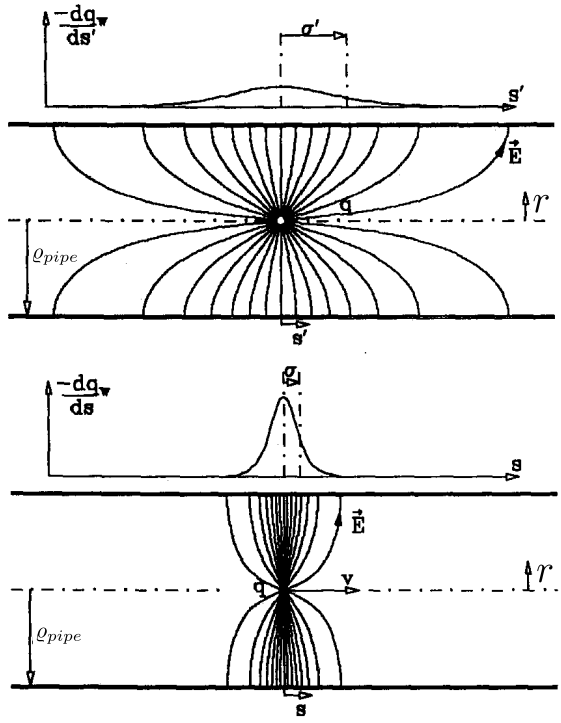

Figure 2.5: E-Field lines in the c.m. (top) and lab frame (bottom) from [H+89].

By contrast, electromagnetic *radiation* occurs only if the motion of the charge is deviating from its *constant* velocity. Energy is taken away form the particle in form of electromagnetic radiation that leaves the surroundings of the charge and travels through the medium. Apart from loosing energy, the charge will not notice the interception of this radiated field by observers. The radiation may still exist even if the source of the radiation does not exist at all. This analogy is much like radio and TV broadcasting or the burst of the SN1987a supernova. The distance of the supernova explosion to earth is about 167000 light years, the burst was only visible several months during 1987, this leads to the conclusion that source of the burst, which emitted electromagnetic radiation in form of visible light did not exist in 1987 any more.

In an unbounded medium, viewed from the lab frame, the field lines of a moving charge are subject to relativistic contraction. For the ultra relativistic case, there are no field components in front or back of the charge itself. The situation is similar in an ideal smooth perfectly electrically conducting (PEC) beam tube except that the presence of the tube changes the field geometry *at all speeds*. According to basics of electromagnetism, electric field lines of a charge must all end perpendicularly on the inner wall of the perfectly

conducting tube. The electric field lines can be described using the following equations

$$E_r'(r,s') = \frac{q}{2\pi\varepsilon_0\varepsilon_r r}\sum_{n=1}^{\infty}\frac{J_1\left(\frac{j_{0n}}{\varrho_{pipe}}r\right)}{J_1^2(j_{0n})}\exp\left(-\frac{j_{0n}}{\varrho_{pipe}}|s'|\right) \tag{2.1.7a}$$

$$E_r'(r,s') = \frac{q}{2\pi\varepsilon_0\varepsilon_r r}\sum_{n=1}^{\infty}\frac{J_0\left(\frac{j_{0n}}{\varrho_{pipe}}r\right)}{J_1^2(j_{0n})}\exp\left(-\frac{j_{0n}}{\varrho_{pipe}}|s'|\right) \tag{2.1.7b}$$

where the BESSEL function notation is the same as in the appendix A.1.1, s corresponds to the distance on z coordinate axis and the primed variables show quantities in the ion rest frame (see figure 2.5 where q_w is the charge on the wall). These equations and the following relations are described in detail by A. HOFMANN in [H$^+$89]. The electric field lines on the wall induce a mirror charge *distribution* that always follows the particle no matter how fast the charge travels, since inside of a metal there are infinitely many electrons in the conduction band. The electric field lines and their resulting magnetic field lines in the lab frame are subject to relativistic contraction

$$E_r = \gamma E_r' \ , \ B_\varphi = \frac{\beta\gamma E_r'}{c} \ , \ s = \frac{s'}{\gamma} \ , \ r = r \tag{2.1.8}$$

hence the electric field lines will be present in an opening angle $\pm 1/\gamma$. The induced linear charge density and its FOURIER transform will be [H$^+$89]:

$$\lambda(z-\beta ct) = -\frac{q\gamma}{\varepsilon_0 r}\sum_{n=1}^{\infty}\frac{1}{J_1(j_{0n})}\exp\left(-\frac{j_{0n}|s-\beta ct|}{\gamma\varrho_{pipe}}\right) \longleftrightarrow \tilde{\lambda}(\omega) = -\frac{q}{\beta c}\frac{1}{I_0\left(\frac{\omega\varrho_{pipe}}{\beta\gamma c}\right)} \tag{2.1.9}$$

where is I_0 is the first modified BESSEL function. At the ultra relativistic limit the opening angle approaches zero and the wall current distribution is equal to the beam current distribution. The longitudinal electric field strength vanishes and a strong radial field causes a rotational magnetic field as in equation A.1.17 where we had $E_r(z) = \eta_0 H_\varphi(z)$.

Wake functions and wake potentials

Now we consider the case where the particles travels with a constant velocity. A non-ideal section in the beam pipe behaves like an antenna that is put in the near field of the

beam.

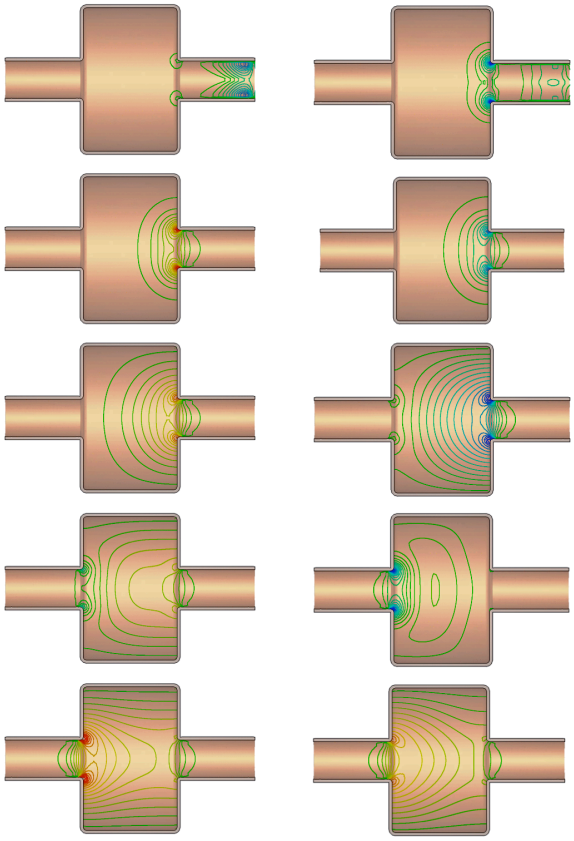

Figure 2.6: Simulated E-field lines of a resonator with beam pipes, sequence: left to right, top to bottom.

A non ideal section of the beam tube can be either

- A perfectly conducting, but non-smooth section, i.e. antennas, bumps, bellows, obstacles, etc.
- A smooth but resistive section.
- A combination of the above.

Considering the first case, as stated in the previous section, the particle continuously interacts with the non-smooth section and thereby looses or gains energy. Now since the particle is passing fast, the interaction time is short, so the part of the field energy that was transferred from the particle to the non-smooth section but didn't have the chance to get back to the particle is said to be *trapped*. These fields are called *wake fields*. A simulation of wake fields is shown in figure 2.6 in a resonator with $\varrho = 23\ [cm]$, $d = 30\ [cm]$ and $\varrho_{pipe} = 6\ [cm]$. This resonator has its fundamental mode at $500\ [MHz]$.

The smaller the cavity, the smaller is the amount of trapped fields. Depending on how lossy the structure is, in other words how high the Q value of the equivalent circuit of the structure for every given frequency band is, these wake fields may remain in the structure for a long time. So they can affect the movement of a charge that is following the original one say in the same bunch, or in following bunch. In circular machines, these fields may even affect the original particle itself in the next turn. So one differentiates between *short range* and *long range* wake fields. For lower Q values we are dealing with *broad band wake fields*. For high Q values we are dealing with *narrow band wake fields*. A cavity resonator, like the one that is the subject of this work, is an intentionally designed non-smooth beam pipe section with a large Q value in order to trap electromagnetic waves near its *eigenfrequencies*.

Resistive wall sections give rise to *resistive wall wake fields*. Here, due to the potential difference between each infinitesimal section of the beam pipe, wake fields are *left behind* the particle. In a system with intentional high Q cavities the effects of resistive wall wake fields are negligible and can be ignored[4]. Both kinds of wake fields remain fully behind the particle if it is travelling ultra-relativistically. If not, a portion remains in front of the charge. This will be discussed in an upcoming section on beam loading.

Wake fields can have undesirable effects and these should be taken into account when designing accelerator structures. While longitudinal components of the electric field accelerate or decelerate the particles, the transversal component may increase the beam cross section. So their collective effects may cause beam instabilities and finally lead to partial or complete loss of beam (*beam blow up*, BBU). Intensive wake fields may also cause extreme heat that may damage the structure. Numerous works of theoretical and applied research have been carried out on the analysis of wake fields and methods that eliminate their effect on beam instabilities. Nevertheless, same wake fields are useful when it comes to detection of a particle as a means of beam diagnostics.

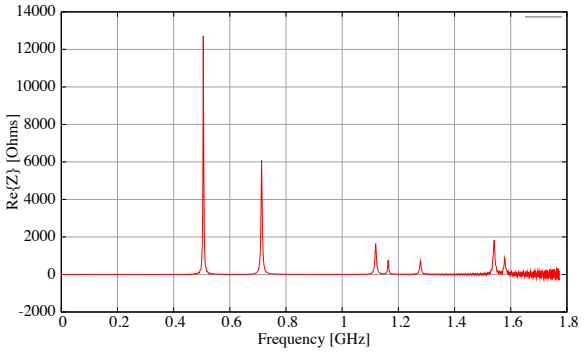

Figure 2.7: Simulated longitudinal wake impedance of the resonator in figure 2.6 (real part).

The fundamental property of a structure that causes wake fields and therefore takes energy away from a particle and dissipates it, can be modelled as an impedance, the *coupling impedance*. Coupling impedance relates the beam current to the induced voltage along the beam trajectory [RV68]. The concept of coupling impedances for a single RLC circuits was introduced in equation A.1.100. A passive structure has infinitely many modes, i.e. it consists of countably infinitely many equivalent RLC circuits each with their own characteristic values of center frequency, loss and coupling impedance. To account for all, one can just add up the effect of all by modifying equation A.1.100 so that for each mode ν we have [Mor94]:

$$Z(\omega) = \sum_{\nu} \frac{R_\nu}{1 + iQ_\nu(\delta\omega_{0\nu})} \tag{2.1.10}$$

[4]More information on resistive wall wake fields can be found in [BS96], [ZO04] and [S+06].

where $\delta\omega_{0\nu} = \left(\frac{\omega}{\omega_{0\nu}} - \frac{\omega_{0\nu}}{\omega}\right)$ is the detuning factor. A plot of the coupling impedance with respect to frequency may show infinitely many broad or narrow peaks depending on the Q value of each mode (cf. figure 2.7). The coupling impedance is in general a complex quantity. Its real part describes the energy loss and the imaginary part is responsible for phase lag or advance.

Closely related to the concept of coupling impedances is their time domain counter part, *wake functions* where both describe the same physical concept from different perspectives. It is defined as the work done by the LORENTZ force in equation 1.1.1 caused by electromagnetic fields of a leading charge on a trailing charge travelling at a distance behind it is

$$\Delta W = \int_{-\infty}^{\infty} q(\vec{E} + \vec{v} \times \vec{B})\, d\vec{z} \tag{2.1.11}$$

where $\vec{v}$ is the speed of both charges and $\vec{E}$ and $\vec{B}$ are in general functions of time, distance between the two particles and each of their radial positions with respect to the axis in cylindrical coordinates. On the other hand, we can define the *wake loss parameter* k as the energy lost by *leading* charge q_1 per unit charge squared[5]

$$\Delta W = q_1^2 k \tag{2.1.12}$$

and the *wake function* as the energy lost by the *trailing* charge q_2 per unit of both charges [P+03]

$$\Delta W = q_1 q_2 w \tag{2.1.13}$$

Furthermore, since the LORENTZ force is a vector quantity, the energy in expression 2.1.11 can be calculated separately for longitudinal and transversal directions. This leads to the definition of longitudinal and transversal wake functions $w_\parallel$ and $w_\perp$. If both charges travel on axis, then the wake function is only a function of distance between them. For the longitudinal case, the inner product of the vectors reduces the expression to

$$w_\parallel(s) = \frac{1}{q_1} \int_{-\infty}^{\infty} \vec{E}_z(z,t)\, d\vec{z} \tag{2.1.14}$$

[5] As an analogy from basic circuit theory we know that the energy stored in a capacitor is $W = \frac{1}{2}CU^2 = \frac{1}{2}\frac{q^2}{C} = \frac{1}{2}qU$. Also please compare with equation A.1.89.

with $t = \dfrac{z+s}{\beta c}$ [WW92]. In some literature the wake function is equivalently defined by the time delay between the two charges [P$^+$03]. Both wake functions and loss parameters depend in general on the transversal position of the charges.

As mentioned earlier, the coupling impedance is the FOURIER transform of the wake function:

$$Z_{\parallel}(\omega) = \int_{-\infty}^{\infty} w_{\parallel}(t) \mathrm{e}^{-i\omega t}\, dt \tag{2.1.15}$$

Wake functions are measured in units of $[\Omega/s] = [V/C]$, but it is customary to use $[V/pC]$ in accelerator physics. If instead a finite charge distribution is taken, then we talk about *wake potentials*, by definition per unit charge for the longitudinal case and per unit momentum for transversal case. So, wake potentials can be determined by the convolution of the wake function with the charge distribution, and are therefore not independent of charge distribution any more.

Wake function of an equivalent RLC

For each resonant mode inside a cavity one can calculate the loss parameter and wake function or potential. Accordingly the impedance is a sum over all resonances. For a single resonant mode, the impedance was shown to be the expression in equation A.1.100. The wake function in this mode is derived in detail in [ZK98] by taking the inverse FOURIER transform of it:

$$\begin{aligned} w_{\parallel}(t) &= \frac{R}{i4\pi Q'} \int_{-\infty}^{\infty} \left(\frac{\omega_1}{\omega - \omega_1} - \frac{\omega_2}{\omega - \omega_2} \right) \exp(i\omega t)\, d\omega \\ &= \frac{R}{Q}\omega_0 \left(\cos\omega_0' t - \frac{1}{2Q'} \sin\omega_0' t \right) \exp\left(-\frac{\omega_0}{2Q} t \right) \end{aligned} \tag{2.1.16}$$

where $Q' = \sqrt{Q^2 - 1/4}$ is the reduced quality factor, $\omega_{1,2} = (\omega_0/Q)(i/2 \pm Q')$ are the poles of frequency in the complex plane. This expression shows a damped oscillation with a modified frequency $\omega_0' = \omega_0 Q'/Q$. We also see this behaviour in the context of examining the RLC circuits in figure A.6 on page 139. For high $Q \gg 1$ cavity the expression can be approximated as [ZK98]:

$$w_{\parallel}(t) \approx \frac{R}{Q}\omega_0 \cos(\omega_0 t) \exp\left(-\frac{\omega_0}{2Q} t \right) \tag{2.1.17}$$

A plot of this expression is shown in figure 2.8 for demonstration values of Q and R. For a particle with $\beta < 1$, the cosine in the wake function has a phase offset [P+03]. From these expressions, it is obvious that the amplitude of the damped oscillation is directly proportional to the factor R/Q which we also encountered in equation A.1.115. Also a high Q resonator has a 'longer' memory. We encountered the same effect in the RLC oscillator model in figure A.6 at the top row. A similar expression can be found for the wake potential of a bunch with a Gaussian distribution [ZK98].

Impedance of a cavity with beam pipes

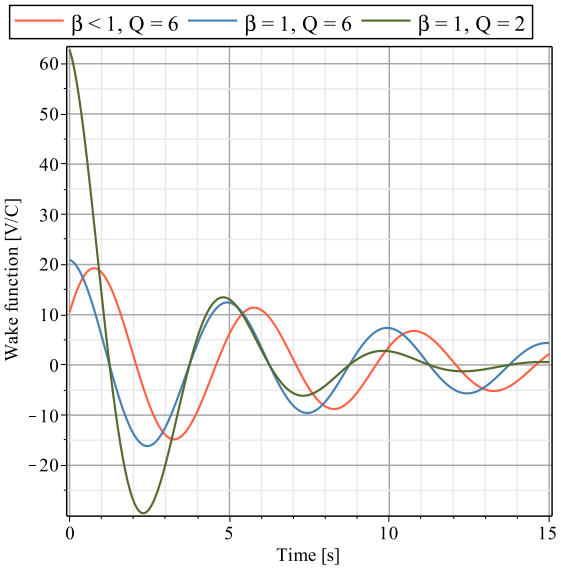

Figure 2.8: Wake function for an RLC with $R = 100[\Omega]$ and different values of Q and β.

Calculation of impedance is more challenging in a resonator with beam pipes since analytical expressions are more difficult to obtain for different regions. Apart from pure numerical calculations, there exist methods known as *field matching* techniques where wave guide field solutions of the beam pipe is matched to the cavity solutions. These solutions are semi analytical that means they are in the form of expressions containing infinite systems of linear equations which then need to be truncated for a large number using computers. The larger the number is, the more accurate the final result will be. Keeping figure 2.4(a) in mind, two popular choices are possible for matching. Either matching is done in the resonator volume at radius $r = \varrho_p$ or at $z = \pm d/2$. Both lead to similar expressions which then need to be solved semi analytically using computers. A complete chapter in [ZK98] is devoted to field matching techniques to which the reader is referred, and to the references named therein. Another approach is discussed in [Hen85] and [Hen86]. A disadvantage of field matching techniques is the limited choice of shapes, usually restricted to cylindrical symmetric structures with simple outlines. Meanwhile numerical solvers allow analysis of arbitrary shapes. The real part of the longitudinal wake impedance for a resonator with beam tubes is shown in figure 2.7.

Fundamental theorem of beam loading

It was mentioned in section 2.1, that depending on the phase, a beam of charges looses energy by exciting fields inside structures and gains energy due to existing fields from external RF fields. This phenomenon is called *beam loading* [LS70]. Using the expression for wake function, it can be proven that as the trailing test charge approaches the leading charge

$$k = \frac{w_{\parallel}(s \to 0^{+})}{2} \tag{2.1.18}$$

This is called the *fundamental theorem of beam loading*. In his papers [Wil74], [Wil78], [WG82] and [Wil89] P. WILSON derived this relation. *This theorem relates the energy loss of a charge crossing a cavity to the cavity parameters calculated in the absence of charge*. Reformulated, the theorem reads:

THEOREM 1 *For any cavity, an ultra relativistic charged particle 'sees' only half of its own charge induced voltage.*

Before demonstrating how the above formulation is related to the energy loss and cavity parameters, we first show that this is not only true for the ultra relativistic particles, but also true for relativistic particles. We need this since heavy ions in storage rings travel with typical speeds $\beta < c$. If a point charge q_1 enters and passes out of an initially empty cavity, a beam induced voltage $U_{q\nu}$ remains in each of the ν modes. For an ultra relativistic particle, the cavity is contracted to a thin line. The induced voltage $U_{1\nu}$ appears instantaneously whenever the charge passes through the cavity. But for a relatively slow particle, the beam induced voltage travels faster than the particle itself and the finite length of the cavity cannot be ignored. It may even be that the beam induced voltage to a mode in question already changes sign before the particle has fully traversed the cavity, causing acceleration of the particle. In order to model this effect again we consider that the beam induced voltage appears instantaneously *after* the particle passed through the cavity, but this time the induced voltage has a *phase advance* θ. This phase advance accounts for the finite length and speed of the particle. Particle q_1 induces a voltage into mode ν which we write in the phasor notation:

$$\tilde{U}_{1\nu} = U_{1\nu} \mathrm{e}^{i\theta} \tag{2.1.19}$$

with

$$\theta = \frac{\omega_{0\nu} d}{\beta c} \tag{2.1.20}$$

where ω_{01} is the resonance frequency of the first mode, d is the length of the cavity, β is the relativistic factor and c is the speed of light in vacuum. If we define the voltage U_{11} itself as:

$$\hat{U}_{11} = \int_{-d/2}^{d/2} E_z \, dz \tag{2.1.21}$$

which can be interpreted as a static or frozen picture of the electric field distribution along the axis for a given mode, then by defining the *transit time factor* Λ as:

$$\Lambda(\beta) = \frac{\int_{-d/2}^{d/2} E_z \cos\left(\frac{2\pi}{\beta\lambda} z\right) dz}{\int_{-d/2}^{d/2} E_z \, dz} \tag{2.1.22}$$

we can rewrite equation 2.1.19 as:

$$\tilde{U}_{1\nu} = \hat{U}_{1\nu}\Lambda(\beta) \tag{2.1.23}$$

Sometimes in the literature, the argument of the cosine is written equivalently as $2\pi f z/\beta c$. Assuming that particle q_1 sees a fraction α of its own charge induced voltage, then the energy loss to the mode ν of the cavity would be

$$\Delta W_{1\nu} = \alpha q_1 U_{1\nu} \cos\theta = \alpha q_1 \hat{U}_{1\nu}\Lambda(\beta) \tag{2.1.24}$$

Now let a second particle q_2 with the same charge and speed follow the first one with a distance of half of the RF wavelength of the chosen mode. Same applies here for the induced voltage $\tilde{U}_{21}$ except that the particle sees a fraction of its own voltage plus all of the existing voltage from the previous particle, since the cavity was assumed to be lossless. By the time q_2 passes the cavity, $\tilde{U}_{11}$ has changed by π (see figure 2.9). So the net energy gain is

$$\begin{aligned} \Delta W_{2\nu} &= q_2 \left(U_{1\nu}\cos\theta - \alpha U_{2\nu}\cos\theta\right) \\ &= q_2 U_{1\nu}\cos\theta(1-\alpha) \\ &= q_1 \hat{U}_{1\nu}\Lambda(\beta)(1-\alpha) \end{aligned} \tag{2.1.25}$$

since $\hat{U}_{1\nu} = \hat{U}_{2\nu}$ and charges are the same. The induced field of the second charge will exactly cancel the induced field of the first so the cavity will contain no energy after the passage of both charges. According to superposition principle, we can equate ΔW_1 and

ΔW_2.

$$\begin{aligned} \Delta W_{1\nu} &= \Delta W_{2\nu} \\ \alpha q_1 U_{1\nu} \cos\theta &= q_2 U_{1\nu} \cos\theta (1-\alpha) \\ \alpha q_1 \hat{U}_{1\nu} \Lambda(\beta) &= q_2 \hat{U}_{1\nu} \Lambda(\beta)(1-\alpha) \\ \alpha &= 1-\alpha \end{aligned} \tag{2.1.26}$$

which results in $\alpha = 1/2$. The same result is obtained for ultra relativistic particles. Equation 2.1.24 becomes:

$$\Delta W_{1\nu} = \Delta W_\nu = \frac{1}{2} q_1 \hat{U}_{1\nu} \Lambda(\beta) \tag{2.1.27}$$

2.1.2 Modal parameters

Modal loss parameter

We introduced the *loss parameter* in the previous section. Similar to equation 2.1.12, the *modal loss parameter* k_ν for radiation of charge q_1 into mode ν of an empty cavity is defined as:

$$\Delta W_\nu = k_\nu q^2 \tag{2.1.28}$$

same energy loss can be expressed as:

$$\Delta W_\nu = \psi \tilde{U}_{1\nu}^2 = \psi \hat{U}_{1\nu}^2 \Lambda(\beta)^2 \tag{2.1.29}$$

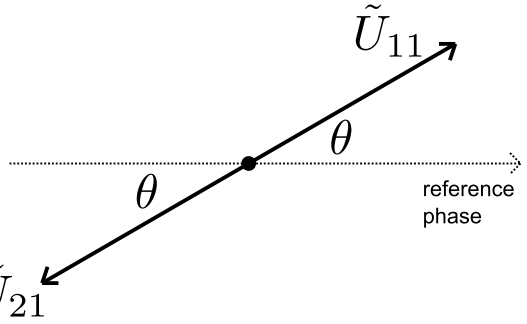

Figure 2.9: Phasor diagram for fundamental theorem of beam loading.

these two expressions together with equation 2.1.27 give us three ways to express the energy loss[5]. These expressions can be used for mathematical manipulation so that we have $\psi = 1/4k$. As a result equation 2.1.29 can be rewritten as:

$$k_\nu = \frac{\hat{U}_{1\nu}^2}{4\Delta W} \Lambda(\beta)^2 = \frac{\hat{U}^2}{4W} \Lambda(\beta)^2 = \hat{k}_\nu \Lambda(\beta)^2 \tag{2.1.30}$$

where $\hat{k}_\nu$ is the loss parameter for the frozen field distribution in the νth mode. The equation is valid no matter what the source of $\hat{U}_{1\nu}$ is and W_ν is just the corresponding stored energy in the resonator. $\hat{U}_{1\nu}$ can be determined by means of simulation as it is done for example in the computer code SUPERFISH. There, the transit time factor is also

calculated like in the equation 2.1.22 [BY06].

Modal shunt impedance and modal characteristic impedance

It was already discussed that in the parallel RLC equivalent circuit of a resonant cavity, all losses can be modelled with a real ohmic resistor connected in parallel or shunt with L and C. For each mode ν inside the resonator, one such characteristic resistance exists which we call *modal shunt impedance*. It is defined as[6]

$$R_{sh,\nu} = \frac{U^2}{P_L} = \frac{\hat{U}^2 \Lambda(\beta)^2}{P_L} = \widehat{R_{sh,\nu}} \Lambda(\beta)^2 \tag{2.1.31}$$

in units of Ohms $[\Omega]$ where again $\widehat{R_{sh,\nu}}$ can be considered as the 'frozen' shunt impedance[7]. As stated before in equation A.1.115 on the discussion of RLC circuits, the *modal characteristic impedance* on the other hand is a quantity that does not depend on lossy features of the resonator. Using equation A.1.87 we have:

$$\frac{R_{sh,\nu}}{Q} = \frac{\hat{U}^2 \Lambda(\beta)^2}{\omega_0 W} = \widehat{\left(\frac{R_{sh,\nu}}{Q}\right)} \Lambda(\beta)^2 \tag{2.1.32}$$

again measured in units of Ohms $[\Omega]$. Using this relation we can derive a new expression for the modal loss parameter in2.1.30:

$$k_\nu = \frac{\omega_0}{4} \frac{R_{sh,\nu}}{Q} = \frac{\omega_0}{4} \widehat{\left(\frac{R_{sh,\nu}}{Q}\right)} \Lambda(\beta)^2 \tag{2.1.33}$$

In practical cases k_ν is measured in units of volts per pico-Coulombs $[V/pC]$. Finally using equation 2.1.28 we have

$$\Delta W_\nu = q^2 \frac{\omega_0}{4} \widehat{\left(\frac{R_{sh,\nu}}{Q}\right)} \Lambda(\beta)^2 \tag{2.1.34}$$

which shows the energy lost to the mode ν. This equation is of practical importance since $\widehat{R_{sh,\nu}/Q}$ can be measured using the rod method which will be discussed in the upcoming chapter on the resonator design and measurement. Transit time factor Λ needs to be estimated numerically. Putting $\Lambda = 1$ defines an upper limit to all of the above values and gives a best case estimate for designs.

[6] In some literature the shunt impedance is defined as $R_{sh} = \frac{U^2}{2P_L}$ which results in smaller values (half).

[7] In some literature $R_{sh,\nu}$ is called the *effective shunt impedance* $R_{sh,\text{eff}}$ (see [Mil05] ch. 1, T. Weiland et. al.)

Example 2.1.1 *Let us consider a resonator with* $f_0 = 243.95\ [MHz]$ *i.e. a* $Q = 1130$ *and* $Q_{loaded} = 565$ *and a* $\widehat{\left(R_{sh,\nu}/Q\right)} = 42\ [\Omega]$ *i.e.* $\widehat{\left(R_{sh,\nu}/Q\right)}_{loaded} = 84\ [\Omega]$. *A single fully ionized* $^{142}Pm^{61+}$ *nucleus with a kinetic energy of* $400\ [MeV/u]$ *travels through the tube at a speed of* $0.71c$ *so that* $\lambda(0.71) = 0.815$. *From equation 2.1.34 we then have*

$$\Delta W \approx 1.02\ 10^{-24}\ [J] \approx 6.4\ \mu eV$$

and twice as much for the loaded resonator.

Equivalent circuit elements

The parallel RLC equivalent circuit is most suitable for describing a cavity (cf. section A.1.4 and [ZK98]). Keeping equation 2.1.10 in mind, for the νth equivalent RLC circuit the values for L and C can be calculated using equation A.1.94b. The relation in equation A.1.115 can be isolated for C showing that

$$\frac{1}{C} = \omega_0 \frac{R}{Q} \tag{2.1.35}$$

From equation A.1.91 we know that the maximum energy stored in the capacitor is $W_{C,max} = CU_{peak}^2/2 = q^2/(2C)$. From the equation 2.1.34 which is a result of the fundamental theory of beam loading, we know that immediately after the passage of charge, the voltage U_{peak} causes all of the energy to be stored in the capacitor. Since the perturbation is static, it can not account for the transit time factor. So energy lost to the 'frozen' characteristic impedance needs to be considered

$$\widehat{\Delta W_\nu} = q^2 \frac{\omega_0}{4} \widehat{\left(\frac{R_{sh,\nu}}{Q}\right)} \tag{2.1.36}$$

so that the following is achieved

$$\frac{1}{C_\nu} = \frac{\omega_0}{2} \widehat{\left(\frac{R_{sh,\nu}}{Q}\right)} \tag{2.1.37}$$

Comparing this to equation 2.1.35 we reach to the conclusion that for each mode ν

$$R_\nu = \frac{\widehat{R_{sh,\nu}}}{2} = \frac{R_{sh,\nu}}{2\Lambda(\beta)^2} \tag{2.1.38}$$

The value of L_ν can be calculated using equation A.1.84. Equivalent circuit elements are best described by the unloaded quantities.

Example 2.1.2 *The resonator in example 2.1.1 will have the following equivalent circuit elements for the fundamental mode (i.e.* $\nu = 1$*):* $C_1 = 195\ [pF]$ *and* $L_1 = 86\ [nH]$ *for the unloaded resonator and* $C_1 = 97\ [pF]$ *and* $L_1 = 172\ [nH]$ *for the loaded case. For both loaded and unloaded resonator* $R_1 = 23.7\ [k\Omega]$*. The resulting transfer functions are depicted in figure A.4. The unloaded bandwidth is about 373 [kHz] and the loaded bandwidth is about 745 [kHz].*

Energy exchange

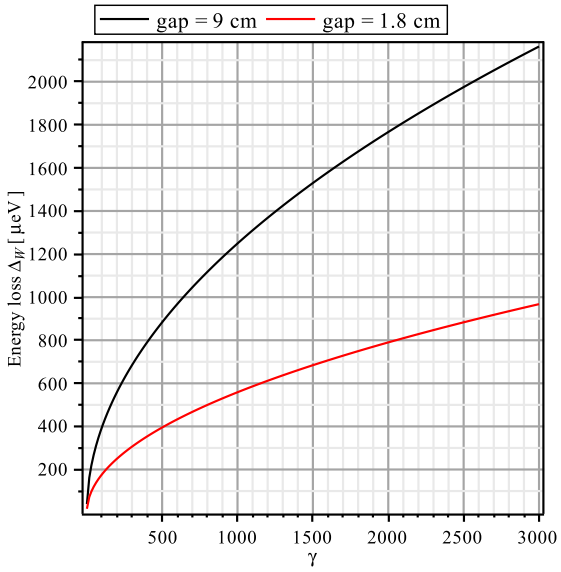

Figure 2.10: Energy loss of a bare ^{208}Pb ion due to radiation into an empty resonator.

In the previous discussion, we considered energy exchange of particles to specific modes of a resonator. The signal that is extracted from a mode via a coupling mechanism depends on how much that mode is excited by the particle. This in turn depends on how good the resonator is optimized to *collect* the energy in that mode, in other words how high the Q of that mode is.

An ultra-relativistic charged beam excites all frequencies in a resonator. On those frequencies where the resonator doesn't have a resonant mode, any excitation is maximally damped and converted to heat. As a result, all harmonics are excited. The higher the energy, the larger will be the contribution of the higher order harmonics, so that these cannot be neglected in calculations of energy loss. On the other hand, in a resonator with beam pipes, mode wave with frequencies larger than the beam cut off frequency will propagate out of it and start to travel around the storage ring and eventually form a standing wave pattern.

The calculation of energy loss has been subject of many papers since the middle of the 20th century. O. A. KOLPAKOV and V. I. KOTOV estimated the energy loss of trapped modes with the assumption that the velocity of the beam is constant and the beam is travelling on

pipe axis [KK64]. Solutions of the inhomogeneous wave equation is sought inside of the volume. For the energy lost to the fundamental mode they estimated

$$\Delta\mathscr{E}_{loss,0} = \frac{d}{4\pi\varepsilon_0}\frac{q^2}{2\varrho_{pipe}^2} \tag{2.1.39}$$

and for all trapped modes inside of the resonator

$$\Delta\mathscr{E}_{loss} = \frac{\beta^2 q^2 \gamma}{4\pi\varepsilon_0 \varrho_{pipe}} \tag{2.1.40}$$

Example 2.1.3 *Using these formulas and the numbers from example 2.1.1 and for a resonator with depth* $d = 9\ [cm]$ *and a pipe with* $\varrho_{pipe} = 12.5\ [cm]$ *we obtain for the losses due to the fundamental mode*

$$\Delta\mathscr{E}_{loss,0} = 15.5\ [\mu eV]$$

which is not the same but comparable to the results of the example 2.1.1 and due to all trapped modes below the cut off frequency in a resonator

$$\Delta\mathscr{E}_{loss} = 31.3\ [\mu eV]$$

The higher frequency components were estimated using energy loss of the particle due to *radiation*. It is the synchrotron radiation of the mirror charge on the beam pipe at the onset of entering the resonator area, where its path changes suddenly. The radiation spreads in a cone in the direction of beam motion, thereby leaving some parts of the resonator unilluminated behind. These radiations have been studied by J. D. LAWSON [Law90] and more exactly by R. B. PALMER [Pal87] and are summarised in a complete chapter in [ZK98]. There it can be found that the energy loss of the particle in a single pass limit is

$$\Delta\mathscr{E}_{loss} = \frac{F_1}{\sqrt{2}}\frac{q^2}{4\pi\varepsilon}\frac{d^{1/2}\gamma^{1/2}}{\varrho_{pipe}^{3/2}} \tag{2.1.41}$$

where d is the gap length as in figure 2.4(a) and the numerical factor F_1 is approximately 0.85 for a point charge. For a given constant configuration, the energy loss is proportional to the square root of relativistic γ. These results are only correct for ultra-relativistic particles and do not deliver proper values for lower energies. Figure 2.10 shows the energy loss of a single fully ionised ^{208}Pb atom in a range of energies. The effect of the gap length is

also visible, since with larger gap the light cone will illuminate larger portions of the front wall. But the energy loss will not diverge as the gap length grows. This has been shown by A. FALTENS in [Fal68].

Example 2.1.4 *The particle in example 2.1.1 has $\gamma = 1.42$, the formula largely overestimates an energy loss 47.3 $[\mu eV]$ for a $d = 9$ $[cm]$ gap and 21.2 $[\mu eV]$ for a $d = 1.8$ $[cm]$ gap, compared to the results in example 2.1.1 and 2.1.3.*

The third mechanism is also due to the radiation of the particle. It is caused by the radiation reaction force [Roh07]. This energy loss is extremely small in low frequency range and can readily be ignored in a heavy ion storage ring.

Relation to observation time

As it was mentioned earlier, the loss of particle energy in a structure can be described by the coupling impedance. It is possible to estimate a measure for the quantum mechanical observation time due to a structure with a known coupling impedance by using HEISENBERG's uncertainty principle in time and energy.

$$\Delta\mathscr{E}\Delta t \geq \frac{\hbar}{2} \tag{2.1.42}$$

The energy lost to one of the modes is a part that contributes to the total energy loss of the particle. In a specific structure, say a resonant pickup, the geometry is designed such that most of the energy is lost to the a certain mode, in our case the fundamental mode. This energy loss is the only source of information we have about the presence of the particle. So by using this energy for the purpose of observation, we can say, that **at least** this amount of energy was extracted from the particle, regardless of the fact that the particle may have lost more energy to higher order modes or due to other energy exchange mechanisms.

Using this minimum energy loss, we can use equation 2.1.42 to obtain a **maximum** interaction time which can be interpreted as *observation* time in quantum mechanical sense. It is noteworthy that during this time, the resonant pickup is continuously *observing* the particle regardless of the fact if the signal is being processed in later stages or not. This way it can also be concluded that a structure with larger coupling impedance observes the particle for a longer time.

Example 2.1.5 *Consider the resonator-particle system in example 2.1.1 be installed in an ideal storage ring with circumference $\Pi = 108.36$ $[m]$ (as in ESR). The observation time*

would then correspond to

$$\Delta t = 25.83\ [ps]$$

whereas a complete turn over the circumference takes 510 $[ns]$ *which is about 4 orders of magnitude larger than the observation time. Hence it is more probable that for example a nuclear decay happens during the time where the particle is not being observed, so that the particle has already changed state* before *entering the 'observation area'.*

The example above shows values that are related to the *loaded* Q value and characteristic impedance. This is obvious since the signal is usually connected to an instrument (load) for analysis.

2.2. Particle Induced Signals

The lost energy of a particle to a specific mode of a pickup can be captured by an antenna and passed to further stages for processing. Spectral analysis is needed in many aspects of the analysis of the whole particle-pickup system and the signals involved therein. The reader is referred to section A.1.2 for detailed review of some concepts in FOURIER analysis. A model of the particle-pickup system is depicted in figure 2.11. It will be discussed in the following sections in detail. It starts with the ideal process $i(t)$ and follows the signal path through to the instrument.

2.2.1 Noise processes

The noise process $n(t)$

One of the most common signals in experimental physics that has a continuous power spectrum is the thermal noise. At each given temperature, due to the thermal energy electrons in any non-ideally conducting material such as a resistor move around randomly and thereby induce a voltage at its ports. This random voltage is called thermal, JOHNSON [Joh28] or NYQUIST [Nyq28] noise. Usually thermal noise process $U_n(t)$ is *assumed* to be an ergodic process [Col00] with a flat spectrum. In reality the power spectrum of thermal noise is only nearly flat for all frequencies, but for most cases the approximation is good enough. A signal with a flat spectrum is called a *white noise*, otherwise it is called a *coloured noise*, in analogy with a spectral content of visible light. Since according to the definition,

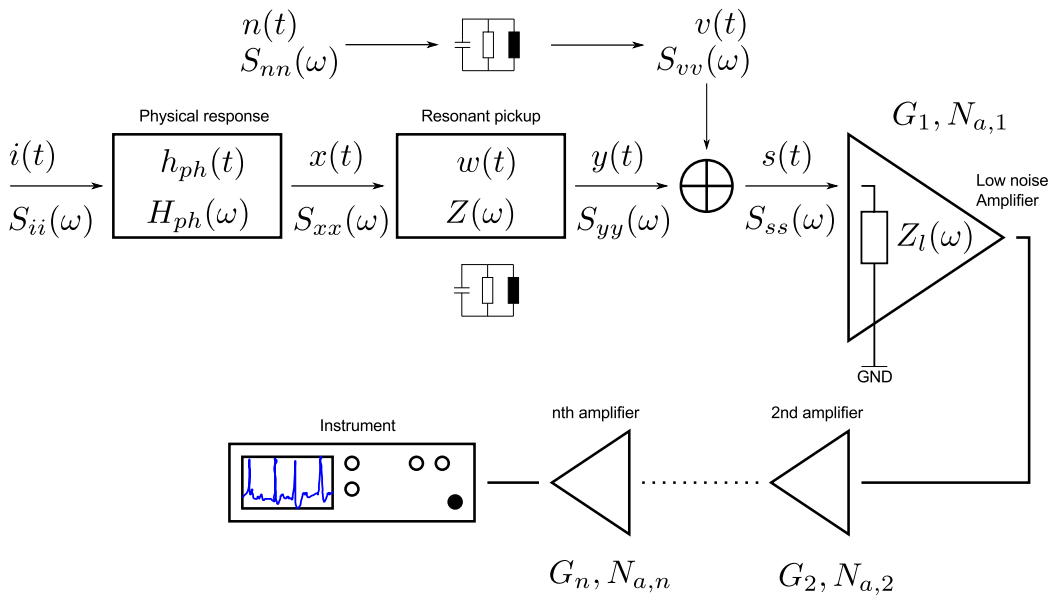

Figure 2.11: A model for the signal flow and noise in the particle-pickup-instrument system.

the spectrum is flat from $-\infty$ to ∞, then the white noise process is zero mean, which means that it doesn't have a deterministic component at all. Then from equation A.1.75 we know that $\sigma_n^2 = E[U_n(t)^2]$ which is the *mean square* voltage per unit frequency (Hz). For the thermal noise we have [Fet90]

$$S_{nn}(\omega) = \sigma_n^2 = E[U_n(t)^2] = \langle {U_n}^2 \rangle = 4k_B TR \text{ or } (2\sqrt{k_B TR})^2 \tag{2.2.1}$$

where $k_B = 1.3806488(13)\times 10^{-23}$ $[J/K]$ is the BOLTZMANN constant, T is the absolute temperature in KELVIN and R is the resistance in ohms[8]. This resistance can be the equivalent resistance of all dissipating elements in a network including losses in non ideal conductors. So if the network is short circuited to itself, the lossy elements of it will dissipate an *average*[9] power of

$$\frac{d\langle P_n \rangle(f)}{df} = \frac{U_{n,rms}^2}{R} = \frac{S_{nn}(\omega)}{R} = 4k_B T \tag{2.2.2}$$

which is independent of resistance, and is only a function of temperature per unit frequency (Hz). If the network is terminated (matched) with another load resistor R_l with the same

[8]This is the one sided PSD for positive frequencies only, otherwise the factor would be 2 instead of 4.
[9]Please also refer to section A.1.2.

value (or its complex conjugate if the impedances are complex valued)

$$R = R_l \text{ or } Z = Z_l^* \tag{2.2.3}$$

then half of the voltage is dropped across each, and the noise generated by each will be dissipated in both. In this case we have the *available noise power* as $d\langle P_n\rangle(f)/df = k_B T\ [W/Hz]$ which is approximately equal to $-174\ [dBm/Hz]$ at room temperature with $300\ [K]$. For a given bandwidth other than unit frequency the result is obtained just by the area under the $d\langle P_n\rangle(f)/df$ curve in the given bandwidth, in this special case by multiplication with Δf so that the larger the bandwidth, the higher is the background noise level. In spectrum analysers based on super-heterodyne principle there is an intermediate filter often called the *resolution bandwidth* (**RBW**) filter. The width of this filter in the frequency domain is the given Δf in the sense mentioned above. Increasing the RBW increases the noise floor since more noise power passes through the RBW filter to the next stage. In this respect, a useful relation for working with spectrum analysers is

$$\text{value in } [dBm/Hz] = \text{value in } [dBm] - 10\,log_{10}(\text{RBW}) \tag{2.2.4}$$

Colored noise process $v(t)$

A noisy resistor can be modelled as an ideal resistor in series with a voltage source that generates that noise with the voltage value described as in equation 2.2.1. Using the MAYER–NORTON theorem from the circuit theory, the noise generator can equally be modelled as a current source in parallel with an ideal resistor. To investigate the noise characteristics of the RLC circuits, we consider no other input signal other than the intrinsic noise of the resistor R itself. Referring to the figure A.3 in appendix, the resistors will be noise generators and other elements are ideal. In pioneering works of H. NYQUIST [Nyq28] and J. B. JOHNSON [Joh28], it was shown that the thermal noise due to a complex valued impedance network is related to its real part (see also [PP02]). This means

$$S_{vv}(\omega) = 2k_B T \Re\{Z(\omega)\} \tag{2.2.5}$$

Using equation A.1.100 for a resonator with one resonant mode we arrive at

$$S_{vv}(\omega) = \frac{4k_B TR}{1 + Q_p^2(\delta\omega)^2} \tag{2.2.6}$$

for the **one sided** PSD where R is related to the shunt impedance of that mode according to equation 2.1.38. This equation is equivalent to 2.2.1 at resonance frequency that means the resonator shows the room temperature on top of its noise spectral density curve, whereas the noise is suppressed for frequencies located otherwise. The whole shape of the noise spectral density depends on all involved resonant modes as was shown in equation 2.1.10. The overall shape will have peaks in frequency domain similar to that of figure 2.7.

2.2.2 Schottky signals

Shot noise was first explained by W. SCHOTTKY [Sch18] while he was studying random fluctuations in vacuum tubes. Meanwhile the application has been extended to many areas of physics and applied mathematics. The SCHOTTKY noise in the mathematical sense is a *yes/no* process similar to BERNOULLI or POISSON processes that can be written as

$$x(t) = \sum_{i=-\infty}^{\infty} h_{ph}(t - \mathbf{t_i})$$

where $\mathbf{t_i}$ are the so called POISSON points and $x(t)$ can be described as the output of a linear system $h_{ph}(t)$ to the input process

$$i(t) = \sum_{i=-\infty}^{\infty} \delta(t - \mathbf{t_i})$$

Many physical applications can be covered such as the movement of electrons in semiconductor diodes. An important characteristic is the directionality of the movement of the particles for example over a voltage barrier across a PN junction diode that distinguishes it from BROWNIAN motion. In a storage ring, we have a similar situation whenever particles pass through a specific region of interest. Here the POISSON points for a large number of particles occur periodically but as we will see with random phase distributed around 2π around the ring. SCHOTTKY signals are affected by microscopic and macroscopic correlations (see [Cha84]), the former being caused by interaction of the particles with the environment, the latter a direct consequence of the external 'bunching' of the beam for example due to an RF cavity. A very good introduction on SCHOTTKY noise analysis is provided in [Cas09]. There, the corpuscular nature of SCHOTTKY noise is compared to the sound of small grains falling on a metal plate.

The input process $i(t)$

One way of detecting particles in an accelerator beam tube is putting metallic plates inside of the tube basically in the shape of a parallel plate capacitor. Each time a charged particle passes through that region of the tube, it induces an electric charge on the plates same as the charge depicted in figure 2.5. According to equation 2.1.9 the charge distribution depends on the transversal distance of the particle from each of the plates, and in principle due to the intensity of the electric fields normal to the plate, higher charges are induced on that plate. Using two sets of horizontal and vertical pairs of plates and differential mode amplifiers, the transversal position of the particle beam can be obtained. The information from one set of plates can be used to extract the intensity of the beam. An example of such a detector is depicted in figure 2.12. It is the picture of the parallel plate SCHOTTKY detector mounted into the heavy ion storage ring ESR at GSI in 1991 [Sch91]. The horizontal and vertical plates are clearly visible on the picture.

There exist many short term transient fluctuations of the surface charge distribution of the plates during and after the passage of a particle. The overall or integral effect of the charge distribution is an electric pulse which depends on the longitudinal extension of the plate along the particle's flight path and of the charge of the particle.

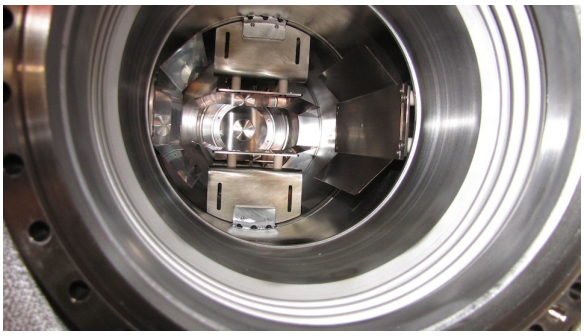

Figure 2.12: SCHOTTKY pickups at GSI [Sch91]. Photo: P. Petri.

It was mentioned that the resulting signal due to an ultra-relativistic particle resembles a DIRAC delta pulse. For a single charge q that traverses a specific position in the storage ring with a revolution frequency $f_r = \omega_r/(2\pi)$, there will be a current that is only present as a short spike every time the particle passes. The resulting time dependency is

$$i(t) = q \sum_{m=-\infty}^{\infty} \delta(t - m\,T_r) \tag{2.2.7}$$

This is called the *delta function approximation* in the literature. The current due to one particle is deterministic and has no random components no matter what the starting phase of the particle is, it is assumed not to change in a given experiment. The FOURIER transform of this current shows a peak at ω_r and subsequent peaks at multiples of it (*harmonics*). Adding one more particle that rotates 180° behind the first particle will show a determinis-

tic fundamental frequency at 2 ω_r. Number of particles can be increased up to N. Now, if the angle Θ_j between the added new particles and the first particle is not deterministically known, but in different experiments have different values between 0 and 2π, i.e. statistically uniformly distributed in that range, then a new set of frequencies ω_j appear in the spectrum for every particle j, but this time the fundamental frequency will be again ω_r and the new frequencies will be in its neighbourhood. One speaks of a *coasting beam* that rotates at a fundamental revolution frequency. Adding this random phase in the expression in equation 2.2.7 we have:

$$\begin{aligned} i(t) &= q\sum_{j=1}^{N}\sum_{m=-\infty}^{\infty}\delta\left(t-\frac{m}{f_r}+\Theta_j\right) \\ &= q\sum_{j=1}^{N}\sum_{m=-\infty}^{\infty}\delta\left(\omega_j t-2\pi m+\Theta_j\right) \\ &= q\sum_{j=1}^{N}\sum_{m=-\infty}^{\infty}f_j\exp\left(im(\omega_j t+\Theta_j)\right) \\ &\quad or \\ &= q\sum_{j=1}^{N}f_j+2q\sum_{j=1}^{N}\sum_{m=1}^{\infty}f_j\cos(m\omega_j t+m\Theta_j) \\ &= I_B+i_S(t) \end{aligned} \tag{2.2.8}$$

where in the last step we used the trigonometric FOURIER series of equations A.1.54 and A.1.55 and used the fact that since the signal centred on the δ pulse is an even function, the coefficients b_n are all zero. I_B is the macroscopic beam current and the i_S is the random current fluctuation. Since ω_j are all in the neighbourhood of ω_r, SCHOTTKY spectrum consists of bands around the harmonics $m\omega_r$. In the literature [Cha84] an equivalent argument is used that in the space of real numbers all signals have a strength of $2qf_j$ except those at band $m=0$, which results in a DC component with all same zero phase that adds up to result in I_B. $i(t)$ is a random process since Θ_j is a randomly distributed

variable. Its expected value is

$$\begin{aligned}\mathbb{E}\left[i(t)\right] &= \mathbb{E}\left[q\sum_{j=1}^{N} f_j + 2q\sum_{j=1}^{N}\sum_{m=1}^{\infty} f_j\cos(m\omega_j t + m\Theta_j)\right] \\ &= q\sum_{j=1}^{N} f_j + 2q\,\mathbb{E}\left[\sum_{j=1}^{N}\sum_{m=1}^{\infty} f_j\cos(m\omega_j t + m\Theta_j)\right] \\ &= q\sum_{j=1}^{N} f_j + 0 = qf_rN = I_B\end{aligned} \tag{2.2.9}$$

where the cosine term vanishes due to averaging. The last step is due to the fact that the area under the curve cancels due to symmetry [Cha84]. This equation can be used to determine the number of particles for a known beam current, for example if the macroscopic current is exactly determined by a calibrated DC current transformer. The current fluctuation term i_S can be decomposed for $f_j = f_r + \Delta f_j$

$$\begin{aligned}i_s(t) &= 2qf_r\sum_{j=1}^{N}\sum_{m=1}^{\infty}\cos(m\omega_j t + m\Theta_j) + 2q\sum_{j=1}^{N}\sum_{m=1}^{\infty}\Delta f_j\cos(m\omega_j t + m\Theta_j) \\ &= 2qf_r\sum_{j=1}^{N}\sum_{m=1}^{\infty}\cos(m\omega_j t + m\Theta_j)\left[1 + \mathcal{O}(\Delta f/f_r)\right] \\ &\approx 2qf_r\sum_{j=1}^{N}\sum_{m=1}^{\infty}\cos(m\omega_j t + m\Theta_j)\end{aligned} \tag{2.2.10}$$

where since $\Delta f_j \ll f_r$ the higher order term can be neglected [Cha84]. It is interesting to notice that these higher order terms actually show a complete set of SCHOTTKY lines of their own, but they are very insignificant in their strength. The final form of the current is

$$i(t) = q\sum_{j=1}^{N} f_j + 2qf_r\sum_{j=1}^{N}\sum_{m=1}^{\infty}\cos(m\omega_j t + m\Theta_j) \tag{2.2.11}$$

In order to obtain an expression for the PSD of the process we need the autocorrelation

function

$$
\begin{aligned}
& r_{ii}(t+\tau, t) \\
& = \mathbb{E}[i(t+\tau)i(t)] \\
& = q^2 \left(\sum_{j=1}^{N} f_j \right)^2 \\
& + 4q^2 \mathbb{E} \left[\sum_{j=1}^{N} \sum_{m=1}^{\infty} \sum_{k=1}^{N} \sum_{n=1}^{\infty} f_j f_k \cos\left(m\omega_j (t+\tau) + m\Theta_j \right) \cos\left(n\omega_k t + n\Theta_k \right) \right] \\
& = q^2 f_r^2 N^2 + q^2 f_r^2 \sum_{j=1}^{N} \sum_{m=1}^{\infty} \left(\mathrm{e}^{im\omega_j \tau} + \mathrm{e}^{-im\omega_j \tau} \right) \\
& = q^2 f_r^2 N^2 + 2q^2 f_r^2 \sum_{j=1}^{N} \sum_{m=1}^{\infty} \cos(m\omega_j \tau) \\
& = r_{ii}(\tau)
\end{aligned}
\tag{2.2.12}
$$

where the approximation in equation 2.2.11 and several trigonometric manipulations were used (please refer to section A.1.5). The above relation has two messages: Firstly, the resulting function is dependent only on the time difference τ, this means that the process is *at least* stationary up to the second order. In fact this process is a strict sense stationary random process as described elsewhere [PP02]. Secondly, the autocorrelation function which is a measure of power, consists of a DC power, i.e. I_B^2 together with a power centred around each harmonic. These are called SCHOTTKY *bands*. It shows that the *integrated* SCHOTTKY noise spectral density in each band does not depend on the harmonic number m and is the same for all, i.e.

$$\langle I_s \rangle^2 = 2q^2 f_r^2 N = 2q f_r I_B \tag{2.2.13}$$

where we used equation 2.2.9 in the last step. This equation can be used to determine the macroscopic current using calibrated beam spectra as will be discussed in section 4.2.2.

Next step is the PSD of this process which can be obtained by FOURIER transformation.

$$\begin{aligned} S_{ii}(\omega) &= \mathscr{F}\{r_{ii}(\tau)\} \\ &= q^2N^2f_r^2\delta(\omega) + \pi q^2 f_r^2 \sum_{j=1}^{N}\sum_{m=1}^{\infty}\left[\delta(\omega + m\omega_j) + \delta(\omega - m\omega_j)\right] \\ &= S_{I_BI_B}(\omega) + S_{i_Si_S}(\omega) \end{aligned} \tag{2.2.14}$$

or

$$S_{ii}(f) = q^2N^2f_r^2\delta(f) + q^2 f_r^2 \sum_{j=1}^{N}\sum_{m=1}^{\infty}\left[\delta(f + mf_j) + \delta(f - mf_j)\right]$$

This expression contains the following information: The PSD consists of a DC component which is proportional to charge, number of particles and revolution frequency. This component is everywhere zero except at zero frequency. All other components are covered by the second term, which indicates that for every particle there are two delta pulses with arbitrary height but with finite power placed symmetric around the multiples of the revolution frequency or harmonics. The deltas will be placed farther apart with larger harmonic number. This in turn means that the extent which contains all of the deltas of all particles in that band, widens (multiplied by m) as harmonic number grows. This fact together with the above mentioned constant power in each band has a consequence that the peak power intensity also decreases as shown schematically in figure 2.13. Another interesting point from the relation is that the power in every SCHOTTKY band is smaller than the DC power by factor of $1/N$. Finally the bands can get so wide, that their SCHOTTKY lines overlap. This is not a desirable situation for experiments since correct identification of the SCHOTTKY line becomes more difficult.

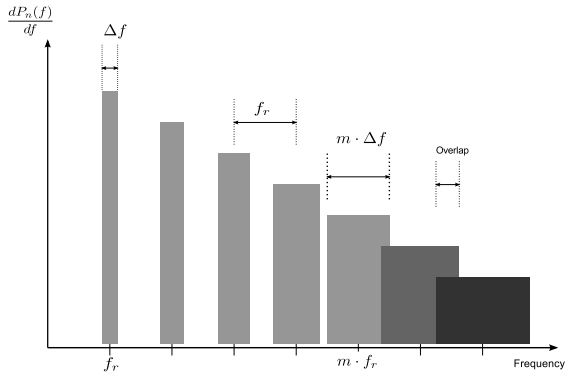

Figure 2.13: Schematic view of SCHOTTKY bands vs. frequency.

Example 2.2.1 *Let the single particle in example 2.1.1 be He-like, that is* $^{142}Pm^{59+}$ *with the same energy and speed. The resonator center frequency is tuned to* 244.963 $[MHz]$ *so that we see* SCHOTTKY *lines at* 124^{th} *harmonic (see figure 4.3 on page 82). The revolution frequency is* $f_r = 1.975\ [MHz]$. *It decays to the ground state of bare* ^{142}Nd *with a* $\Delta f \approx 1.6\ [kHz]$ *or*

equivalently only 13 $[Hz]$ *at the fundamental harmonic. Choosing a high harmonic number increases the frequency resolution, but it may case* SCHOTTKY *band overlap if the harmonic is too high. In this case the highest possible harmonic is the* 153700^{th}*. This number is far above any measurable scales anyway.*

The processes $s(t)$

In the previous section we discussed the case for the ultra-relativistic particle. We saw also in section 2.1.1 equation 2.1.9 that the linear charge distribution depends on the speed of the particle. Looking at the equation 2.1.8 we realize that since the strength of the radial electric field increases with particle's relativistic gamma factor. For the same tube radius, the resulting electric field would be as if it is originating from a new charge $q' = \gamma q$. Hence the system h_{ph} can be defined as a constant factor that is multiplied with the charge

$$H_{ph}(\omega) = \gamma \tag{2.2.15}$$

In the following we only consider the zero mean process $i_S(t)$ since we are interested in the SCHOTTKY fluctuations in the harmonic bands. The choice of the zero mean process also simplifies the calculation of its passage through LTI systems, otherwise the mean must always be taken into account[10]. The impedance of the equivalent parallel circuit of the resonator was introduced in equation A.1.100. For the overall behaviour of a resonator with many resonances one should consider the sum over all resonance bands as in equation 2.1.10. But as we will soon see, only the first resonance is enough for the description of the signal path.

The process $s(t)$ is the input to the first amplification stage being the addition of the signal and noise processes.

$$\begin{aligned} S_{ss}(\omega) &= S_{vv}(\omega) + S_{yy}(\omega) \\ &= S_{vv}(\omega) + S_{xx}(\omega)|Z(\omega)|^2 \\ &= S_{vv}(\omega) + S_{i_S i_S}(\omega)|H_{ph}(\omega)|^2|Z(\omega)|^2 \end{aligned} \tag{2.2.16}$$

[10]Details on this can be found in standard textbooks on digital signal processing such as [Zou10].

2.2.3 Single particle power and signal to noise ratio

The pickup is designed to work in the fundamental mode with the desired operating point being exactly on top of the resonance curve where the fastest transient behaviour and largest oscillation amplitudes are present (see figure A.6). It is interesting to find out what would be the ratio of the signal power to the noise level. In a typical experiment, one of the harmonics is chosen so that the desired spectral line actually is on top of the resonance curve (e.g. figure 3.13). If it is not, there are usually possibilities to tune the resonance frequency of the pickup with plungers (figure 3.2) so that this becomes the case. So this conditions requires that $\omega = m\omega_j \approx \omega_0$. With that condition and also by using equation equation 2.1.38, S_{vv} in equation 2.2.6 reduces to $4k_BTR$. The resonator response reduces to the pure real value R. The process $S_{i_S i_S}(f)$ reduces to $q^2 f_r^2 N$ for the given SCHOTTKY band that is on the resonance. Finally for the equation 2.2.16 we have:

$$S_{ss}(mf_j) = 4k_BTR + S_{yy}(mf_j) \tag{2.2.17}$$

with $S_{yy}(mf_j) = \gamma^2 q^2 f_r^2 N R^2$. The **single sided** average power for a single particle is then

$$\langle P \rangle = 2\frac{S_{yy}(mf_j)}{R} = 2\gamma^2 q^2 f_r^2 R \tag{2.2.18}$$

so that we have

$$SNR = \frac{S_{yy}(mf_j)}{S_{vv}(mf_j)} = \frac{1}{2}\frac{\gamma^2 q^2 f_r^2 R}{k_B T} \tag{2.2.19}$$

The same result can be obtained in time domain using equation A.1.110 which describes the single particle signal power on resonance and the fact that $I_p = 2\gamma q f_r$ from equation 2.2.11 we have

$$\langle P \rangle = 2\gamma^2 q^2 f_r^2 R \tag{2.2.20}$$

The average thermal noise power is according to equation

$$\langle P_n \rangle = 4k_BT \tag{2.2.21}$$

so that

$$SNR = \frac{\langle P \rangle}{\langle P_n \rangle} = \frac{1}{2}\frac{\gamma^2 q^2 f_r^2 R}{k_B T} \tag{2.2.22}$$

which is the same as expression above. Now we have to differentiate between the two cases of unloaded and loaded circuits. Using equation 2.1.38 we have for the unloaded

circuit

$$\langle P \rangle = \gamma^2 q^2 f_r^2 \widehat{\left(\frac{R_{sh,1}}{Q}\right)} Q \tag{2.2.23}$$

$$SNR = \frac{1}{4} \frac{\gamma^2 q^2 f_r^2}{k_B T} \widehat{\left(\frac{R_{sh,1}}{Q}\right)} Q \tag{2.2.24}$$

where we intentionally introduced a dependency on Q in order to relate it to measureable parameters. For the loaded circuit we have $\widehat{R_{sh}}/2$ parallel with the load resistor R_l so that

$$\langle P \rangle = \frac{2\gamma^2 q^2 f_r^2 R_l \widehat{\left(\frac{R_{sh,1}}{Q}\right)} Q}{R_l + \widehat{\left(\frac{R_{sh,1}}{Q}\right)} Q} \tag{2.2.25}$$

$$SNR = \frac{1}{2k_B T} \frac{\gamma^2 q^2 f_r^2 R_l \widehat{\left(\frac{R_{sh,1}}{Q}\right)} Q}{R_l + \widehat{\left(\frac{R_{sh,1}}{Q}\right)} Q} \tag{2.2.26}$$

It is arbitrary to either use the loaded or unloaded Q in this expression.

Example 2.2.2 *Consider the resonator in example 2.1.1. The given data for the particle leads to a revolution frequency $f_r \approx 1.978$ $[MHz]$ which in turn leads to the harmonic number $m = 124$. At room temperature the unloaded circuit leads to a signal power of*

$$\langle P \rangle = -134.4 \; [dBm]$$
$$SNR = 33.4 \; [dB]$$

The same configuration delivers following values for the loaded resonator with a load resistor of 50 $[\Omega]$:

$$\langle P \rangle = -161.2 \; [dBm]$$
$$SNR = 6.6 \; [dB]$$

The amplifier chain

The first amplifier in the signal chain plays an important role in the overall noise analysis due to the fact that the noise factor of the first amplification stage has a large impact on the overall noise figure of the system. In telecommunications, this effect is known as the FRIIS formula for the total noise factor [Fri44], which has the following form:

$$F_{total} = F_1 + \frac{F_2 - 1}{G_1} + \frac{F_3 - 1}{G_1 G_2} + \frac{F_4 - 1}{G_1 G_2 G_3} + \cdots \tag{2.2.27}$$

where

$$F_i = \frac{SNR_{in,i}}{SNR_{out,i}} = \frac{N_{a,i} + G_i N_{i-1}}{G_i N_{i-1}} \text{ for } i = 1, 2, \cdots \tag{2.2.28}$$

is the *noise factor* (the ratio between input and output signal to noise ratio) and G is the *gain factor* of each amplifier stage i. $N_{a,i}$ is the noise added by each stage and N_i is the output noise of each stage. This relation can be rewritten as $F_{total} = F_1 + (F_{other} - 1)/G_1$ so the overall noise factor is low if the noise factor of the first stage is low and its gain is high. The noise factor is a measure of how much any amplifier stage adds to the noise level while amplifying both signal and noise simultaneously. This relation is very well depicted in a figure in [Tec10]. Noise power can be added since they are uncorrelated. The noise power at the output of second stage is the thermal noise due to the resistor amplified by both amplifiers + N_{a1} amplified by the second amplifier + the N_{a2}. For the first stage we have $N_i = N_{th} = k_B T \Delta f$. The noise factor F is usually given in decibel and is called *noise figure* (NF) NF $= 10\ log_{10} F$. Often the same quantity is described by the effective *input noise temperature* T_e which is equal to [Tec10]

$$T_e = T_0(F - 1) \tag{2.2.29}$$

where T_0 is the standard temperature 290 $[K]$ for defining noise factor as adopted by an IEEE standard [H$^+$63]. When using noise figure, one must take care that gains are also expressed in decibels. The noise figure of passive stages is taken equal to their loss, their gain and noise figure can be combined with a previous active component (see e.g. [Lya12]) in order to reduce the steps needed to calculate the FRIIS equation.

Example 2.2.3 *The system in figure 3.4 can be simplified to 3 stages (when the third amplifier is in the signal path) or 2 stages (when the 3rd amplifier is out of the signal path). For the former case we have* $G_{total} = 77.5\ [dB]$ *and* $NF_{total} = 1.95\ [dB]$ *and for the latter case*

$G_{total} = 57.5\ [dB]$ *and* $NF_{total} = 2.05\ [dB]$.

Example 2.2.4 *Using the information in examples 2.1.1, 2.2.2 and 2.2.3 what is the total signal power for a single particle and the total signal to noise ratio?*

Using equation 2.2.28 for the loaded case and using the third amplifier stage the values for one particle but with either q, 2q or 3q charge are listed in table 2.2. The measured values are taken from figure 4.5 on page 83.

	Calculated		Measured	
Charge of Nucleus	$\langle P \rangle\ [dBm]$	$SNR\ [dB]$	$\langle P \rangle\ [dBm]$	$SNR\ [dB]$
q	-83.5	4.65	-84	8
2q	-77.7	10.65	-81	11
3q	-74.1	14.2	-74	18

Table 2.2: Approximate calculation and measurement values of particle powers and SNR. Third amplifier in the chain of figure 3.4 is turned on. See also figure 4.5 on page 83.

If the condition in equation 2.2.3 is not satisfied, then part of the noise power will be reflected at the load and will return to the source causing a *standing wave pattern*. The value of reflection coefficient is

$$\Gamma = \frac{Z - Z_l}{Z + Z_l} \tag{2.2.30}$$

which is a complex quantity showing magnitude and phase of reflection. The condition in equation 2.2.3 corresponds to $\Gamma = 0$. The available noise power will then be reduced by the amount of mismatch.

$$\frac{d\langle P_n \rangle(f)}{df} = k_B T(1 - |\Gamma|^2) \tag{2.2.31}$$

From equation A.1.114 we know that the coupling factor k is the ratio of the power loss in the external circuit to the internal circuit. This means $R_l = kR$. Dividing both sides by $1 + iQ(\delta\omega)$ results in $Z = Z'$ where $Z' = kZ$. Putting this into the equation for Γ and using equation 2.1.38 we see that for critical coupling (i.e. $k = 1$) we have

$$\Gamma = \frac{kR - R_l}{kR + R_l} = \frac{2R_l - \widehat{\left(\frac{R_{sh,1}}{Q}\right)Q}}{2R_l + \widehat{\left(\frac{R_{sh,1}}{Q}\right)Q}} \tag{2.2.32}$$

Example 2.2.5 *For the resonator in example 2.1.1 and a load resistance of* $R_l = 50\ [\Omega]$ *we have* $\Gamma = 0.995$

2.2.4 Spectrum estimation and multitaper

The easiest way to determine the frequency content of a signal is to use a *band pass filter* (e.g. an RLC filter) and to sweep its resonance (also called *center*) frequency between two frequencies f_0 and f_1. Ideally, if the response of the filter has the shape of a square, with an amplitude of unity and an infinitesimally small bandwidth δf it will let the amplitude on that frequency content through and suppress all other frequency contents. In the language of linear algebra we would be extracting the projections in the frequency domain. This voltage will give us the power content of the signal when measured over an ideal 1Ω resistor and can be shown on a display. For dynamical signals, i.e. generally non-stationary signals, we should repeat the measurement again and again, so that each time a new snapshot of the frequency content is obtained. This is basically how old fashioned analogue spectrum analysers worked. The point that the signal may at least be stationary during the sweep time is needed, since after the filter passes one frequency f_1 and is now at frequency $f_2 > f_1$, any fast transient change in the signal at frequency f_1 will not be seen. Meanwhile digital signal processing is dominant in almost all areas of experimental physics. Stronger computation powers of the instruments give rise to the so called *real time spectrum analysers*, which have a more sensitive transient response due to simultaneous processing of different sections of time data.

Due to the nature of stochastic signals, their spectra cannot be determined a priori, and even afterwards it is not guaranteed that signal components will appear as often. So it is common practice to talk about stochastic parameters such as mean, variance, bias and *spectrum estimation* when dealing with such signals. One of the common misunderstanding in the concept of estimation is when it comes to the usage of computer based analysis of a random signal or a signal with random components, say by frame by frame data acquisition. Of course just a FOURIER transformation of each frame will show us the frequency content of that frame at that time. But due to its stochastic nature, a sample sequence of the signal might contain absolutely no information about its true frequency content so we don't have an overall view of the signal characteristics and so no prediction power, which is indeed needed if we want to process the random signal say by digital filtering. Stationary random signals or those which can be assumed stationary over the period of interest are suitable for the estimation process. Another misinterpretation is sometimes the use of

averaging instead of estimation. Averaging several sample functions (ensemble averaging) as it can be done in most instrument has a visual smoothing effect, but it doesn't really help with stochastic signals since some signal components that don't appear often will be attenuated. Averaging is of course very useful, when it comes to deterministic signals that are hidden in random noise.

Estimators can be classified into parametric and non parametric types. If the characteristics of the system where the signal is going through is known, then by modelling that system with a parametric estimator, very good spectrum estimation can be achieved. In the example of the temperature in the green house it is known that the temperature at each time depends on the temperature at a previous point in time. This behaviour is a consequence of the system (the green house in this case) and not the signal itself. If a description of the system is not possible, then *non parametric estimators* are the best choice.

Estimators are characterized by their *bias* and *variance*. The former describes how far the expected value of the estimator is from the true mean and the latter describes how much the estimated spectrum fluctuates around it. Usually the bias and variance are inversely proportional, although in the ideal case it is always desirable to have both as low as possible in order to estimate the true spectrum the best way. The simplest non parametric estimator is the *Periodogram* which was introduced in 1898 [Sch98]. For an N-point sample function $X_N(t)$ of a stochastic process $X(t)$ it is defined as the normalized square of its (finite) FOURIER transform [Zou10].

$$I_{XX}^N(\omega) = \frac{1}{N}|\mathscr{F}_N\{X(t)\}|^2 \tag{2.2.33}$$

where $\mathscr{F}_N$ is the N-point finite FOURIER transform. Other combinations and variants have been developed over the years.

A recent estimation technique which tries to lower variance is the *multitaper* method which was used in this work. It was first introduced by THOMSON in 1982 [Tho82]. A thorough description can be found in the work of PARCIVAL and WALDEN [PW93] and a good introduction in [San10]. The mean of the periodogram in equation 2.2.33 for a zero mean random process $X(t)$ is [Zou10]

$$E\left[I_{XX}^N(\omega)\right] = \frac{1}{2\pi}\int_{-\pi}^{\pi} S_{XX}(\omega)\,\frac{1}{N}\left|\Delta^N(\omega-\lambda)\right|^2 d\lambda \tag{2.2.34}$$

where

$$\Delta^N(\omega) = \sum_{n=0}^{N-1} \mathrm{e}^{-i\omega n} = \frac{\sin(\omega N/2)}{\sin(\omega/2)}\,\mathrm{e}^{-i\omega(N-1)/2} \tag{2.2.35}$$

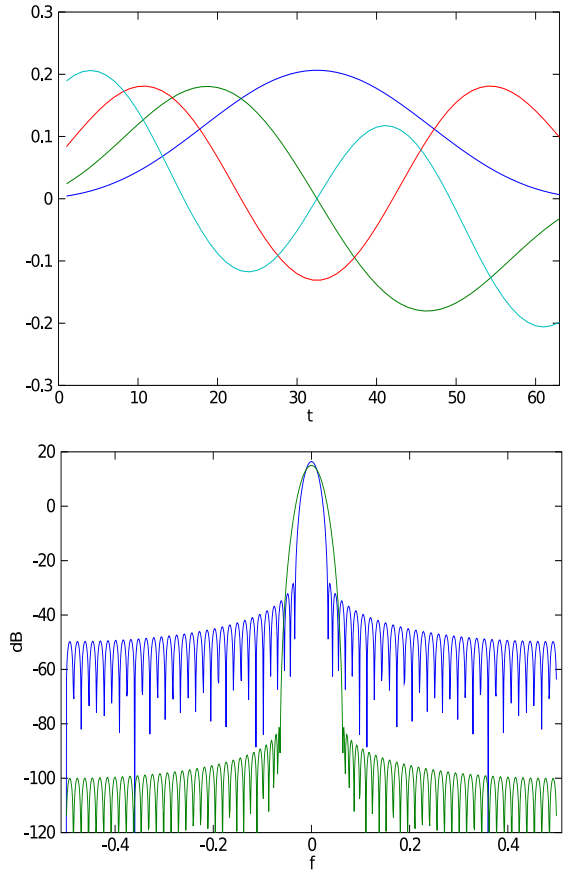

Figure 2.14: The first four of DPSS for $n = 64$ and $nW = 2$, blue line: 1st, green line: 2nd, red line: 3rd and cyan: 4th sequence (top). The first eigenspectrum for $n = 64$ and different nW. Blue line: $nW = 2$ and green line: $nW = 4$ (bottom) taken from [San10].

is the FOURIER transform of a rectangular window. The above relation shows that the mean of the estimator is the convolution of the psd of the signal with the rectangular window in frequency domain. According to fundamentals of FOURIER analysis this corresponds to multiplication in time domain. This is also called *windowing*, or in the context of multitaper analysis, *tapering*. If the rectangular window is plotted versus frequency, one can see that its side lobes are actually very high and contribute to energy leakage. In order to overcome that, other windows may be used. In the multitaper analysis, the (discrete) time domain data is windowed several times by different sequences called *tapers*. The resulting *tapered* sequences are then averaged directly or by weighted average to give the final result. The suitable taper sequences are the so called *discrete prolate spheroidal sequences* (**DPSS**) which are also known as SLEPIAN sequences [Sle78]. For a given sequence length n these sequences maximize the energy in a given normalized bandwidth W in frequency domain. This is an eigenvalue problem where the eigenvalues correspond to the energy concentration in the frequency interval $[-W, W]$. Corresponding to the largest eigenvalue, there is the first eigenvector which is also the first DPSS and so on. So all sequences are by definition orthogonal to each other. The quantity nW is called the *time-bandwidth product*. A plot of the first four DPSS for $n = 64$ and $nW = 2$ is depicted in figure 2.14. It can be seen from the figure that each sequence has a different emphasis on different sections of time signal. Not all eigenvalues are suitable for multitaper since after a certain number ($2nW$), eigenvalues start to become very small so in practice the first $K < 2nW$ eigenvalues λ_k and their corresponding DPSS h_k are used. Width of the main lobe defines the resolution, the narrower the main lobe is, the higher is the resolution and by contrast, a large window 'smears' the

resulting estimate. The side lobes are responsible for leakage of signal energy. The higher the side lobes are, the larger is the overall bias. There is a trade off between the two quantities such that increasing the resolution increases the leakage as well. The spectrum of the first sequence (the first *eigenspectrum*) is depicted in figure 2.14 for different values of time-bandwidth product. Finally, since every eigenspecturm is orthogonal to every other, they can be averaged without increasing the overall bias [San10]. The averaging is usually done by weighting such that $\sum_k w_k = 1$

$$\tilde{S}_{XX}^{N}(\omega) = \sum_{i=1}^{K} w_k \left| \mathscr{F}_N\{h_k(t)X(t)\} \right|^2 \tag{2.2.36}$$

with

$$w_k = \frac{\lambda_k}{\sum_{i=0}^{K-1} \lambda_i} \tag{2.2.37}$$

If equal weighting is desired, then obviously $w_k = 1/K$ can be used.

CHAPTER 3

THE RESONANT PICKUP

In the following chapter, mechanical design, simulation results and electrical properties of the resonator are discussed.

3.1. Design Aspects

The pickup is designed based on a pill box resonator with attached beam pipes as schematically shown in figure 2.4(a). It is made of two half-cylinders out of cast steel. Some mechanical dimensions are listed in table 3.1. Inside, the half-cylinders are coated with a

Resonator Depth	9 [cm]
Resonator Radius	30 [cm]
Thickness of the ceramic	1.3 [cm]
Metallic gap length	1.8 [cm]
Beam pipe radius	12.5 [cm]

Table 3.1: Important mechanical dimensions of the resonator.

copper layer. The two halves are air-filled and are mounted around a ceramic gap which is fixed on the evacuated beam pipe. The ceramic holder shields the ceramic and exposes only 1.8 cm of it. The beam pipe is made of stainless steel and so is the ceramic gap holder. A bellow section is connected to the gap holder for ease of installation into the ring. Each of the half-cylinders can be taken apart in order to expose the gap during the heating or for shorting the gap in high current experiments where the resonator is not needed. Mechanical junctions between ceramic gap holder and the half-cylinders are doubly RF shielded. On the inner side contact springs are used for better electrical connection, on the outer

side and between the interfaces special wire wound rubber bands are placed inside vanes. These RF rubber bands are pressed against metal surfaces whenever the screws are tight. Plungers are also shielded with contact springs and flanges for loop antenna are tightened with usual CF copper rings as used in the accelerator vacuum technology. The ceramic gap, the loop antenna and one of the plungers are depicted in figure 3.2. Figure 3.3 shows the resonator before installation on a test bench. The ceramic rod in the center was used for the measurement of the longitudinal shunt impedance of the device as we will discuss in section 3.3. The installation location of the pickup into the ESR ring is depicted in figure 1.2. Since the screws of the half-cylinders are tightened along the radial direction, surface currents are least disturbed in the fundamental mode (compare with figure 3.5). The same feature causes a resistive path along for surface currents of the higher order modes, thereby causing a natural damping for these mode.

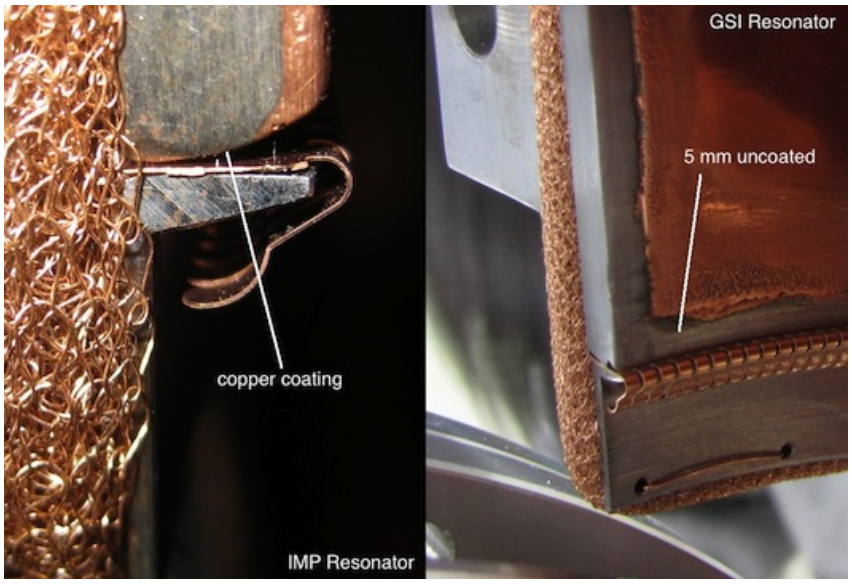

Figure 3.1: Improved copper coating of the IMP resonator (left) compared with the coating of GSI resonator (right). Photo: P. Petri

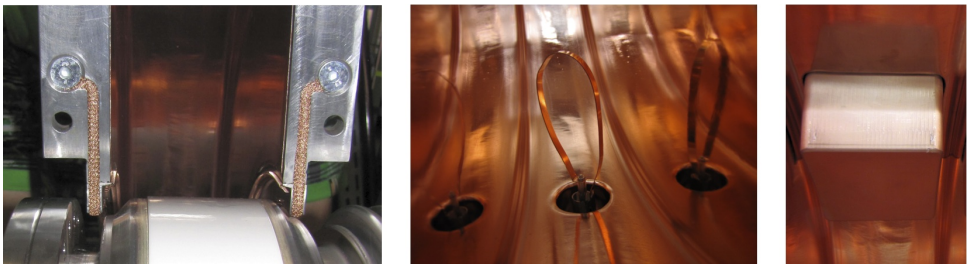

Figure 3.2: Ceramic gap, magnetic loop and one of the two plungers. Photo: P. Petri

Unfortunately, the large diameter of the beam pipe was a construction constraint that was imposed by the structure of the ESR (and the CSRe) ring at the specific installation point. This affected the overall size of the structure and therefore its operation frequency. The choice of frequency depended on many parameters. On the one hand, higher frequencies are desirable to achieve higher frequency resolutions (cf. section 4.1. But at higher frequencies the dimensions of the resonator would become small, and since the beam pipe is comparatively large, the overall Q will decrease. On the other hand the fundamental frequency must lie below the cut-off frequency of the beam pipe (around 918 MHz). The IMP resonator is built using identical mechanical features except an improved copper coating on the edges of the half-cylinders as shown in figure 3.1.

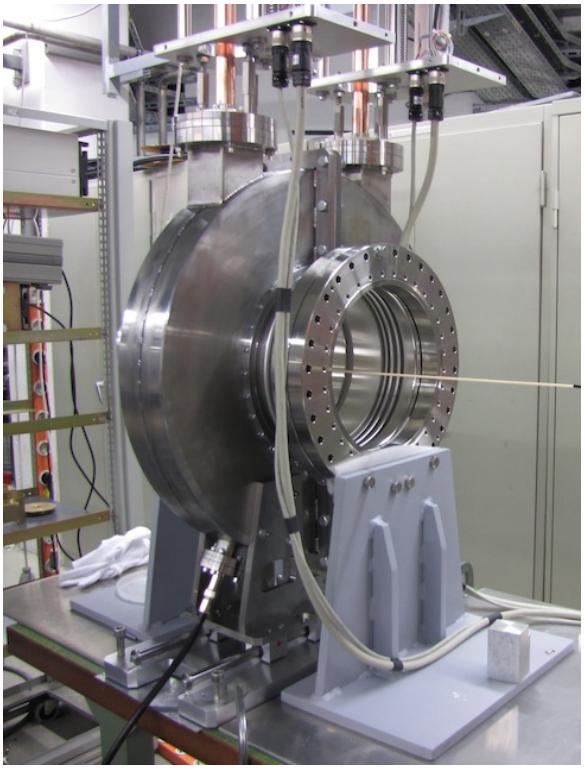

Figure 3.3: The pickup on a workbench before installation in the ESR ring. Photo: P. Petri

Motor-driven copper plungers can fine-tune the resonance frequency over a range of about 2 MHz. They feature limit switches that are calibrated. A linear potentiometer is used to measure position of plungers which can be controlled remotely by the GSI accelerator control system, with a software called **NODAL** from the main control room, where two commands are reserved for the position of each of the plungers (cf. section A.2.2). The plungers must be driven into the resonator only to change the inner volume. If they are inserted too far inside, they disturb the magnetic field too much and thereby change the mode geometry. The amplifier chain is connected to a magnetic loop antenna inside the resonator via a port with an N-type RF connector. Using semi rigid RF cable the signal is then carried to an RF shielded box that is installed directly under the resonator. The first element inside the RF shielded box, is a *low noise amplifier* LNA, followed by a band pass filter and a second amplifier. Outside of the box, there is another control board that contains two switches to turn on a third amplifier in the path. This board is connected with the box using **RG213** cable (approx.. 15 [m]). The board is then connected to the spectrum analyser in the main control room using a long (approx. 360 [m]) cable. Figure

3.4 shows the system overview with device numbers, noise figures, amplifier gains and cable attenuations. For a more detailed description of the control circuit please refer to section A.2.2. The overall gain and noise figure of the amplifier chain was calculated in example 2.2.3.

The analysis is done using a TEKTRONIX® **RSA3303B** real time spectrum analyser, featuring 14-bit ADCs. The center frequency of the analyser is tuned on top of the resonance curve of the resonator (around 244 MHz), where the harmonics of the particle induced signals are expected within 20 kHz of span. The spectrum analyser has an internal IQ demodulator and is capable of storing sampled data in frequency domain as well as in time domain. The time domain data are suitable for further off line signal processing on PC. The specific data format of the time domain files can be decoded using available routines for OCTAVE (or MATLAB™) [Jos10], [Tek08] or C++ [Nol10].

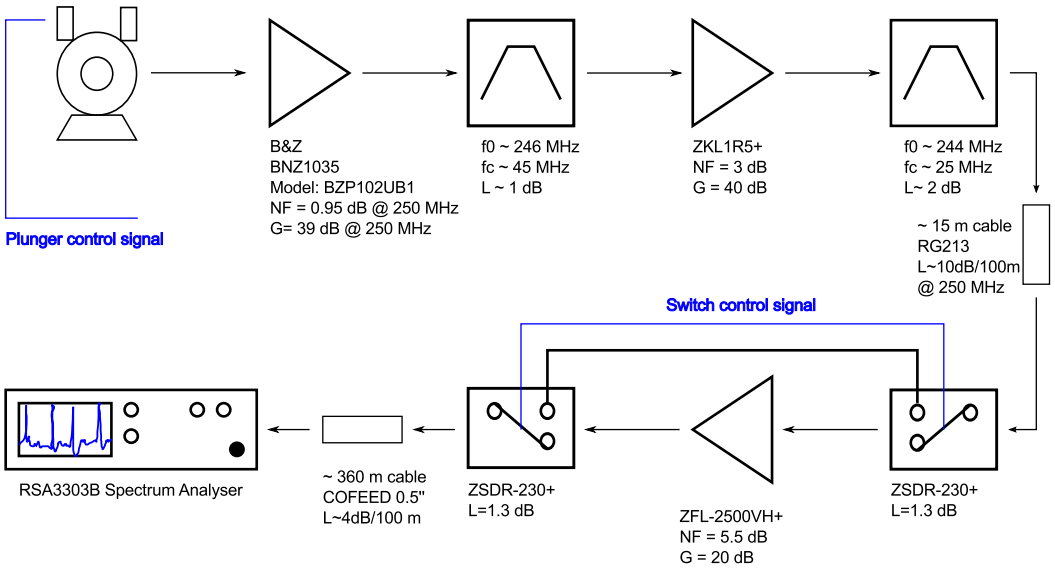

Figure 3.4: The signal flow diagram and the amplifier chain.

3.2. Numerical Simulations

Analytic solution allow observation of different parameters. Once the desired figures of merit are chosen for a design, numerical simulation techniques are used for fine tuning of final parameters. In the following section, the simulation results on the resonator is described. First we make a comparison between analytical and simulated characteristics

of a closed pillbox resonator with PEC walls. This comparison will first help establish an upper bound for the expected figures of merit, second it will demonstrate the reliability of the simulator. In the following part then, we go on to a more realistic model of the resonator where the effect of the beam pipe and ceramic gap are considered as well.

The resonator was designed to comply with the mechanical constraints imposed by the available gap/bellow structure and the beam pipe. After initial analytical calculations, simulation of the structure was needed to estimate the performance of the cavity. The dimensions for the simulation were chosen such that they mostly resemble the CAD data.

3.2.1 The pill-box

Analytical and simulated results are compared in table 3.2 for a closed pill box cavity with the same radius and depth as our design. In both models the material used is standard copper at room temperature. The magnitude of the electric fields is normalized to 10^6 $[V/m]$. It can be seen in the table that there is a good agreement between analytically calculated (see section 2.1) and simulation results with SUPERFISH.

3.2.2 The resonator

At first, qualitative simulations were carried out using CST-MAFIA-4 simulation package. Some of the results are depicted in figure 3.5. As expected from the fundamental mode, the cavity has a rotational magnetic field whereas the electric field is distributed in the pipe direction. In the pipe area the cavity is almost empty of magnetic fields and the electric field lines deviate from those of an ideal pill box in that they are bent due to the gap. The figure also shows high current densities around the interface between the pipe and the resonator. This is an important indication that the electrical connection between these two must be very good. High contact resistance causes higher dissipation, lower Q, detuned frequency and change in mode geometry.

A more detailed simulation for parameter extraction was performed using the SUPERFISH package. It makes use of the symmetrical characteristics of the pickup, considering only one fourth of the full structure in 2D cutting plane and closing the symmetry planes by ideal electric or magnetic boundary planes. Cylindrical symmetry is assumed in the simulation (see figure 3.6). Different symmetry plane configurations are explained in section A.2. SUPERFISH uses a triangular mesh. In order to account for the frequency change caused by the existing power coupler and stamp guides, a detune in the shape of contour change was

	Calculated Ideal Pillbox	Simulated Ideal Pillbox
f_0	382.47509 [MHz]	382.47485 [MHz]
Q	20310.3	20486.7
$\Lambda(0.71)$	0.836	0.957
$\widehat{R}_{sh}$	2.25 $[M\Omega]$	2.274 $[M\Omega]$
$\widehat{(R_{sh}/Q)}\Lambda(\beta)^2$	77.58 [Ω]	106.388 [Ω]
$\widehat{(R_{sh}/Q)}$	111.011 [Ω]	116.163 [Ω]
k	0.06669 $[V/pC]$	0.06116 $[V/pC]$
Stored Energy	30.362 [mJ]	30.354 [mJ]
Power loss	3.592 [kW]	3.560 [kW]

Table 3.2: Calculated and simulated results of an ideal pill box in SUPERFISH. Electric field is normalized to 1 [MV/m].

introduced, so that the resonance frequency corresponds to that of the measured structure. Following material characteristics were assumed for the simulation:

- Resonator made of 100% IACS[1] copper: 1.7241 $[\mu\Omega cm]$ @ 20°C (i.e. 5.8 $\times 10^7$ $[Siemens/m]$)
- Pipe and ceramic holder: Alloy Steel, X2CrNi19-11 (1.4306, 304L): 6.897×10^{-5} $[\Omega\ cm]$ @ 20°$C = 68.97$ $[\mu\Omega\ cm]$ (i.e. 1.45 $\times 10^6$ $[Siemens/m]$), $\mu_r = 1.3$
- 10mm between pipe and resonator: Cast (plain) steel: S235JO (1.0114, DIN: ST37-3U): 1.611e-5 $[\Omega\ cm]$ @ 20°$C = 16.11$ $[\mu\Omega\ cm]$ (i.e. 6.206 $\times 10^6$ $[Siemens/m]$), $\mu_r = 100$
- Ceramic gap: made of FRIALIT F 99,7 with $\varepsilon_r = 9.7 + j * 4.365 \times 10^{-3}$, i.e. tan $\delta = 4.5 \times 10^{-4}$

It is worth mentioning that the calculated shunt impedance in SUPERFISH is normalized to the length. The effect of transit time factor (TTF) is also considered in the simulation. Among many useful information, some important values that are extracted from the output of SUPERFISH post processor and their equivalent quantity mentioned in this work are listed in table 3.3. Since there is a symmetry plane at $z = 0$, values that are calculated for half of the structure must be multiplied by two. The value of $\widehat{R_{sh,1}/Q}$ which is interesting for comparison with bench top measurements must be calculated manually by dividing $\widehat{(R_{sh}/Q)}\Lambda(\beta)^2$ by $\Lambda(\beta)^2$. The results are summarized in Table 3.4 and the field patterns are depicted in figures 3.6 which shows a cut through the mid plane of the structure. The lines coloured in pink illustrate the equipotential electric field lines, brown arrows are

[1] International Annealed Copper Standard

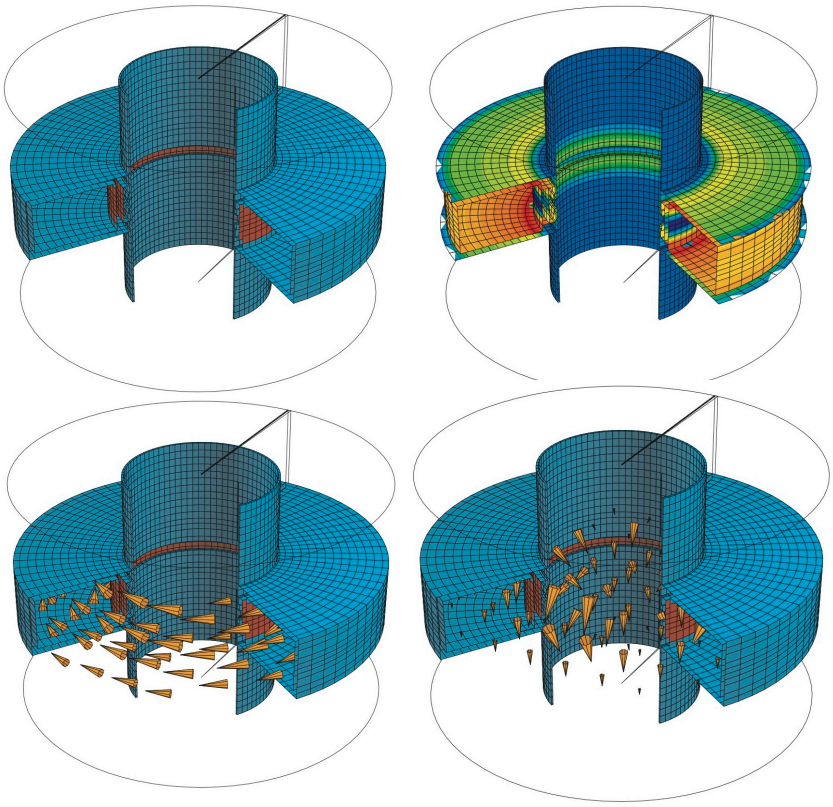

Figure 3.5: Resonator simulations with CST-MAFIA-4 showing the volume (top left), surface current (top right), magnetic field (bottom left) and electric fields (bottom right) of TM010 mode.

electric field components and the brown circles illustrate the magnetic field components perpendicular to the plane. Two different simulations were performed to check the effect of the ceramic gap. It is apparent from simulations that the dielectric losses due to the ceramic are significant. The results of the structure without the ceramic gap, which would resemble a fully evacuated cavity, is also listed in Table 3.4. From the table it can be seen that the fundamental frequency f_0 and characteristic impedance $\widehat{R_{sh}/Q}$ change mainly because the ceramic gap changes the geometry and volume inside of the resonator. The transit time factor $\Lambda(\beta)$ decreases and $(\widehat{R_{sh}/Q})\Lambda(\beta)^2$ and $\widehat{R}_{sh}$ respectively increase, since the magnitude of the electric field on the axis increases in the resonator without ceramic gap. Due to the same reason, the loss parameter k to the fundamental mode also increases, since the particle 'sees' a larger electric field on the axis. The stored energy is less in the resonator without ceramic, since in the resonator with ceramic gap, the electric displacement vector adds to the electric field intensity and the overall electric field density inside of the volume, which in turn increases the overall stored energy. The lossy dielectric accounts for huge

Nomenclature in this work	SUPERFISH SFO output	Unit	Comment
f_0	f_0	$[Hz]$	
Q	Q	$[-]$	for the whole structure
$\Lambda(\beta)$	T (Transit time factor)	$[-]$	for the specified β
$\widehat{R}_{sh}$	Shunt impedance	$[M\Omega/m]$	per unit length
$\widehat{R}_{sh}\Lambda(\beta)^2$	Z*T*T	$[M\Omega/m]$	per unit length
$\widehat{(R_{sh}/Q)}\Lambda(\beta)^2$	r/Q	$[\Omega]$	for half of the structure
$\widehat{R_{sh}/Q}$	N/A	$[\Omega]$	calculate manually
k	Wake loss parameter	$[V/pC]$	for half of the structure
W	Stored energy	$[J]$	for half of the structure
P_L	Power dissipation	$[W]$	for half of the structure

Table 3.3: SUPERFISH output parameters. N/A = not available

losses together with ohmic losses on the wall, compared to the case where only ohmic losses are present in the resonator without the ceramic gap. Figures 3.6 also show clearly

	With ceramic gap	Without ceramic gap	Unit
f_0	243.95	317.73	$[MHz]$
Q	**2550.32**	**5459.2**	$[-]$
$\Lambda(\beta)$	0.815	0.707	$[-]$
$\widehat{R}_{sh}$	0.137	0.445	$[M\Omega/m]$
$\widehat{(R_{sh}/Q)}\Lambda(\beta)^2$	35.602	40.832	$[\Omega]$
$\widehat{R_{sh}/Q}$	**53.54**	**81.73**	$[\Omega]$
k	0.01364	0.02038	$[V/pC]$
W	12.18	6.13	$[J]$
P_L	7.323	2.245	$[MW]$

Table 3.4: Simulated results on a more realistic model. Electric field is normalized to 1 $[MV/m]$.

that a significant electric field strength extends to fairly long distances within the beam pipe. This is due to the large beam pipe diameter of 250 [mm]. By comparing the stored energy in the resonator with beam pipe and the results of an ideal pill box (table 3.2) we see that a significant amount of energy is stored in this very field extension into the beam pipes. This extension affects power loss as well, since there is more ohmic wall exposed to the tangential magnetic field. The simulated electric field along the axis is plotted in figure 3.7, where the symmetry plane is located at the center of the cavity, i.e. $z = 0$.

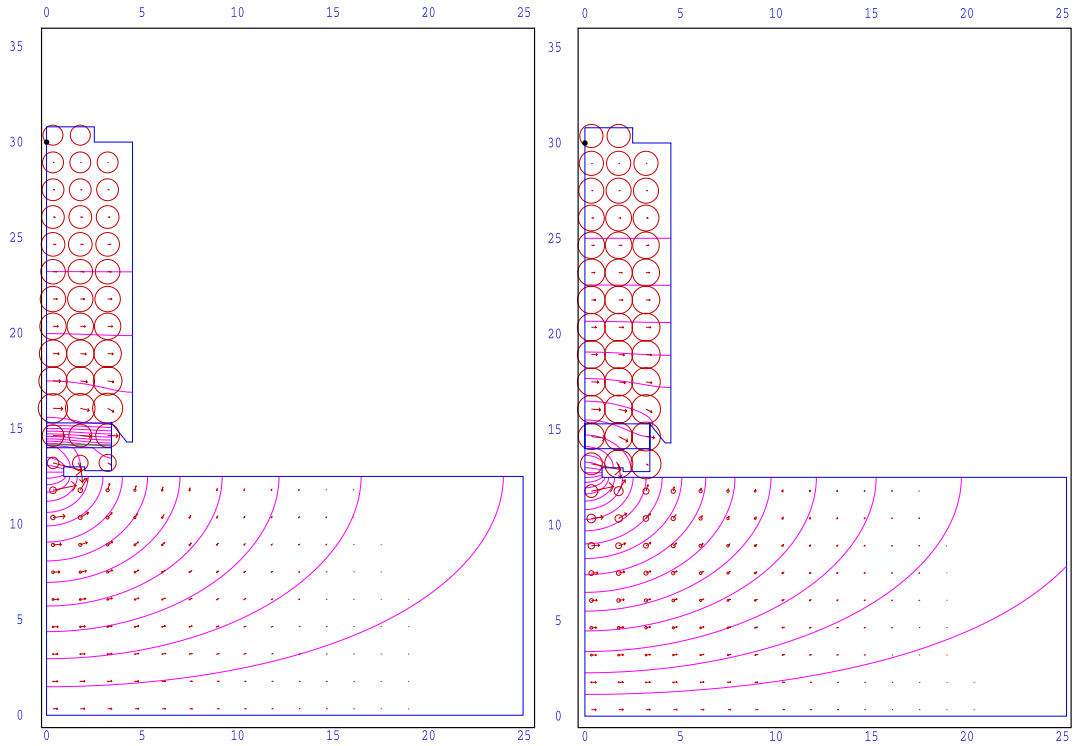

Figure 3.6: Resonator simulations with SUPERFISH showing the effect of the ceramic gap (left) compared to the structure without ceramic (right). Axes are in centimetres.

3.2.3 Transit time factor

Figure 3.7 also shows the simulated variation of the transit time factor Λ with the relativistic β. For a typical ion during our experiments (e.g. ^{142}Pm) with a kinetic energy of about 400 $[MeV/u]$, the relativistic β corresponds to about 0.71. According to the figure, this leads to a transit time factor Λ of about 0.7. Due to the non zero length of the cavity, the transit time factor never becomes unity even if particles would travel at the speed of light.

3.2.4 Higher order modes

Higher order modes are simulated using SUPERFISH. These values can be compared with the analytical modes in the ideal pill box (table 2.1), specially in the region below the cut-off frequency of the beam pipe. The relatively loose boundary conditions of the resonator with beam pipe causes the resonant modes to spread into higher frequency. The fundamental and the 14 higher order modes are listed in table 3.5. Unless the mode pattern

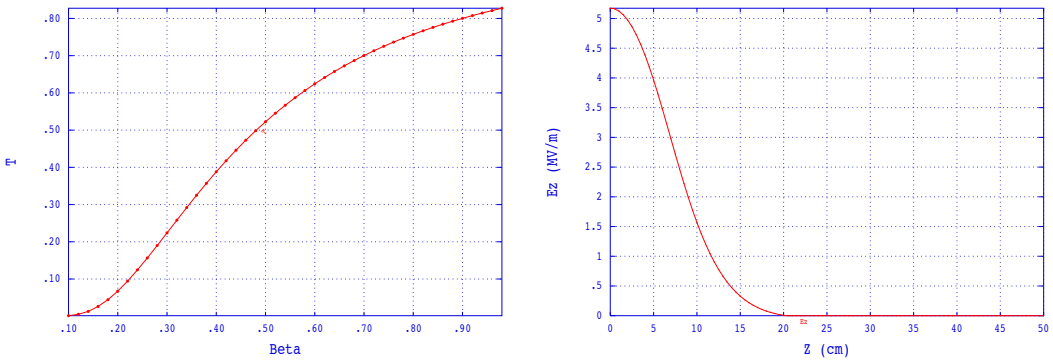

Figure 3.7: Simulated transit time factor vs. β (left). Simulated electric field distribution normalised to 1MV/m (right).

is not studied in each case, it is not possible to generally relate the mode names of the resonator with beam pipe to the mode names of the pill box. Nevertheless, the first four modes which are distinct can be identified. Using CST-MICROWAVE STUDIO®, frequencies

Mode	With ceramic gap	Without ceramic gap
1	240	310
2	410	470
3	900	900
4	910	920
5	930	940
6	960	970
7	1000	1010
8	1070	1080
9	1100	1130
10	1150	1170
11	1270	1300
12	1280	1310
13	1470	1740
14	1480	1760
15	1610	1810

Table 3.5: Simulated mode frequencies in SUPERFISH in units of $[MHz]$ for the cases with and without ceramic gap.

of fundamental and higher order modes were calculated with a model with similar details and materials as in the previous SUPERFISH calculations, with the the enhancement that another 5 $[mm]$ was added radially between the two half-cylinders to account for the losses that are caused by the faces that are connected by screws. The simulation was made using about 450000 hexahedral mesh cells for one eighth of the structure. This number is not

high enough to cover all details of the structure very well, but increasing the number of points would require better processing power and larger memory. So the results are only roughly comparable with the SUPERFISH results. Symmetry planes were used as described in section A.2.

Mode	Frequency $[MHz]$	Frequency Accuracy $[MHz]$	Q
1	**244.9**	0.005587	**2827.5**
2	328.1	3.764	3089.1
3	579.5	9.487e-005	1076
4	905.7	0.2116	5760
5	951.4	0.03627	1278.1
6	976.5	0.04658	5908
7	1078.	0.03233	7318
8	1256.	0.1125	1656.8
9	1298.	0.9488	3468.6
10	1354.	0.3075	5160.9
11	1564.	0.08215	3925.5
12	1745.	0.2609	2117.8
13	1943.	0.1110	1820.4
14	2031.	0.8137	4002
15	2104.	0.2689	4258.2

Table 3.6: Simulated mode frequencies in CST-MICROWAVE STUDIO.

3.3. Benchtop Measurements

For the bench measurements a vector network analyser (VNA) was used. The VNA must be calibrated with the calibration kit in single port configuration for the reflection coefficient. For the transmission measurement, a 'through' calibration is enough. For the resonant measurement a very useful feature is the *marker tracking* function which can be set to track the resonance frequency. For a non-resonant measurement marker tracking should be turned off.

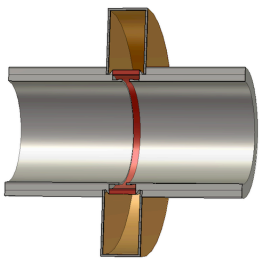

Figure 3.8: Detailed model in CST MICROWAVE STUDIO®.

3.3.1 Q value and coupling factor κ

First the size of the magnetic loop was trimmed manually to account for sufficient coupling. Fine tuning of the value of $\kappa = 1$ *for the fundamental mode* was achieved by slightly turning the loop so that the effective surface is reduced. Q value measurement followed the instructions in [Cas10]. The IMP resonator was measured once in 2010 at GSI Darmstadt and once in 2011 after shipping to China before installation into the CSRe ring at IMP. Measurements are done using an **Agilent 8753ES** network analyser. For the 2011 measurement of the IMP resonator a VNA of type **Agilent E5071C** was used at 0 dBm power. The measurement results are summarized in table 3.7. Note that the position of the plungers changes the resonant frequency about 2 MHz.

Date	Resonator	$f_0[MHz]$	Mode	Q	κ
2010	GSI	243.986250	first	1130	≈ 1
2010	GSI	≈ 375	second	N/M	N/M
2010	IMP	243.9272	first	1072	≈ 1
2011	IMP	242.36585	first	1003	0.97
2011	IMP	370.44681	second	980	0.7

Table 3.7: Results of measurements of f_0, Q and κ. N/M = not measured.

3.3.2 Determination of $\widehat{R_{sh,1}/Q}$ using cavity perturbation

Analytical methods for simple cavity structures and numerical methods for more realistic real life applications help reach limits for a final design. After the construction though, there is always a need to actually measure the device and to see how much it complies with predictions. Some cavity parameters can be determined using bench top measurements. Accurate measurements of the characteristic impedance of the resonator is practically very difficult due to its extremely large beam pipe openings. Nevertheless, with a careful set-up, a rough estimate is possible. Determination of $\widehat{R_{sh,v}/Q}$ is based on the theory of perturbation of cavities which will be covered in this section. Different measurement methods can be applied and they result in different values. Altogether a general trend can be observed.

Measurement of RF cavity properties using perturbation method was first introduced by J. Müller [Mue39] in 1939 and later in his comprehensive work by J. C. Slater [Sla46] and [MJS52]. Ever since there has been many publications and enhancements on the topic.

The main idea is to connect a generator and an analyser to the cavity and measure how much of the generator power is reflected or transmitted by the resonator before and after perturbation. In practice the so called *s-parametes* are used[2]. The perturbation is assumed to be very small and can be in the form of a change in the boundary walls of the resonator or a small object put any where inside it.

Usually one differentiates between the resonant and non-resonant perturbation. In the resonant perturbation, the instrument is tuned to the resonant frequency of the cavity both before and after the perturbation. The difference between these two values is taken into consideration. In the non resonant approach, the instrument is tuned only to the resonant frequency before perturbation, then the phase of the reflection coefficient is measured before and after the perturbation. The non resonant method is not covered in this work, but can be found in detail in [Ste66], [Hue92] and [Hue01].

Different perturbing objects may be 'sensitive' electric or magnetic fields or both. Metallic objects are sensitive to both electric and magnetic fields whereas dielectric objects are mainly sensitive to the electric field only. The shape of the perturbing object may also be used to selectively perturb longitudinal (a needle) or transversal field components (a disc shape) [Pes95]. In this work we consider the resonant method and use it in the fundamental mode, since the resonant pick up is designed to work in this mode. The underlying theorem that enables these measurements is the BOLTZMANN-EHRENFEST Theorem ([Wan08] page 165) which relates the change of the resonance frequency to a change in stored energy in a cavity

$$\frac{\Delta\omega}{\omega_0} = \frac{\Delta W}{W} \tag{3.3.1}$$

Resonant capacitor method

Capacitor perturbation methods are often used in RFQ design. For a cavity structure it may deliver results that are not so accurate since the capacitor itself reduces the volume inside of the cavity and thereby changes the mode geometry. Nevertheless a small capacitor can be connected in parallel to the gap in order to infinitesimally

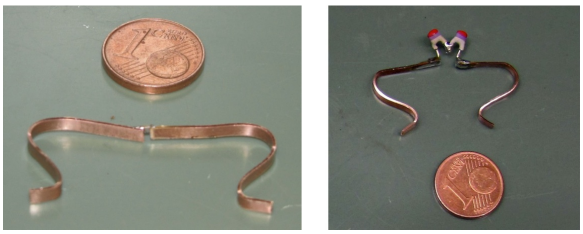

Figure 3.9: Capacitors for perturbation measurement soldered in the middle of copper holders.

[2]Detailed description cab be found in [Col00]

perturb its value. The resonance frequency
depends only on the gap inductance L_1 and gap capacitance C_1 in the fundamental mode. A change in the resonance frequency can be related to the characteristic impedance using equation 3.3.1. For this purpose, equation A.1.84 can be expanded using a TAYLOR series for small variations about C_1. Since parallel capacitances add up, we have a change in total capacitance $(C_1 + \delta C) - C_1 = \delta C$. So we have

$$\frac{\delta f_{0,1}}{f_{0,1}} = -\frac{1}{2}\frac{\delta C}{C_1} \tag{3.3.2}$$

Combining equations 2.1.38 and A.1.94b we have

$$Q = \pi f_{0,1} \widehat{R_{sh}} C_1 \tag{3.3.3}$$

This leads to the final relation:

$$\widehat{\left(\frac{R_{sh,1}}{Q}\right)} = -\frac{2}{\pi}\frac{\delta f_{0,1}}{f_{0,1}^2}\frac{1}{\delta C} \tag{3.3.4}$$

For an added parallel capacitance, the quantity $\delta f_{0,1}$ will always be negative, so that the negative sign of the expression vanishes. The used capacitors (see figure 3.9) were of 5% precision and 20% type and were tested with a VNA (soldered inside of a 50 Ω N-Type female connector) on the resonant frequency to check if they have the nominal value. Same capacitor values in series result in half capacitance, but precision remains the same. During the measurement the resonance frequency was $f_{0,1} = 243.95\ [MHz] \pm 1000\ [Hz]$. Error propagation is calculated using equation 3.3.10. Table 3.8 shows the results. The results

Capacitor $[pF]$ ±20%	Δf $[MHz]$ ±100$[Hz]$	Capacitor $[pF]$ ±5%	Δf $[kHz]$ ±100$[Hz]$
2.2	13.1	2.2	2.6
2.0	11.3	2.0	2.45
1.0	5.19	1.0	3.05
0.5	2.65	0.5	1.85
$\widehat{R_{sh,1}/Q} = 59 \pm 3\ [\Omega]$		$\widehat{R_{sh,1}/Q} = 16 \pm 7\ [\Omega]$	

Table 3.8: Results of measurement of $\widehat{R_{sh,1}/Q}$ of the GSI resonator with capacitor method.

of the 20% caps are more comparable to other methods. One possible reason can be the better electrical contacts of their wired ports (figure 3.9 right). Still due to their larger size, they may actually shift the frequency more than what the added capacitance would

do, so the resulting characteristic impedance is overestimated. Another source of error is the large value of the perturbation capacitors ranging from 0.5 to 2.2 [pF] compared to the calculated value of the gap capacitance C_0 of about 97 [pF] (cf. example 2.1.2). Nevertheless the results are relatively acceptable.

Resonant dielectric rod method

The method described here is for measuring $\widehat{R_{sh,1}/Q}$ in the fundamental TM010 mode of the resonator. A similar approach has been presented in [Car01]. A completely different approach which we did not employ here uses a conductive wire. It has been described in many papers including [CD85].

The perturbation is carried out by using a dielectric (ceramic) rod with a diameter that is small compared to the diameter of the cavity. The resonance frequency of the cavity is measured first. Then while keeping other settings fixed, the rod is placed on the symmetry axis of the cavity as in figure 3.3 and the resonance frequency is measured again. There are practically no magnetic field components on the axis of the cavity, so the electric field component delivers the result. Due to the perturbation, the resonance frequency will change to smaller values. The change is then proportional to the value of $\widehat{R_{sh,1}/Q}$ in the following way. We start with the stored energy in the electric field inside a thin confined cylindrical volume of a rod on the axis of the resonator. Keeping in mind that the tangential electric field component is continuous on the border between rod and vacuum as stated in equation A.1.23a we have from equation 2.1.3.

$$W_e = \frac{1}{4}\varepsilon_0\varepsilon_r \int_V |E_z|^2 \, dV \tag{3.3.5}$$

The depending on whether the cylinder is filled with dielectric material (ceramic) or is empty, a difference in stored energy can be calculated[3].

$$\begin{aligned} \Delta W &= \Delta W_{e,cer} - \Delta W_{e,vacuum} \\ &= \frac{1}{4}\varepsilon_0 |E_z|^2 V_{rod}(\varepsilon_r - 1) \end{aligned} \tag{3.3.6}$$

where $V_{rod} = 2\pi\varrho_{rod}^2 l_{rod}$ is the volume of the rod in the region where the electric field is extended. For a pill box this region is completely enclosed within the cavity, but for a

[3] ΔW will be positive.

pillbox with attached pipes, this region extends more into the pipes the larger the diameter of beam pipes are. The value of the extension of the electric field must be determined experimentally by carefully inserting an object from both sides along the axis and monitoring the vector network analyser to see when it shows a considerable change in the reflection (or transmission) coefficient. Further, by applying equations A.1.87 and 2.1.31 and then applying equations 2.1.21, 3.3.1 and 3.3.6 we have

$$\begin{aligned}
\widehat{\left(\frac{R_{sh,1}}{Q}\right)} &= \frac{\hat{U}^2}{\omega_0 W} \\
&= \frac{\hat{U}^2 \Delta\omega}{\omega_0^2 \Delta W} \\
&= \frac{|E_z|^2 l_{rod}^2 \Delta\omega}{\omega_0^2 \Delta W} \\
&= \frac{4|E_z|^2 l_{rod}^2 \Delta\omega}{\omega_0^2 \varepsilon_0 |E_z|^2 V_{rod}(\varepsilon_r - 1)} \\
&= \frac{2}{\pi} \frac{l_{rod}^2}{V_{rod}} \frac{1}{\varepsilon_0(\varepsilon_r - 1)} \frac{\Delta f}{f_0^2} \\
&\quad or \\
&= \frac{2}{\pi^2} \frac{l_{rod}}{\varrho_{rod}^2} \frac{1}{\varepsilon_0(\varepsilon_r - 1)} \frac{\Delta f}{f_0^2}
\end{aligned} \tag{3.3.7}$$

There are two different ways equation 3.3.7 can be used in a measurement:

- Retrieve the relative permittivity of the ceramic material from the datasheets provided by the manufacturer (Direct rod method).
- Calibrate the rod to encapsulate all rod specific features into a single constant (Calibrated rod method).

For the second method, a constant α is defined so that is contains all characteristics of the rod.

$$\widehat{\left(\frac{R_{sh,1}}{Q}\right)} = \alpha \frac{d}{\varrho_{rod}^2} \frac{\Delta f}{f_0^2} \tag{3.3.8}$$

with

$$\alpha = \frac{2}{\pi^2} \frac{1}{\varepsilon_0(\varepsilon_r - 1)} \tag{3.3.9}$$

in units of $[\Omega\ m/s]$. This constant must then be determined in another resonator with depth d with known characteristics. Such a *calibration resonator* has usually a simple shape and no beam pipes so that its figures of merit highly match their predicted analytical

values. These resonators are usually used at universities for educational purposes. For these resonators one can assume that $\widehat{(R_{sh,1}/Q)}_{ideal} = \widehat{(R_{sh,1}/Q)}_{measured}$ since the characteristic impedance is only a function of geometry. With this assumption, the dielectric rod can be calibrated using equation 3.3.8 and subsequently used for the measurement using equation 3.3.7. Finally the usual error analysis can be applied. The propagation of error into a function $f(x)$ can be obtained using

$$df = \sqrt{\sum_{i=1}^{N} \left(\frac{\partial f}{\partial x_i}\right)^2 dx_i^2} \tag{3.3.10}$$

where N is the number of quantities with uncertainty, and dx_i is the uncertainty of each. The average of many of such quantities from different measurements can be made using:

$$\langle x \rangle = \frac{\sum_{i=1}^{N} \frac{x_i}{\sigma_i^2}}{\sum_{i=1}^{N} \frac{1}{\sigma_i^2}} \tag{3.3.11}$$

with the corresponding error

$$\sigma = \sqrt{\frac{\sum_{i=1}^{N} \frac{(x_i - \langle x \rangle)^2}{\sigma_i^2}}{\sum_{i=1}^{N} \frac{1}{\sigma_i^2}}} \tag{3.3.12}$$

For the resonant rod measurement a ceramic rod made of DEGUSSIT-AL23 (made by Friatec AG, Germany, same material as FRIALIT F99,7 which was also used as gap material but different commercial name) was used. Since the measurement was completely static, loss tangent was ignored.

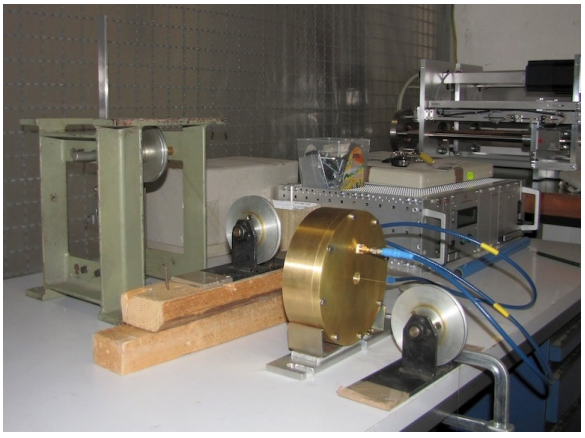

Figure 3.10: The calibration resonator on the test bench.

For the direct method, a value of $\varepsilon_r = 9.7$ from the technical data-sheets [Web10] was used in equation 3.3.7. An error of ± 0.4 was considered. Calculations were done using an effective length $l_{rod} =$

19 $[cm]$ with a relatively large error of $\pm 1.5[cm]$. This effective length was measured as described in the theory section using the rod itself, by slowly inserting it on the axis from both sides to see where a significant change in the electric field is visible. This length is of course smaller than the total length 'seen' by the metallic bead in figure 3.11 because of the difference in material. Nevertheless, the choice of this effective length doesn't affect the change in frequency since the rods were anyway much longer than the whole structure. Other error sources are written in the table and error propagation is calculated using equation 3.3.10. Using equations 3.3.11 and 3.3.12, the final result of the direct rod method

Date	Resonator	f_0 $[MHz]$ $\pm 100[Hz]$	$2 \times \varrho_{rod}$ $[mm]$ $\pm 0.1[mm]$	Δf $[kHz]$ $\pm 10[Hz]$	$\widehat{R_{sh,1}/Q}$ $[\Omega]$ (Direct)	$\widehat{R_{sh,1}/Q}$ $[\Omega]$ (Calibrated)
2010	GSI	243.986250	3	9.75	36.4 ± 5.9	49.2 ± 9.3
2010	GSI	243.986250	5	26	35 ± 4.3	131 ± 25
2010	IMP	244.2841	0.5	0.375	50.2 ± 40.5	1.89 ± 0.36
2010	IMP	244.2841	1.1	1.437	39.8 ± 14.9	7.2 ± 1.4
2010	IMP	244.2841	2.5	5	26.8 ± 4.9	25.2 ± 4.8

Table 3.9: Results of measurement of $\widehat{R_{sh,1}/Q}$ with rod method. D is the DEGUSSIT rod

for the GSI resonator is shown in table 3.9.

Calibrated rod method was used with DEGUSSIT rod and was performed using a cylindrical calibration resonator almost in the shape of a pillbox made of **MS-58** brass (see figure 3.10) with radius $\varrho = 70 \pm 1$ $[mm]$ and depth $d = 32 \pm 1$ $[mm]$. It had an extremely small coupling loop and a front antenna for the electric field coupling both with low coupling factor so that transmission measurements could be performed with higher accuracy.

While the theoretical and measured fundamental frequencies match perfectly ($f_{0,analytic} = 1.639178969 \times 10^9$ $[Hz]$ and $f_{0,measured} = 1.641212769 \times 10^9$ $[Hz]$), a comparison shows that the measured Q value is **78 %** of the theoretical Q factor for the specified geometry ($Q_{analytic} = 6609.743257$, $Q_{simulated} = 6607.9$[4] and $Q_{measured} = 5138$). The difference can be related to the openings on the wall and other irregularities. Nevertheless, since the characteristic impedance ($\widehat{R_{sh,1}/Q}$) (169.2 $[\Omega]$ analytic and 170.3 $[\Omega]$ simulated) only depends on the geometrical design we can use equation 3.3.8 to determine the rod constant. The error in mechanical dimensions were considered ± 1 $[mm]$ which causes an error of ± 5.8 $[\Omega]$ when used in equation 3.3.10. Using a rod with 1.5 $[mm]$ in diameter we get a

[4]Using $\sigma_{brass} = 1.4 \times 10^7$ $[S/m]$ which leads to resistivity 7.14285×10^{-6} $[\Omega\ cm]$

normalized constant $\alpha = 8.9 \times 10^8 \pm 2.4 \times 10^8$ $[\Omega\ m/s]$ where

$$\alpha = \widehat{\left(\frac{R_{sh,1}}{Q}\right)} \frac{f_0^2}{\Delta f} \tag{3.3.13}$$

Using equations 3.3.11 and 3.3.11, the final result of the calibrated rod method for the GSI resonator is 59.15 ± 26.8 $[\Omega]$ and for the IMP resonator 2.33 ± 2 $[\Omega]$. These results are also shown in table 3.9. More realistic results are achieved using the direct rod method. The calibrated rod method works well, when using a proper diameter size in the time of calibration. It will either overestimate the characteristic impedance for the 5 [mm] rod or underestimate it for thin rods.

Resonant bead pull method

The rod method has an integrating effect and is not sensitive to variations of electric field distribution along the axis. To account for that, a bead (small piece) of dielectric or metallic material can be used. The bead is moved step wise along the axis such that the shift of the resonant frequency can be recorded. The overall measurement leads to the normalized distribution of the electric field and the value of $\widehat{R_{sh,1}/Q}$.

In the literature, the bead is usually approximated as an ellipsoid of revolution and is described using a confocal coordinate system [MJS52]. SLATER derived an expression for the perturbation of boundaries [Sla46][5]

$$\frac{\omega_0^2 - \omega_{0p}^2}{\omega_{0p}^2} = \frac{\int_V \vec{E}^* \vec{P}\, dV - \int_V \vec{H}^* \vec{M}\, dV}{2W} \tag{3.3.14}$$

where ω_{0p} is the resonance frequency after the insertion of the perturbing object. $\vec{P}$ is the polarization and $\vec{M}$ is the magnetization caused by the bead. The volume integrals must in principle be calculated over the whole cavity volume, but since these two quantities are non zero only inside the perturbing object, the volume integrals can be calculated over the object's volume only. In the fundamental mode there are no components of the magnetic field on the axis[6], so the second integral vanishes. On the axis in the fundamental mode $\vec{E}$ has only a z component E_z. W is the stored energy in the cavity in the mode in question,

[5] More detailed explanation in [Hue92] and [Pes95] (German).
[6] For a pure dielectric material the magnetization is zero

in this case the fundamental mode. For a comparatively thin bead, the polarization vector has only one component along the z axis $\vec{P} = P_z \vec{e_z}$.

In the following discussion, the indexes $1, 2, 3$ and a, b, c correspond to the three coordinate directions x, y and z, whereas a, b and c are the two semi minor and one semi major axis of the ellipsoid. In a rotationally symmetric ellipsoid we have $a = b$. In the literature mentioned above, it is shown that the electric field inside of the ellipsoidal bead can be determined using

$$\vec{E}_b = \mathring{A}\vec{E} \tag{3.3.15}$$

where $\mathring{A}$ is a diagonal matrix. On the z axis, we are interested in the matrix element A_{33} which is

$$A_{33} = \frac{1}{1 + \dfrac{(\varepsilon_r - \varepsilon_0)L_C}{\varepsilon_0}} \tag{3.3.16}$$

with

$$L_C = \frac{1}{2}abc \int_0^\infty \frac{1}{(s+c^2)\sqrt{(s+a^2)(s+b^2)(s+c^2)}}\, ds \tag{3.3.17}$$

which is an elliptical integral[7]. The expression for polarization is:

$$\begin{aligned} P_z =& (\varepsilon_r - \varepsilon_0) A_{33} E_z \\ =& \frac{\left(\varepsilon_r - \varepsilon_0\right) E_z}{1 + \dfrac{\left(\varepsilon_r - \varepsilon_0\right) L_C}{\varepsilon_0}} \end{aligned} \tag{3.3.18}$$

For a metallic bead with infinite relative permittivity we have

$$\lim_{\varepsilon_r \to \infty} P_z = \frac{\varepsilon_0 E_z}{L_C} \tag{3.3.19}$$

Evaluating the integral over the bead volume V_b in equation 3.3.14 we get

$$\frac{\omega_0^2 - \omega_{0p}^2}{\omega_{0p}^2} = \frac{1}{2}\frac{\varepsilon_0 |E_z|^2 V_b}{L_C W} \tag{3.3.20}$$

From equation A.1.87 we have $W = QP_L/\omega_0$. Substituting we have

$$\frac{|E_z|^2}{QP_L} = 2\frac{\left({\omega_0}^2 - {\omega_{0p}}^2\right) L_C}{{\omega_{0p}}^2 \varepsilon_0 V_b \omega_0} \tag{3.3.21}$$

[7] A similar expression exists for elliptical integrals L_a and L_b along x and y axis [Pes95].

From equation 2.1.31 we know that $\widehat{R_{sh,v}} = \hat{U}/P_L$. Dividing both sides by Q and using equation 2.1.21 and the square root of the right hand side of equation 3.3.21 we have:

$$\begin{aligned}
\widehat{\left(\frac{R_{sh,1}}{Q}\right)} &= \frac{\left(\int_{-d/2}^{d/2} E_z\, dz\right)^2}{QP_L} \\
&= \left(\int_{-d/2}^{d/2} \frac{|E_z|}{\sqrt{QP_L}}\, dz\right)^2 \\
&= \left(\int_{-d/2}^{d/2} \sqrt{\frac{2\left({\omega_0}^2 - {\omega_{0p}}^2\right) L_C}{{\omega_{0p}}^2 \varepsilon_0 V_b \omega_0}}\, dz\right)^2 \\
&= \left(\int_{-d/2}^{d/2} \sqrt{M\frac{(f_0^2 - f^2)}{f^2}}\, dz\right)^2
\end{aligned} \tag{3.3.22}$$

where $M = L_C/(\pi\varepsilon_0 f_0 V_b)$ is a constant that depends only on the geometrical factors of the bead. The quantity $|E_z|/\sqrt{QP_L}$ in equation 3.3.22 shows the normalized electric field strength at each position along the axis in units of $[\Omega/m]$. This quantity is achieved by keeping the constant M inside of the square root. Equation 3.3.22 can finally be used for the bead pull measurement.

Bead pull measurement was performed at IMP in August 2011. It was carried out in fundamental mode at 242.38389 $[MHz]$. For better measurement results, dummy copper pipes were attached to both sides of the resonator. For the bead pull system, a step motor controller **Zolix MC200** was used. The controller was set to no acceleration between points, relative speed of 100 and single step trigger for 148 measurement points each 1 cm apart. An **Agilent E5071C** VNA was calibrated in reflection mode with the N type calkit **85032F**. A low loss high frequency cable with SMA connectors was connected to the N type port. The bead or in this case the needle was a 14 mm long hollow cylinder with an outer diameter of 4 mm and inner diameter of 2 mm. In order to use equation 3.3.22, the needle was assumed to be an equivalent ellipsoid of revolution with the *same outer diameter and volume*, i.e. $a = b = 2\ mm$ and $c = 10.5\ mm$. It was glued to a thin nylon string which was stretched through the center of the resonator. The stretched thread will always have some small misalignments. This causes an overall linear trend in the data. The effect of misalignment must be corrected from the data. Finally the data was cut on both sides

where the values were almost zero.

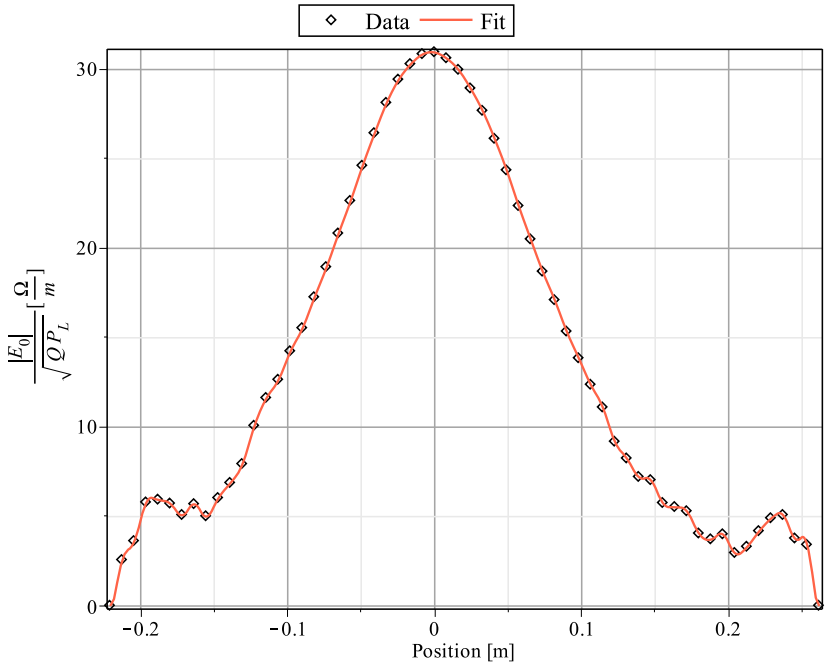

Figure 3.11: Normalized electric field amplitude of the fundamental mode on axis of the IMP resonator, measured data and fit.

The normalized electric field at each position is plotted in figure 3.11. Each of the measured data points, which are shown in black, are averaged results of 10 measurements. The plot is centred at the resonator center, same as the origin used in the simulation models (cf. figure 3.7). The bellows structure is to the right side of the graph. It can be seen from the figure, that the electric field has a larger extension into the beam pipe on the side with the bellows structure. The resulting $\widehat{R_{sh,1}/Q}$ is about 42 [Ω]. Using the measured $Q = 1003$ we have $\widehat{R_{sh,1}} = 42.3$ [$k\Omega$].

The above result should be considered as a mean value. The used setup doesn't allow proper estimation of the error for the given value of 42 Ohms. Here a short description of the situation: These data have actually a vertical and a horizontal error bar. The vertical error is caused by the uncertainties in mechanical dimensions from equation 3.3.17 that propagate into the constant M in equation 3.3.22 and the frequency uncertainties in equation 3.3.22 itself which are about ±1 [kHz]. The horizontal uncertainty is caused by the slipping of the thread: the step motor controller is connected to pulleys, the thread actually slips tiny amounts on each stepper motor step, so that the displayed value is not equal the total length of the structure any more, i.e. 148 [cm] instead of 121 [cm]. It is even not sure if in every step, the thread slipped the same amount, so that completely different

horizontal errorbars for every points may be expected. The last contributing factor to error is the coupling between the horizontal and vertical errorbars, since for every misplaced position, there would have been a different measured frequency other than recorded. As a simplification, the mean value for every data point was equally distributed, i.e. the data points were shrunken horizontally accordingly. All of these effects, change the area under the curve in equation 3.3.22 so that a maximum and a minimum characteristic impedance around the given value result. A suggestion is provided in the outlook section 5.2 for more accurate measurements in the future.

Using beam power

Using equation 2.2.25 one can actually determine the characteristic impedance experimentally by measuring the beam power. This method delivers very approximate results because of many uncertainties that may be caused due to the transmission circuits. Nevertheless, the values provided in table 2.2 and figure 4.5 on page 83 show that the values of characteristic impedance determined by other methods is in the correct order.

3.3.3 Other measurements

Background noise

Spectroscopy was performed on the input of the amplifier chain to determine the noise behaviour using an **Agilent 4395A**. Figure 3.12 shows the noise in the measurement setup where the input is terminated by a short, a load or by the resonator. Typical standing wave patterns are visible. The resonant frequency is also visible together with a peak on the next higher order mode (TM110). Figure 3.12 also shows a close up around the resonant frequency, where some other fluctuation is also visible. One of the practical issues in such measurements concerns the input attenuation of the spectrum analyser. One usually sets the input attenuation (or uses the auto attenuation) such that there is minimum distortion of the signal due to the spectrum analyser itself (compression point). The reference level is chosen so that there is at least 20 $[dB]$ difference between noise floor of the spectrum analyser without signal and noise floor after the amplifier chain. Other components in the storage ring also contribute to the overall noise background. Some thermal energy travels through the whole ring and settles on an equilibrium.

Radiation losses

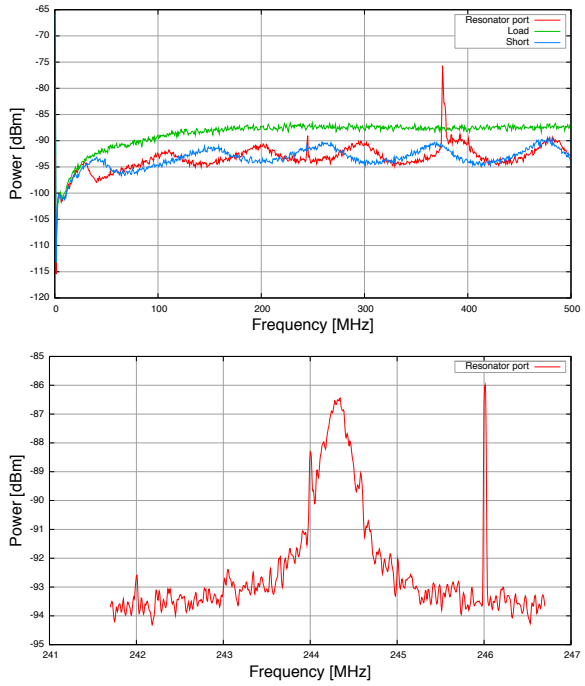

Figure 3.12: Noise floor on the amplifier chain for $RBW = 1\,[MHz]$ and span = 500 MHz (left). Noise background close-up around the resonant frequency for $RBW = 30\,[kHz]$ and span = 5 MHz (right).

As it always is, real life constructions are anything but ideal and perfect. Much of the deviations of the measured Q value and the theoretical (simulated) is due to losses through the mechanical joints into the surrounding. A tuned antenna was built to measure radiation using a VNA (in transmission) for the GSI and IMP resonator. Although proper RF shielding was taken into consideration of design, radiation was visible mostly in the region of the ports and connections between the beam pipe. It is hoped that in future designs, fully evacuated cavities eliminate the needs for RF shielding between the mechanical parts.

Higher order modes

Apart from the fundamental mode, higher order modes below the pipe cut-off frequency are also excited. The band pass filter in figure 3.4 suppresses their contribution to the final signal, but still a considerable amount passes through. Their position is easily visible when high beam currents are stored in ESR. Figure 3.13 shows the fundamental mode at 244.95 $[MHz]$ and higher order modes at 375.2 $[MHz]$, 489.7 $[MHz]$ and 734.5 $[MHz]$ in an experiment performed in 2012 using an approx. 4 mA hydrogen-like ^{197}Au beam. Unfortunately simulation results of higher order modes in tables 3.5 and 3.6 were not accurate enough to predict these frequencies.

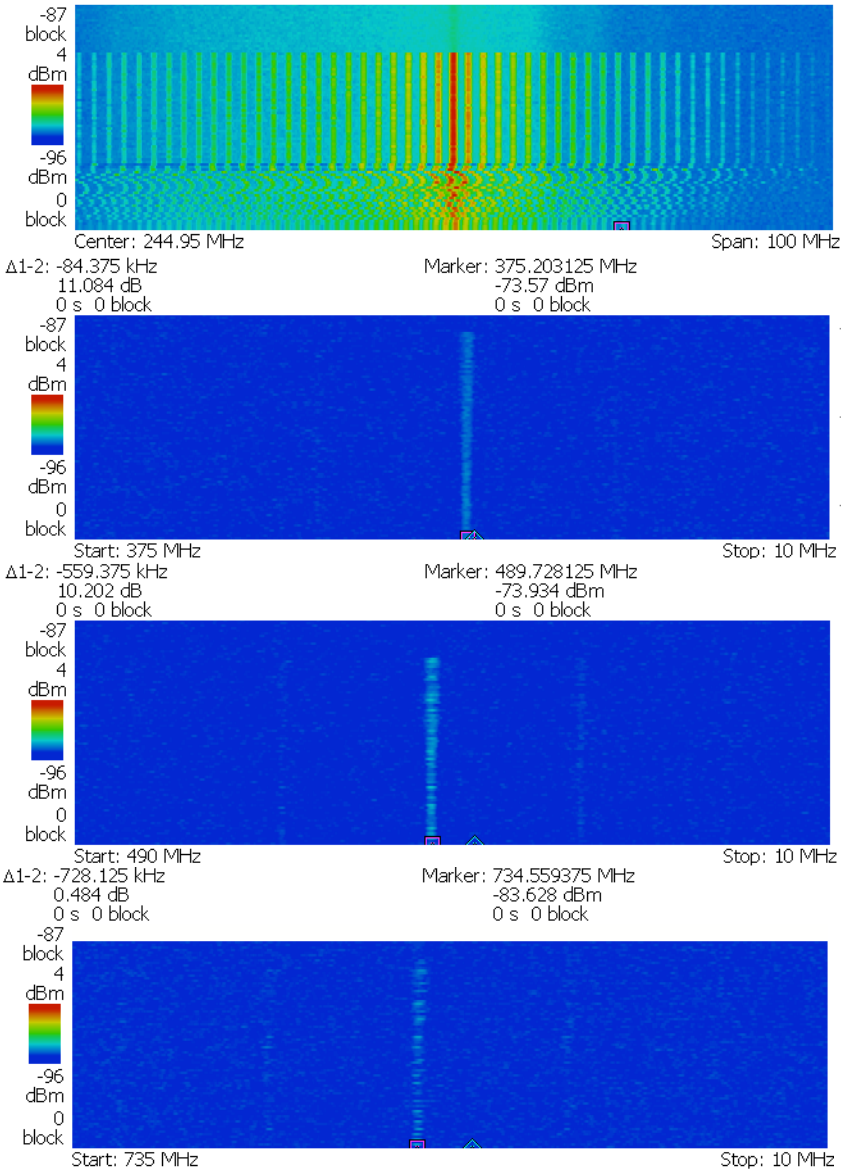

Figure 3.13: Schottky lines in fundamental and the first 3 higher order modes of an approx. 4 *mA* hydrogen-like ^{197}Au beam.

CHAPTER 4

FEATURES AND APPLICATION OF THE PICKUP IN STORAGE RING EXPERIMENTS

The following chapter is dedicated to the features and applications of the resonant pickup in storage ring physics.

4.1. Features of the Resonant Pickup

The underlying central property of the resonant pickup that makes it an indespensible tool for storage ring physics can be summarised in one sentence: The resonant pickup has a high sensitivity when measuring higher harmonic of the SCHOTTKY signals. To see how this actually helps we need to consider the following points:

Resolution and speed

If two particles or two isomeric states of the same nuclide have nearly equal masses, they will appear as two very close frequency lines in the spectrum. In order to resolve them, one might choose either of the two alternatives[1]

- Use a long enough acquisition time at a lower harmonic
- Use a mixed down version of higher harmonics for a given acquisition time

[1] Obviously, if the lines are exactly on top of each other, it is impossible to resolve them at all.

The explanation follows: Longer acquisition times means that a larger time domain window is needed in order to resolve two frequency peaks. According to the FOURIER analysis the FOURIER transform of a rectangular time window corresponds to a sinc function as it can be seen in the equation A.1.129 and figure A.9 in the appendix. The two frequencies of interest f_1 and f_2 must lie within the main lobe of the sinc function, so considering equation A.1.130 the time window must *at least* be

$$T_{min} = 2/(f_2 - f_1) = 2/\Delta f \tag{4.1.1}$$

If we are concerned with masses of short lived nuclei, then we are dealing with a fixed maximum acquisition time so that we are forced to choose other alternatives, such as the second method. From SCHOTTKY theory (cf. section 2.2) we know that:

1. Harmonic frequencies are placed at multiples of the revolution frequency f_r.
2. SCHOTTKY bands widen, i.e. SCHOTTKY lines are placed further apart as the harmonic number grows.
3. SCHOTTKY noise power is constant in all bands, so the peak power decreases as the integral power smears over the larger bands.

This has two consequences, the first is the reduced needed acquisition time as can be immediately seen from the above mentioned relation: at harmonic m, only $1/m$ of the time is needed for the same Δf. In other words: for a given time, a much larger frequency band of $m\Delta f$ can be resolved. This speeds up the process of detection of a frequency peak.

The second is the increase in the mass resolution power for the given acquisition duration, which is not so straight forward and needs to be remedied: We have

$$f_r \pm \Delta f \rightarrow m(f_r \pm \Delta f)$$

at a higher harmonic m, so that the ratio $\Delta f / f$ remains the same at all harmonics. This is still **not** an advantage and this fact should be kept in mind for mass analysis formula (equation 5.2.1) which depends on this ratio. In order to make an advantage of it, if we can subtract the revolution frequency, or a large portion of it using a frequency mixer (see section A.1.2), then we will increase this ratio:

$$mf_r \pm m\Delta f - f_{LO} = f_{BB} \pm m\Delta f$$

where f_{LO} is the local oscillator frequency and $f_{BB} = mf_r - f_{LO}$ is the *base band frequency*. The base band frequency is chosen such that it satisfies the NYQUIST condition

$$f_{BB} + \Delta f < \frac{f_s}{2} \tag{4.1.2}$$

where f_s is the sampling rate (also refer to A.1.2). Now since

$$\frac{m\Delta f}{f_{BB}} > \frac{m\Delta f}{mf_r} = \frac{\Delta f}{f_r}$$

we have a higher mass resolution power which is ready to use with equation 5.2.1, while keeping all other parameters unchanged. In practice obtained spectra are averaged in time so that peaks are easier to detect.

Example 4.1.1 *The Pm particle of example 2.1.1 decays and produces the spectrum in figure 4.3 on page 82 where* $\Delta f = 1.6$ $[kHz]$. *Using relation 4.1.1 the signal must be recorded at least for 1.25 [ms]. If we would not use the higher harmonic number of 124, then the corresponding recording time would be 124 times longer, that is about 150 [ms].*

In practice, due to the complex structure of the storage ring and many factors that contribute to noise, longer times may be required to make some nuclides satisfactorily visible on the spectra, so that confident detection can be carried out.

Example 4.1.2 *With the capacitive pickups in the ESR about 10 [s] are required to detect a single ion with* $Z \sim 50$ *[*L^+05*]. For ions with a revolution frequency of about 2 [MHz], this corresponds to the* 30^{th} *harmonic in the capacitive pickup. Working at the* 124^{th} *harmonic would reduce this time by factor of 4, i.e. only 2.5 [s].*

As we can see, SCHOTTKY analysis at higher harmonics increases the frequency resolution i.e. reduced the required acquisition time and thereby speeding up the detection process. At this stage this advantage is general and there is nothing peculiar about the resonator. The specific role of the resonator becomes obvious with regard to the third point in the list above. The low peak power at higher harmonics can be largely enhanced using a resonant pickup. This is described in the following subsection.

Sensitivity

Equation 2.2.25 shows that the average signal power of a particle is directly proportional to the shunt impedance of the resonator. Higher shunt impedances can only be achieved using resonant structures. Depending on the geometry and material losses very high shunt impedances can be realised which can not be possible by conventional capacitive pick-ups.

Band width and Dynamic range

The bandwidth of the resonator is calculated in example 2.1.2 and depicted in figure A.4 (right). It is about 745 [kHz] for the loaded circuit, which is the normal operation mode in experiments. Within this bandwidth many nuclei can be simultaneously observed. In the in-ring mass spectrometry, this is specially useful for identification, e.g. isobars appear as triple lines near each other. Another use of such simultaneous view is calibration of the mass formula (equation 5.2.1) by comparing strong frequency components of known or stable isotopes, since both intense and weak signals are simultaneously visible. This assures a high dynamic range as far as the unknown peaks of interest are sufficiently away from the frequency spread of high intensity beam components.

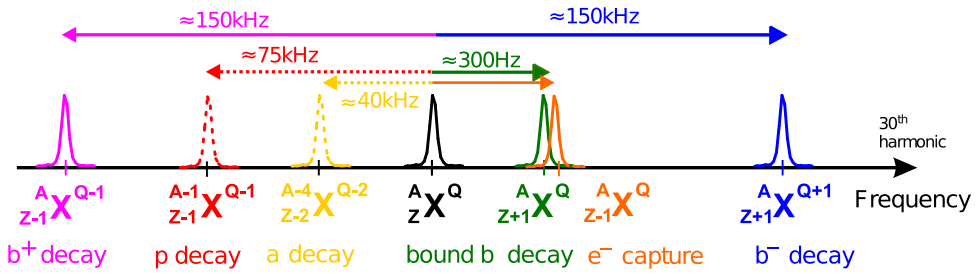

Figure 4.1: Schematic view of changes in frequency peaks due to changes in mass over charge ratio in an in-ring radioactive decay (from [Lit03]).

The closer the peak of interest is placed at the band center, the higher the gain will be. So by a combination of changing the resonance frequency using plungers and choosing a suitable SCHOTTKY harmonic, one can always place the desired signal peak at the top of the resonance curve, and of course both at the center of the spectrum analyser. For the in-ring decay studies, the analysis span can then be set according to the required frequency jump. A schematic of relative frequency changes due to different radioactive decays of stored highly charged ions can be seen in figure 4.1 [Lit03].

4.2.1 Single ion Decay Spectroscopy of highly Ionized ^{142}Pm

As a continuation of a series of studies on beta decay of stored highly charged ions [Lit09] [LB11], an experiment was designed to take advantage of the high sensitivity of the resonant pickup in the measurement of electron capture in the ^{142}Pm $\longrightarrow^{142}$ Nd system. In May 2010, a beam of a few Hydrogen-like (H-like) or alternatively Helium-like (He-like) ^{142}Pm was stored in the ESR to study its decay behaviour. ^{142}Pm was generated from ^{152}Sm fragmented on a 4 $[g/cm^2]$ beryllium production target, collected within the FRS fragment separator (see figure 1.1) and finally injected into the ESR with an energy of 400 MeV/u (β=0.71). Stochastic and electron cooling were used subsequently. Using time resolved SCHOTTKY spectroscopy, decay times could be measured with a time resolution of 32 ms. Figure 4.4 (on page 85) shows a single H-like ^{142}Pm particle decaying to ^{142}Nd by electron capture (EC) decay: the reaction can be schematically written as:$^{142}\mathrm{Pm}^{1e^-} \xrightarrow{EC} {}^{142}Nd^{0e^-} + \nu_e$. This is a two-body reaction, where the produced neutrino is monochromatic. The sudden change in the mass of the daughter nucleus causes a change in the m/q ratio, which is directly related to the revolution frequency [Lit03]. Since the decay energy is above 1.022 [MeV], a competing decay channel, namely positron emission or in other words continuous $\beta+$-decay also exists, but since both mass and charge change after decay, the daughter trace is far outside of the visible analysis span. Finally, a negligible amount of parent nuclei are also lost due to collisions with the remaining gas in the vacuum tube

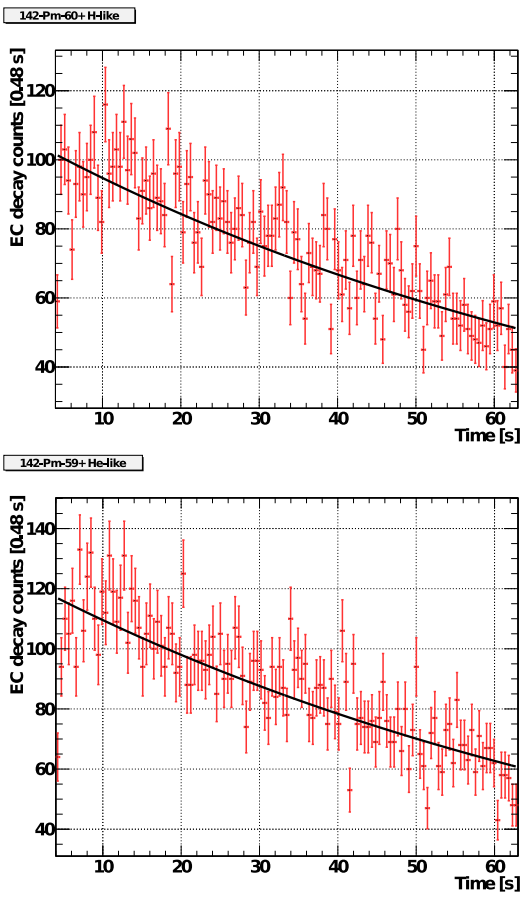

Figure 4.2: EC decay times of ^{142}Pm ions.

or via radiative recombination (electron capture) process in the electron cooler. The parent ions in figure 4.4 appear on the left side since their masses are higher and therefore have a lower revolution frequency. After each decay, the daughter nucleus can be ejected isotropically in all directions. This means that due to the two-body nature of the decay, the recoiling daughter ion has a defined recoil momentum but opposite to the momentum of the neutrino.

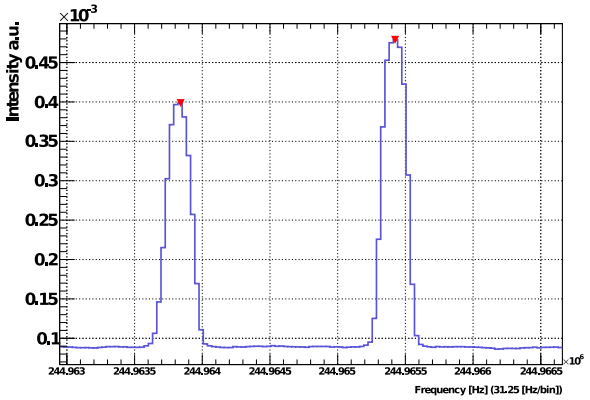

Figure 4.3: He-like ^{142}Pm (left) and bare ^{142}Nd peak (right) the $\Delta f \approx 1.6$ $[kHz]$ at 124^{th} harmonic.

The daughter nucleus is then cooled to the frequency (speed) corresponding to its mass over charge ratio. The curved lines are the cooling paths in the frequency space of the particles due to the force of the electron cooler. In the same figure the initial cooling after injection is also shown. Figure 4.2 shows decay times of He-like ^{142}Pm nuclei which occurred 4 [s] and 63 [s] after injection. Data was collected in bins each 480 [ms] long while every bin shows the standard error of $\sqrt{n}$, where n is the number of counts in that bin. For hydrogen-like nuclei an exponential fit with $\chi^2/\text{dof} \approx 1.4$ to the histogram shows a $\lambda_{lab} = 0.0116(6)$ $[s^{-1}]$ and for the helium-like nuclei with $\chi^2/\text{dof} \approx 1.6$ a $\lambda_{lab} = 0.0111(5)$ $[s^{-1}]$ in the lab frame. At 400 MeV/u, Pm ions have a relativistic $\gamma = 1.42$. The ratio of the two is

$$\frac{\lambda^H_{tot}}{\lambda^{He}_{tot}} = 1.04(7)$$

The resulting EC decay half-lives are

$$t^H_{1/2,cm} = \frac{ln(2)}{\gamma\lambda_{lab}} = 41.9(2.2)\ [s]$$

for the H-like ions and

$$t^{He}_{1/2,EC} = \frac{ln(2)}{\gamma\lambda_{lab}} = 43.8(2.2)\ [s]$$

for the He-like ions in the ion rest frame. The full half life considering the $\beta+$ channel as well is $t_{1/2,EC} = 40.5(5)$ $[s]$ [Tul00] (page 721). The Q value of the decay is given in the same reference as $Q_{decay} = 4870 \pm 40$ and elsewhere $Q_{decay} = 4820 \pm 100$ [R$^+$73] (page

36). The corresponding frequency change to this Q value is depicted in figure 4.3. Figure 4.5 shows the spectrum of three nuclei that decay subsequently through electron capture. The **absolute** instantaneous signal powers were determined using the spectrum analyser. For the noise level, an average of 40 channels was chosen. These values are written also in table 2.2 for comparison and show a relatively good agreement.

4.2.2 Beam intensity and life time measurements

Conventional beam current monitors act as a transformer that can determine the amount of beam current. But as we saw in equation 2.2.11, the beam current has many high frequency components. DC current transformers have some disadvantages: even those devices with high sensitivity suffer from a limited bandwidth which results in reduced performance at higher frequency components of the beam current.

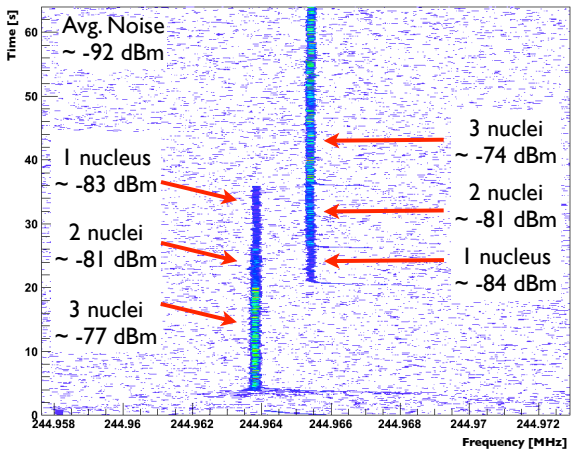

Figure 4.5: Approximte values of measured peak instantaneous signal power for different number of nuclei. Noise was averaged over 40 frames.

To achieve measurements of beams with very few ions, one can make use of the high sensitivity of resonant pickups at a harmonic band. It was discussed in the section 2.2 that the integral power in every band is constant and is related to the beam current according to equation 2.2.13. By measuring the area under the curve in a band one can obtain the integral power. The only problem is that absolute powers may change during all steps of signal processing, e.g. filtering, windowing, multi-tapering, etc. Also the number of points changes the level of thermal noise, so that it is difficult to determine at what level the signals can be distinguished from noise. A solution is to use an external DC current transformer (DCCT) as a calibration reference to determine I_B in equation 2.2.13 and to scale the area under the curve such that it corresponds to it. Finally one can use equation 2.2.9 to determine the number of ions.

In August 2012 several beams of ^{238}U were stored in ESR at relatively low energies. The electronics of the ESR DCCT delivers modulated frequency values that correspond to the

voltage caused by the beam current every millisecond. These values were averaged first in bins of 1 [s] duration. The offset was determined by fitting the background noise and was subtracted subsequently.

The profile of the area under SCHOTTKY spectrum was generated and was also corrected for offset. Both curves were moved in time so that their beginnings exactly match. Then, the SCHOTTKY spectra were averaged for every second. To avoid the Moiré effect, bins did not have fixed number of frames but instead fixed length in time. Finally these spectra were scaled such that their maximum at the beginning corresponds to that of the DC current transformer. The number of ions was calculated accordingly.

The beams of $^{238}U^{88+}$ were injected at 90 $[MeV/u]$ while the gas target was turned on, so that beam losses over several orders of magnitude could be observed. Beams of $^{238}U^{28+}$ were injected at energies of 50 $[MeV/u]$ and 30 $[MeV/u]$. For the observation of their decays no gas target was needed. The results can be seen in figure 4.6 on page 86. The resonant pickup is several orders of magnitude more sensitive than the DC current transformer, but of course its sensitivity depends on the beam energy. In these figures, the absolute error of the values delivered by the transformer was impossible to estimate due to many different components in the electronic chain. The effect of unknown uncertainties of transformer measurements was estimated to be below 10%. These uncertainties are not shown in figure 4.6. In fact transformer values have an error bar which propagates to the SCHOTTKY curve and increases the uncertainty specially in the plot with number of ions. Using a high precision DC current transformer with known uncertainty is suggested in section 5.2.

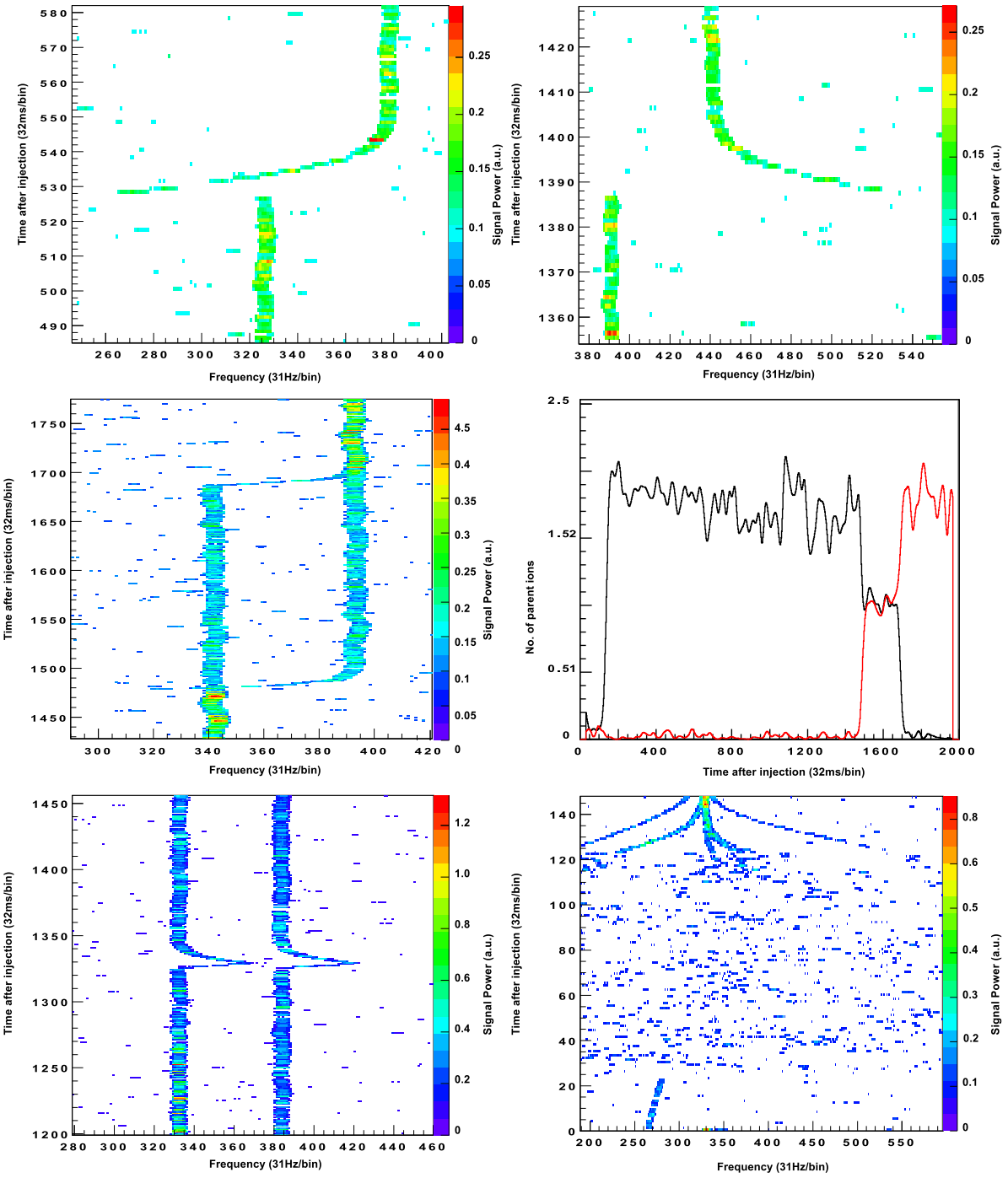

Figure 4.4: Single ion decays of Helium-like ^{142}Pm nuclei with different recoil directions (top). Two consecutive EC decays and their projection (middle). Power supply jitter in the spectrum of helium-like ^{142}Pm (bottom left). Stochastic and electron cooling of 5 hydrogen-like ^{142}Pm nuclei (bottom right).

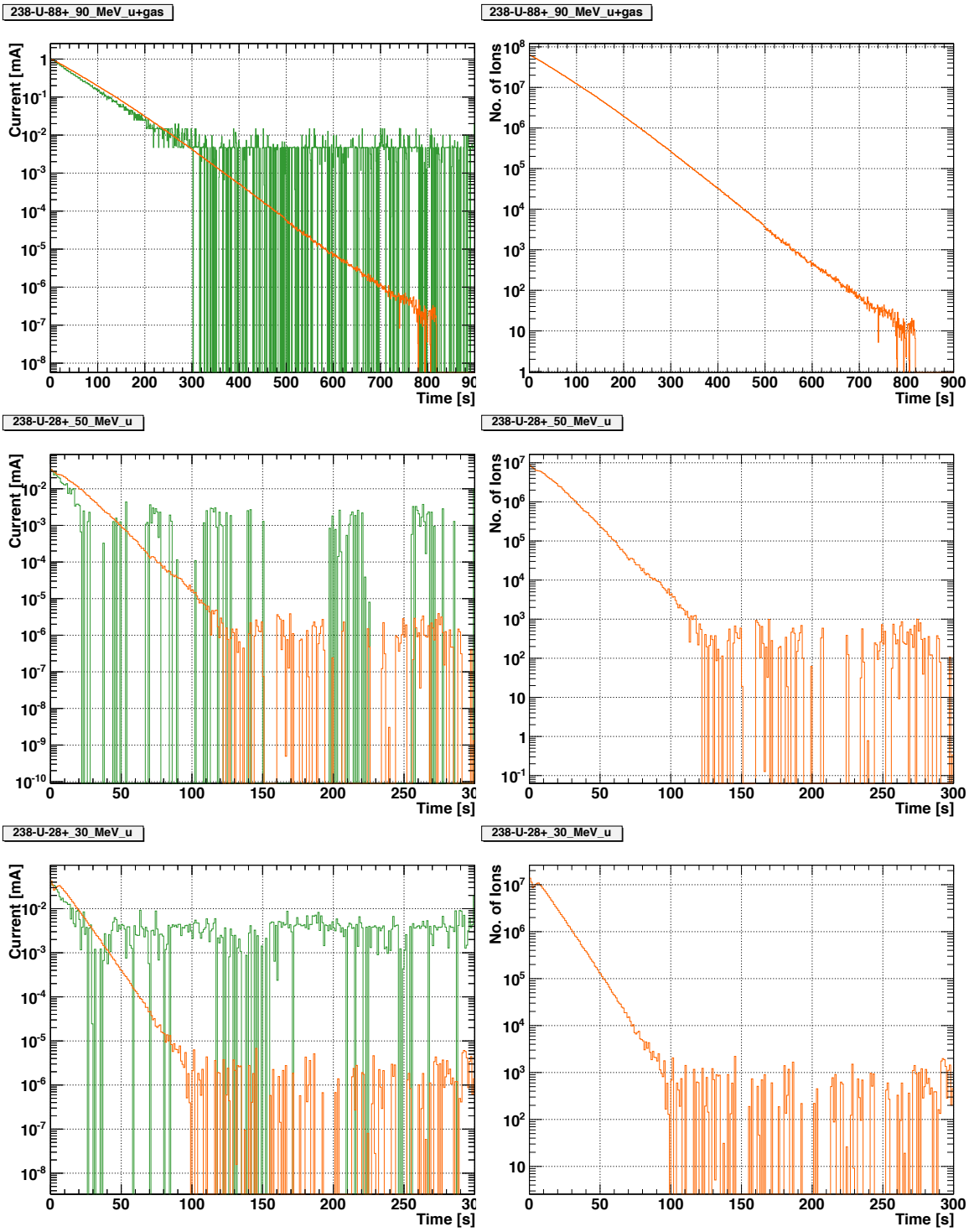

Figure 4.6: Resonant pickup (orange) vs. DC current transformer (green) measuring exponential loss of beam current intensity (left) and its corresponding number of ions (right) for $^{238}U^{88+}$ at 90 $[MeV/u]$, $^{238}U^{28+}$ at 50 $[MeV/u]$ and 30 $[MeV/u]$. The effect of the unknown uncertainties of the transformer measurements was estimated to be below 10%. The uncertainties are not shown here.

CHAPTER 5

SUMMARY AND OUTLOOK

5.1. Summary

A new resonant pickup was designed and commissioned into the heavy ion storage ring ESR at GSI Darmstadt in 2010 and at CSRe storage ring at IMP Lanzhou in 2011. With the pickup at GSI, single ion decay spectroscopy was achieved at 400 $[MeV/u]$. It was used in many experiments ever since as a principal detector.

In chapter 1 a brief history of particle accelerators and particle monitors is provided. Section 1.2 which describes the motivation for a non-destructive beam current monitor is followed by a brief list of previous works.

The theory of operation is provided in section 2. Additionally, in section A.1.1 detailed calculations of the electromagnetic of a pillbox is provided. Some of its field patterns and mode frequencies are shown in figure 2.2 and table 2.1. This section continues with the review of some fundamental concepts about wake functions and impedances. In section 2.1.2, modal parameters are presented. This is followed by a discussion on energy exchange in the particle-pickup system. SCHOTTKY noise theory is provided in section 2.2. Formulas for the single particle power and signal to noise ratio are derived in this section and are presented in equations 2.2.25 and 2.2.26. Some approximate results are shown in table 2.2 and figure 4.5.

The resonant pickups are based on a pillbox design with attached beam pipes as shown schematically in figure 2.4(a). Computer aided simulation results are provided in section 3.2. In table 3.4 it is shown that the simulated characteristic impedance is about 53 Ohms. The simulation of the transit time factor and higher order modes are shown in figure 3.7 and table 3.6. Some further details of simulation software are discussed in the appendix.

Mechanical dimensions are listed in table 3.1. The cutoff frequency of the beam pipe is about 918 $[MHz]$ and is calculated in section 2.1. The resonator has a resonant frequency

around 245 $[MHz]$ which can be tuned about ± 2 $[MHz]$ using remote controlled plungers (figure 3.2). The unloaded Q is about 1130. This together with other measurement results are listed in table 3.7 of section 3.3.1. The resulting equivalent circuit parameters of the resonator is calculated in example 2.1.2 where it is shown that $C_1 = 195$ $[pF]$ and $L_1 = 86$ $[nH]$ for the unloaded resonator and $C_1 = 97$ $[pF]$ and $L_1 = 172$ $[nH]$ for the loaded case. For both loaded and unloaded resonator $R_1 = 23.7$ $[k\Omega]$. The resulting transfer functions are depicted in figure A.4. The unloaded bandwidth is about 373 kHz and the loaded bandwidth is about 745 kHz. Finally the measurement of the characteristic impedance is discussed in section 3.3.2 and tables 3.8 and 3.9. Three different resonant methods were used and the results are listed in the table 5.1

	CAP	ROD	BEAD
GSI Resonator	~ 59	~ 35	N/M
IMP Resonator	N/M	$\sim 25\ to\ 50$	~ 42

Table 5.1: Summary of measurements of characteristic impedances. All values are in Ohms. N/M = not measured.

The loop antenna inside the resonator was tuned to have a coupling factor of unity. The amplifier chain that is connected to the instrument is shown in figure 3.4. The overall gain and noise figure is calculated in example 2.2.3. For the full chain we have $G_{total} = 77.5$ $[dB]$ and $NF_{total} = 1.95$ $[dB]$ and for the case where the third amplifier is out of the signal path, we have $G_{total} = 57.5$ $[dB]$ and $NF_{total} = 2.05$ $[dB]$. The signal is connected to a TEKTRONIX® **RSA3303B** real time spectrum analyser.

The instrument has a sampling rate of 32 ksps at an acquisition bandwidth of 20 kHz. The IQ data are therefore stored in time domain with a sampling time of 31.25 micro seconds. Using 2000 frames of each 1024 points which result in frames of 32 ms length, time resolved spectra of 64 seconds were generated. Single ion lifetime measurement were then performed as described in section 4.2.1. The offline analysis employed the multitaper method as described in section 2.2.4. Measurement of beam intensity was performed with Uranium beams as described in section 4.2.2.

5.2. Outlook

Several issues can be optimized in the future to allow higher time and frequency resolution accuracy or better experimental results. Some suggestions are provided in this section.

Other possible applications and future designs follow.

Suggestions

It is suggested to use non-resonant perturbation method for the estimation of the characteristic impedance when dealing with cavities that have low Q. In our case, a non-resonant method specially when performed in *transmission*, would deliver more accurate results. This can be combined with a mechanical structure, in which the thread and the bead are fixed and the resonator rolls slowly with stepper motors underneath. This has an advantage that due to the heavy weight of the resonator, more accurate movements can be achieved.

The sensitivity of absolute current measurements using the resonant pickup can be enhanced by using a very accurate beam current transformer for the calibration reference. This can be installed in the ESR. A possible candidate for such transformers are the so called DCCT or the "Unser" transformer named after K. B. UNSER [Uns92]. Meanwhile these transformers are commercially available as high precision complete modules that can be built into beam pipe e.g. NPCT from BERGOZ®.

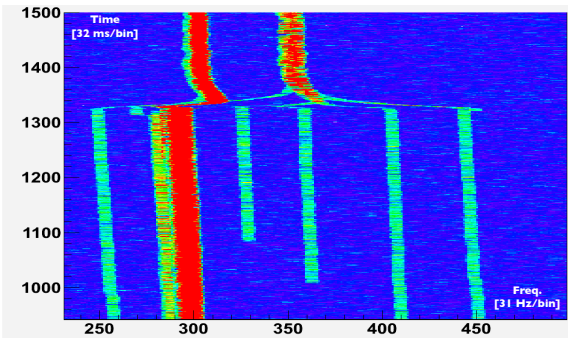

Figure 5.1: Increasing decay statistics.

It would be of interest to investigate the sensitivity of the pickup versus beam energy in a dedicated machine experiment. The result could then be considered as an approach to measure the transit time factor experimentally (cf. figure 3.7 left). But, there are also some difficulties: the ions must be stable and long-living with the specified charge state through all the region of energy scan of interest. This is of course impossible, so different ions-charge combinations will need to be used to cover different energy regions possibly with overlap, e.g. from 400 to 300 MeV/u, the other from 350 MeV/u down to 250 MeV/u and so on. The results from different curves must then be properly combined to obtain a unified behaviour.

Lifetime measurement without cooling

In order to increase the statistics in the lifetime measurement experiments, one could increase the number of injected ions per spill. But since the cooler always restores the daughter (and of course parent) nuclei to the frequency that corresponds to their mass over charge ratio, the peak power intensity increases on those frequencies, which in turn makes the detection process more difficult.

In order to circumvent this limitation, after initial cooling of the parent nuclei, the cooler can be turned off. After decaying, the daughter nuclei will therefore have different frequency spread depending on the magnitude of the longitudinal component of their recoil energy. This results in a spectrum with single lines, since for a few ions, the probability of having exactly the same recoil energy is still very low. At the end of the injection cycle, the cooler can be turned on again, in order to "collect" the nuclei.

During the beam time of 2010, some injections were used to test this possibility. An example of such technique can be seen in figure 5.1, where each of the five pale green lines indicate a single daughter ion. This way, decay times are clearly visible and a visual identification of nuclei becomes easier due to the cooling traces, since each nucleus will be cooled again to its related revolution frequency at the end of the cycle. An automatic identification is more demanding, especially for those single ion traces that are slower than the slowest parent ion.

This option can be combined with a beam shutter at the end of each cycle in order to make sure that the ring is empty before a new beam is injected. Clearing off the storage ring is an additional measure in case the ESR kicker magnet malfunctions in an injection cycle.

Single ion mass spectroscopy

One of the important quantities that describes matter is the atomic mass. Knowing exact values of atomic masses helps understand many fundamental concepts in physics and chemistry. This fact gave birth to many attempts to describe atomic masses theoretically and experimentally[1]. Accelerator facilities offer a possibility to determine nuclear mass in a precise way. Ions can be prepared with a defined charge state and stored in a trap or a storage ring. As it was mentioned in the introductory chapter, ions can be produced in ISOL facilities or using in-flight fragmentation. Some possible configurations are:

[1] An overview can be found in [Shu12].

- ISOL facility → trap (e.g. ISOLDE @ CERN)
- ISOL facility → storage ring (e.g. future proposal TSR@ISOLDE [Lin03])
- In-flight fragmentation → trap (e.g. HITRAP @ GSI)
- In-flight fragmentation → storage ring (e.g. FRS + ESR @ GSI)
- Hybrid: Fragmentation + stopping in a gas-cell and store in a trap (SHIPTRAP @ GSI)

Nuclear yield of ISOL facilities depend on chemical properties of the required elements, such that it is not possible to cover some regions of the nuclidic chart. In this sense in-flight facilities have an advantage that all particles in the nuclidic chart can in principle be produced through fragmentation. Furthermore, the process of chemical diffusion in ISOL facilities sets an lower bound on the life time of the nuclides that can be measured.

Mass measurements using traps is done using TOF-ICR or FT-ICR methods[2] [Bla06]. The first method is destructive and is not well suited for nuclei with extremely low production yields. The latter needs some time for frequency scan which makes it less suitable for short lived ion species.

Compared to traps, mass measurements in storage rings can be performed non-destructively with nuclei with low production cross section. So in the list above the last method is one of the good choices where it comes to mass measurements of exotic short lived nuclei. Here one can differentiate between two mass measurement methods, the *isochronous mass spectroscopy* (IMS) and the *Schottky mass spectroscopy* (SMS). These methods are now very well established and have been used in many experiments for determination of exotic nuclear species successfully [Sch97] [R$^+$00] [L$^+$05] and recently [Shu12]. The basic idea is to use the relation of the mass over charge ratio with the revolution frequency [Lit08].

$$\frac{\Delta f}{f} = -\alpha_P \frac{\Delta(\frac{m}{q})}{\frac{m}{q}} + \frac{\Delta v}{v}\left(1 - \frac{\gamma^2}{\gamma_T^2}\right) \tag{5.2.1}$$

where v, m, q, γ and f are the velocity, mass, charge, relativistic factor and revolution frequency of the particles and γ_T is the *transition gamma*. α_P is the *momentum compaction factor* which is equal to $1/\gamma_T^2$. Δf can then be used for calibration with known masses. In order to use this relation, one needs to cancel out the second term. In SCHOTTKY mass

[2]Time of flight ion cyclotron resonance and FOURIER transform ion cyclotron resonance

spectrometry cooling techniques are applied so that $\Delta\nu \rightarrow 0$, whereas in IMS[3] one tries to achieve $\gamma = \gamma_T$, and relies on a special, isochronous ion-optical setting of the ESR ring.

For SCHOTTKY mass spectroscopy in storage rings, spectral analysis is performed on the signals of the parallel plate SCHOTTKY monitors or a resonant pickup. This way, in contrast to measurements in traps, a broad spectrum with many nuclei can be measured. The mass resolving power is mainly limited by the spectral width of SCHOTTKY lines which is itself dominated by the velocity spread in the cooler. In ESR a mass resolving power of $\Delta m/m \approx 10^{-5}$ to 10^{-6} can be achieved.

Briefly, with a resonator it is possible to measure short lived nuclei (due to higher speed) with extremely low production yields down to single ions (due to high sensitivity). Like with the parallel plates, one can see a large portion of the nuclidic chart (broad band operation compared to traps) which contains many known and unknown masses of stable and unstable nuclei with high and low yields. Those stable nuclei with known masses and high yields can then simultaneously be used for calibration of those with small production yields (due to high dynamic range). Within the frequency resolution, isomeric states can also be analysed.

The transversal mode resonator

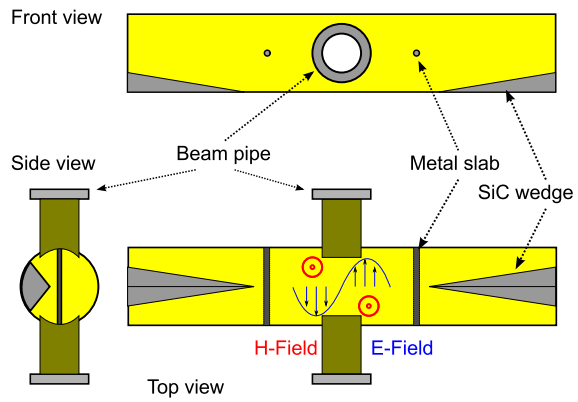

Figure 5.2: A possible model for the transversal resonator.

The TM010 mode can be excited only by the longitudinal component of the electric field of the beam and therefore cannot be used to detect the transversal position of the particles. As a result, spectra shown in this work, such as figure 5.1, show the component of the particle momentum only in the longitudinal direction. Hence for each decay, the resulting Δf can be associated to a point on the circumference of a circle in parallel to the beam axis. For full-kinematic studies, it would be of interest to determine the transversal component of the recoil as well. For that purpose transversal SCHOTTKY signals can be used together with a resonator

[3]Please refer to [Wol87] and [Lit08] for more details.

working in dipole mode, such as the TM020 mode as shown in figure 2.2. Transversal SCHOTTKY bands appear due to the dipole fluctuations caused betatron motion of the particles [Cha84]. Also the transversal pickup must have a linear response or be operated in a linear region, otherwise it will detect higher order moments as well [BL82]. The *betatron tune* is defined as the number of transversal oscillations that the particle does around the ideal *synchronous orbit*. The tune is usually set such that it is not an integer number of revolution frequency, otherwise it would cause instabilities due to resonance. The ratio is usually chosen to be rational and transversal SCHOTTKY bands are visible with the same frequency ratio around the revolution frequency f_r.

Apart from the pillbox geometry, other geometries such as figure 2.4(b) can be used to allow better control over field patterns. An example can be seen in figure 5.2. Here, the beam pipe enters in the resonator region. These will have curved cross section (see side view) in order to forbid the rotation of the dipole mode. Metal slabs trap the dipole mode optimally within the pipe region, whereas higher order modes propagate to the Silicon Carbide dampers. The use of higher order mode dampers can be seen in other designs as well, such as the Choke Mode Cavity [Shi92]. Finally a remote controlled mechanism can be installed inside of the tubes for the purpose of shorting the resonator, so that all components work in vacuum. Such a transversal resonator was proposed in 2011 for future developments in HESR in FAIR [KH11]. It will enable a range of novel technical capabilities for physics experiments. For example:

- If a position of a particle can be determined within a few thousand revolutions in a dispersive section of the ring, then a first-order correction related to the $\gamma_T = \gamma$ in equation 5.2.1 can be achieved.
- Full kinematic studies measurements become possible for atomic or nuclear processes.
- Transversal SCHOTTKY signals also allow determination of other beam parameters such as machine chromaticity [Cas09].

The planning of a prototype of a transversal SCHOTTKY resonator is in discussion for the ESR.

APPENDIX

A.1. Detailed Theoretical Descriptions

A.1.1 Electromagnetic waves in a bounded medium

Classical electromagnetism deals with magnetic and electric fields and the forces they apply on charged particles. Strictly speaking, magnetic fields can be seen as a side effect of the electric fields of relativistically moving charged particles in different frames as was known already as early as 1900 by LIÉNARD and WIECHERT. But, without loss of correctness, the overall effect can be handled in an abstract way as a magnetic field. A time varying electric field generates a magnetic field and a time varying magnetic field generates an electric field. Under such circumstances, the electric field is not conservative any more. This is manifested in a set of four MAXWELL*'s equations* which are listed in equations A.1.1.

$$\vec{\nabla} \times \vec{E} = -\frac{\partial \vec{B}}{\partial t} \qquad or \qquad \oint_C \vec{E} \cdot d\vec{l} = -\int_S \frac{\partial \vec{B}}{\partial t} \cdot d\vec{s} = -\frac{d\Phi}{dt} \tag{A.1.1a}$$

$$\vec{\nabla} \times \vec{H} = \vec{J} + \frac{\partial \vec{D}}{\partial t} \qquad or \qquad \oint_C \vec{H} \cdot d\vec{l} = \int_S \left(\vec{J} + \frac{\partial \vec{D}}{\partial t} \right) \cdot d\vec{s} \tag{A.1.1b}$$

$$\vec{\nabla} \cdot \vec{D} = \rho \qquad or \qquad \oint_S \vec{D} \cdot d\vec{s} = \int_V \rho \; dv = q \tag{A.1.1c}$$

$$\vec{\nabla} \cdot \vec{B} = 0 \qquad or \qquad \oint_S \vec{B} \cdot d\vec{s} = 0 \tag{A.1.1d}$$

$\vec{H}$ and $\vec{E}$ are *magnetic and electric field intensity vectors* measured in units of $[A/m]$ and $[V/m]$. $\vec{B} = \mu\vec{H}$ and $\vec{D} = \varepsilon\vec{E}$ are the *magnetic and electric flux density vectors*[1] measured in units of Tesla $[T]$ and $[C/m^2]$, where $\mu = \mu_r \, \mu_0 = \mu_r \times 4\pi \times 10^{-7} \; [H/m]$ and $\varepsilon = \varepsilon_r \varepsilon_0 \approx \varepsilon_r \times 8.854187817620 \times 10^{-12} \; [F/m]$, ε_r and μ_r are the dimensionless relative permittivity

[1] The electric flux density vector is also sometimes called the electric displacement vector

and permeability of the material in question. These equations together with the continuity equation:

$$\vec{\nabla} \cdot \vec{J} = -\frac{\partial \rho}{\partial t} \tag{A.1.2}$$

and the LORENTZ equation 1.1.1 form the foundation of classical electrodynamics. ρ is the *charge density* measured in units of $[As/m^2]$, Φ is the *magnetic flux* through a given surface measured in units of WEBER $[Wb]$ and finally q is the total charge in a given volume measured in units of COULOMBS $[C]$. The *current density vector* $\vec{J}$, may consist of the conduction current density i.e. movement of a charge density ρ or the convection current caused by an electric field in a conductor. In the following $\vec{v}$ is the velocity vector and σ is the conductivity of the material in units of SIEMENS $[S]$.

$$\vec{J} = \rho \vec{v} = \sigma \vec{E} \tag{A.1.3}$$

$\partial \vec{D}/\partial t$ has units of current density $[A/m^2]$, which justifies its addition to the $\vec{J}$ term that is measured in the same units. It can be thought of as a kind of current that flows through the dielectric materials by flipping the polarized material, for example the dielectric inside of a capacitor. This way loop integrals are still possible even if the conductor line is broken inside of a capacitor. This term was actually the main contribution of MAXWELL himself. The relation between the differential form and integral forms in the MAXWELLS's equations A.1.1 is based on two theories in vector calculus. The first one is GAUSS's Theorem[2] which relates the volume integral of the divergence of a vector field to the total outward flux of the vector field through the bounding surface.

$$\int_V \vec{\nabla} \cdot \vec{A} dv = \oint_S \vec{A} \cdot d\vec{s}$$

The second is the STOCKE's theorem

$$\int_S (\vec{\nabla} \times \vec{A}) \cdot d\vec{s} = \oint_C \vec{A} \cdot d\vec{l}$$

which states that a surface integral of the curl of a vector field over an open surface is equal to the closed path integral of the vector field around the bounding contour of that surface.

Finally, It can be seen from the first two equations that in contrast to the electrostatic or magneto-static case, where $\vec{\nabla} \times \vec{E} = 0$ and $\vec{\nabla} \times \vec{H} = 0$, in the time varying case, the electric

[2]Also known as divergence theorem

and magnetic fields are not curl-free. According to vector calculus, only curl-free vector fields can be written as the gradient of a scalar potential.

MAXWELL's equations are interrelated in the sense that the two divergence equations can in fact be derived from the two curl equations through the continuity equation. But all four are coupled and for a particle solution they need to be solved simultaneously. $\vec{E}$ and $\vec{H}$ describe physical fields that generally depend on time and position regardless of coordinate system used to describe them. In order to solve for these equations it is possible to reduce these four to two decoupled (partial differential) equations that can be treated independently. By choosing a vector potential $\vec{A}(\vec{r},t)$ and a scalar potential $\phi(\vec{r},t)$ that are defined such that:

$$\vec{B}(\vec{r},t) = \vec{\nabla} \times \vec{A}(\vec{r},t) \tag{A.1.4a}$$

$$\vec{E}(\vec{r},t) = -\vec{\nabla}\phi(\vec{r},t) - \frac{\partial}{\partial t}\vec{A}(\vec{r},t) \tag{A.1.4b}$$

where $\vec{r}$ is the position vector, two of four MAXWELL equations are satisfied automatically. This can be seen by putting these two identities in equations A.1.1a and A.1.1d and remembering vector calculus identities that curl of gradient of any scalar field is the zero vector and also divergence of curl of any vector field is zero. Similarly the two remaining equations follow:

$$\begin{aligned} \vec{\nabla} \cdot \vec{D} &= \rho \\ \vec{\nabla} \cdot \vec{E} &= \rho/\varepsilon \\ \vec{\nabla}^2\phi + \frac{\partial}{\partial t}\,\vec{\nabla} \cdot \vec{A} &= -\rho/\varepsilon \end{aligned} \tag{A.1.5}$$

by remembering that divergence of gradient of a scalar field is equal to its divergence squared. Also

$$\begin{aligned} \vec{\nabla} \times \vec{H} = \frac{1}{\mu}\,\vec{\nabla} \times \vec{\nabla} \times \vec{A} = \frac{1}{\mu}(\vec{\nabla}(\vec{\nabla} \cdot \vec{A}) - \vec{\nabla}^2\vec{A}) = \vec{J} + \varepsilon\frac{\partial}{\partial t}\left(-\vec{\nabla}\phi - \frac{\partial \vec{A}}{\partial t}\right) \\ -\vec{\nabla}^2\vec{A} + \mu\varepsilon\frac{\partial^2\vec{A}}{\partial t^2} = \mu\vec{J} - \vec{\nabla}\left(\vec{\nabla} \cdot \vec{A} + \mu\varepsilon\frac{\partial \phi}{\partial t}\right) \end{aligned} \tag{A.1.6}$$

By choosing $\vec{\nabla} \cdot \vec{A} = -\mu\varepsilon\frac{\partial\phi}{\partial t}$ the term in the parentheses in equation A.1.6 vanishes. This choice is called the LORENZ[3] gauge. In most cases of interest we observe fields that are already propagating and are far from the their generating source so that $\rho = \vec{J} = 0$.

[3]The gauge is named after Danish Ludvig Lorenz.

MAXWELL's equations reduce to two decoupled homogeneous partial differential equations

$$\vec{\nabla}^2\phi - \mu\varepsilon \frac{\partial^2\phi}{\partial^2 t} = 0 \tag{A.1.7a}$$

$$\vec{\nabla}^2\vec{A} - \mu\varepsilon \frac{\partial^2\vec{A}}{\partial t^2} = 0 \tag{A.1.7b}$$

Also electromagnetic fields of interest are almost always periodic in time so that

$$\vec{A}(\vec{r},t) = \vec{A}(\vec{r})\mathrm{e}^{i\omega_0 t} \Longrightarrow \frac{\partial^2}{\partial t^2}\vec{A}(\vec{r},t) = -\omega_0^2\vec{A}(\vec{r},t) \tag{A.1.8}$$

Finally, with the LAPLACIAN $\Delta = \vec{\nabla}^2$ potential equations reduce to:

$$\Delta\varphi + k^2\,\varphi = 0 \tag{A.1.9a}$$

$$\Delta\vec{A} + k^2\,\vec{A} = 0 \tag{A.1.9b}$$

where

$$k = \omega\sqrt{\mu\varepsilon} \tag{A.1.10}$$

is the *wave number*. These two equations bear many similarities to the ideal simple harmonic oscillator. Using an alternative definition instead of the vector potential in equation A.1.4 would lead to same wave equations A.1.9 where one could have chosen

$$\vec{D}(\vec{r},t) = \vec{\nabla}\times\vec{A}(\vec{r},t) \tag{A.1.11a}$$

$$\vec{H}(\vec{r},t) = \vec{\nabla}\phi(\vec{r},t) + \frac{\partial}{\partial t}\vec{A}(\vec{r},t) \tag{A.1.11b}$$

these two equations would fulfil equations A.1.1b andA.1.1c for the source free case, the other two are:

$$\begin{aligned} \vec{\nabla}\cdot\vec{B} &= 0 \\ \vec{\nabla}\cdot\vec{H} &= 0 \\ \vec{\nabla}^2\phi + \frac{\partial}{\partial t}\,\vec{\nabla}\cdot\vec{A} &= 0 \end{aligned} \tag{A.1.12}$$

and

$$\begin{aligned}\vec{\nabla}\times\vec{H}=\frac{1}{\varepsilon}\,\vec{\nabla}\times\vec{\nabla}\times\vec{A}=\frac{1}{\varepsilon}(\vec{\nabla}(\vec{\nabla}\cdot\vec{A})-\vec{\nabla}^2\vec{A})=-\mu\frac{\partial}{\partial t}\left(\vec{\nabla}\phi+\frac{\partial\vec{A}}{\partial t}\right)\\ -\vec{\nabla}^2\vec{A}+\mu\varepsilon\frac{\partial^2\vec{A}}{\partial t^2}=-\vec{\nabla}\left(\vec{\nabla}\cdot\vec{A}+\mu\varepsilon\frac{\partial\phi}{\partial t}\right)\end{aligned} \tag{A.1.13}$$

The step towards the wave equation is identical. Finally applying time harmonic conditions also to the $\vec{E}$ and $\vec{H}$ reduces MAXWELL's equations to:

$$\vec{\nabla}\times\vec{E}=-i\omega_0\mu\vec{H} \tag{A.1.14a}$$
$$\vec{\nabla}\times\vec{H}=i\omega_0\varepsilon\vec{E} \tag{A.1.14b}$$
$$\vec{\nabla}\cdot\vec{D}=0 \tag{A.1.14c}$$
$$\vec{\nabla}\cdot\vec{B}=0 \tag{A.1.14d}$$

Propagation through media

Propagation of electromagnetic waves in different media causes certain restrictions on the solution of the wave equations A.1.9. Some terminology is used often in the literature that describe different types of media. A *linear* medium is one in which electric (magnetic) field intensity and electric (magnetic) flux density are related to each other linearly, so that the constant of proportionality is the permittivity ε (permeability μ). In a *homogeneous* medium ε_r does not depend on position within the medium. An *isotropic* medium has no distinct direction. A *simple* medium is one which is linear, homogeneous and isotropic. A *source free* medium contains electromagnetic waves that are far away from their generating source, i.e. $\rho=0$ and $\vec{J}=0$ within the medium. A *non conductive* medium is one with $\sigma=0$. Finally a *lossy* medium has a complex permittivity and/or permeability $\varepsilon_c=\varepsilon'+i\varepsilon''$, where $\varepsilon'=\varepsilon$ and $\varepsilon''=\sigma/\omega$. The ratio $\varepsilon''/\varepsilon'$ shows the ratio of the conduction current to displacement current and accounts for ohmic losses. δ_s in

$$\tan\delta_s=\frac{\varepsilon''}{\varepsilon'}=\frac{\sigma}{\omega\varepsilon} \tag{A.1.15}$$

is called the *loss angle*. In a good conductor $\sigma\gg\omega\varepsilon$ and the reverse is true for a good insulator.

From many different possible solutions of the wave equation, the simplest case is the prop-

agation of wave in unbounded free space where it propagates only in forward direction. Far from the source, CARTESIAN coordinates is a suitable choice since, for an electric field say with a time varying component in the x direction, E_x, there will be only one magnetic field component H_y due to the cross product, and both are orthogonal to the wave propagation vector $\vec{k}$. Consequently, these solutions are called transverse electric and magnetic (TEM) solutions. The magnitude of the wave propagation vector becomes $k = k_0$ in equation A.1.9, the free space wave number

$$k_0 = \frac{2\pi}{\lambda_0} = \frac{2\pi f_0}{c_0} = \frac{\omega_0}{c_0} = \omega_0\sqrt{\mu_0\varepsilon_0} \tag{A.1.16}$$

measured in $[rad/m]$ where λ_0 is the wavelength. The relation between H_y and E_x is:

$$E_x(z) = \eta_0 H_y(z) \tag{A.1.17}$$

where $\eta_0 = \sqrt{\frac{\mu_0}{\varepsilon_0}} = 120\pi \approx 377\ [\Omega]$ is the *free space impedance*. For other dielectric material an intrinsic impedance can be defined as $\eta = \eta_r\eta_0$. The complex permittivity in lossy media, affects the wave number in the equation A.1.10, so the resulting wave number itself will be complex k_c. An example of such lossy medium is the ceramic used in the construction of the gap material of the resonant pickup as will be mentioned later in chapter 3. It is a *low loss dielectric* material with $\varepsilon'' \ll \varepsilon'$. Using equation A.1.10 a *propagation constant* γ is usually defined in the literature such that

$$\gamma = jk_c = j\omega\sqrt{\mu\varepsilon_c} = \alpha + j\beta \tag{A.1.18}$$

measured in units of $[m^{-1}]$, where β is the *phase constant* measured in $[rad/s]$. It shows how much the phase of the wave has changed after travelling a distance of one meter through the medium. α is called the *attenuation constant* measured in units of $[Np/m]$ meaning that, after travelling a distance $\delta = 1/\alpha$ through that medium, the original amplitude of the wave will be multiplied by the factor $e^{-1} = 0.368$ so it will be attenuated. δ is the depth of penetration of a wave into a conductive medium, also known as the *skin depth* of that medium. For low-loss dielectric materials the propagation constant is ([Che89]):

$$\gamma = \alpha + i\beta \approx \frac{\sigma}{2}\sqrt{\frac{\mu}{\varepsilon}} + i\,\omega\sqrt{\mu\varepsilon}\left[1 + \frac{1}{8}\left(\frac{\sigma}{\omega\varepsilon}\right)^2\right] \tag{A.1.19}$$

From the equation it is clear that the attenuation constant is almost directly proportional

to the conductivity of the material. For the case of good conductors this becomes

$$\alpha = \beta = \sqrt{\pi f \mu \sigma}.$$

So the skin depth in a conductor is:

$$\delta = \frac{1}{\sqrt{\pi f \mu \sigma}} \tag{A.1.20}$$

This shows that at very high frequencies the field is confined in a layer under the surface of the conductor. This fact must be taken into account in the construction of accelerator components like our resonator of this work, that are made of steel and need copper coating on the inner wall. The copper coating must be larger than the skin depth. Finally, it is noteworthy to mention that while the magnetic and electric field intensity are in phase in a lossless medium, this is not the case for lossy media, and they are 45° out of phase in good conductors.

Boundaries and cavity resonators

The characteristics of each medium through which the wave propagates applies certain restrictions on the solutions of the wave equations. From the fact that $c_0 = 1/\sqrt{\mu_0 \varepsilon_0}$ it is clear that the speed of propagation of electromagnetic waves is smaller in media with larger permittivity and permeability. If the wave is passing through several media, then the border between these act as boundary conditions for the solutions of the PDEs. On each boundary, some portion of the wave is reflected back and some is transmitted. The extent to which the wave is transmitted or reflected can be mathematically modelled by the coupling between two oscillatory systems, i.e. the incident electromagnetic wave and the confinement. A 'hard' boundary causes a larger reflection amplitude, whereas a 'soft' boundary causes a larger transmission amplitude on that boundary.

It is possible to use this reflection property at boundaries to actually *guide* the wave in a certain direction. If a one dimensional confinement exists, then the wave is guided between two infinite planes. A two dimensional confinement is a *wave guide*. Wave guides can have different shapes such as a rectangular or circular hollow pipes or even normal cables or patches of conductor on a flat printed circuit board. In the case of three dimensional confinement, the wave can be trapped. Here we talk about a *microwave cavity* or a *cavity resonator*. As it will be clear soon the name suggests that cavity resonators behave like

systems described in section A.1.4. Of course if waves need to be kept inside a volume, wall materials that cause highest reflection and least transmission are most suitable.

The applied confinement has the effect that the resulting frequency spectrum becomes discrete and only certain propagation frequencies, *the eigenfrequencies* are allowed, so that the overall spectrum consists of infinite number of simple harmonic oscillations. To each of these eigenfrequencies a specific propagation pattern or *mode* is related. The shape of the cavity can be designed so that some of these modes have a 'softer' coupling and some 'harder', so that one talks about different coupling constants for each mode. The 'softer' the coupling, the easier it is to excite a given mode, because more energy is going through and less is reflected. One talks about perfect *matching* when all of the power from the source is transmitted to the sink without reflection at the boundary.

Other confinement configurations including the case of wave guides are discussed in the literature[Col00]. For this work, the case of cavity resonators is most relevant, which will be discussed in the following. In real cavities, the harmonic oscillations in different modes are not ideal, at least due to thermal losses as we will encounter later. So to the equation of each of the modes a damping constant must be added which takes care of the losses. Consequently, every mode has a distinct Q value.

The behaviour of $\vec{E}$ and $\vec{H}$ at boundaries can be derived from the MAXWELL's integral equations (see e.g. [Che89]). For the tangential and transversal components of the field vectors $\vec{E}$ and $\vec{H}$ we have:

$$E_{1t} = E_{2t} \tag{A.1.21a}$$

$$\vec{n}_2 \times (\vec{H}_1 - \vec{H}_2) = \vec{J}_s \tag{A.1.21b}$$

where $\vec{n}$ is the normal vector to the surface of the second boundary, and $\vec{J}_s$ is the surface current density in $[A/m]$. For the normal components of $\vec{B}$ and $\vec{D}$ the conditions are as follows where ρ_s is the surface charge density in units of $[C/m^2]$ and B as usual in $[T]$:

$$B_{1n} = B_{2n} \tag{A.1.22a}$$

$$\vec{n}_2 \cdot (\vec{D}_1 - \vec{D}_2) = \rho_s \tag{A.1.22b}$$

It is important to note that, since as mentioned before, the two divergence equations can be derived from the two curl equations through the continuity condition, so these two sets of boundary conditions are not independent form each other. Only *one* of these sets must

be used for a given problem, since simultaneous use of both sets causes contradictions. An important case is the investigations of the boundary condition between two lossless media where there are no free charges and no surface currents. So, equations A.1.21 and A.1.22 are simplified as follows [Che89]:

$$E_{1t} = E_{2t} \rightarrow \frac{D_{1t}}{D_{2t}} = \frac{\varepsilon_1}{\varepsilon_2} \tag{A.1.23a}$$

$$H_{1t} = H_{2t} \rightarrow \frac{B_{1t}}{B_{2t}} = \frac{\mu_1}{\mu_2} \tag{A.1.23b}$$

$$D_{1n} = D_{2n} \rightarrow \varepsilon_1 E_{1n} = \varepsilon_2 E_{2n} \tag{A.1.23c}$$

$$B_{1n} = B_{2n} \rightarrow \mu_1 H_{1n} = \mu_2 H_{2n} \tag{A.1.23d}$$

We will need this boundary condition later for the description of the perturbation measurement. Another important boundary condition is the interface between perfect vacuum (medium 1) and a perfect electric conductor (PEC, medium 2). In this case the boundary conditions in equations A.1.21 and A.1.22 reduce to:

$$E_{1t} = 0 \qquad E_{2t} = 0 \tag{A.1.24a}$$

$$\vec{n}_2 \times \vec{H}_1 = \vec{J}_s \qquad H_{2t} = 0 \tag{A.1.24b}$$

$$\vec{n}_2 \cdot \vec{D}_1 = \rho_s \qquad D_{2n} = 0 \tag{A.1.24c}$$

$$B_{1n} = 0 \qquad B_{2n} = 0 \tag{A.1.24d}$$

$\vec{n}$ is an outward normal vector from medium 2 (PEC) extending into medium 1.

Microwave cavities can have any shape. In fact the theory of oscillation patterns can be calculated for arbitrarily shaped cavities (see e.g. [Col00]). In accelerator physics mostly right circular cylindrical symmetric shapes are used due to the practical manufacturing process, so that the solution of the wave equations are most convenient in cylindrical coordinates. Furthermore in cylindrical coordinates solutions of PDEs can have an analytic form using the separation of variables.

Unlike the solutions of the free wave equation, where $\vec{E}$ and $\vec{H}$ vectors are both orthogonal to each other and to the wave propagation vector $\vec{k}$, in a bounded medium this is not always the case, since apart from the vector potential defined in equation A.1.4 an alternative definition delivers another set of solutions. The general solution is a *superposition* of these solutions. In each of these solution sets the component of either $\vec{E}$ or $\vec{H}$ along the propagation direction is zero. The former set is called *transverse magnetic* or TM and the latter *transverse electric* or TE solutions. TE/TM means that $\vec{E}/\vec{H}$ has no components in the

direction of propagation and the other two components along the spacial coordinates are transverse to it. TM solutions are obtained using equations A.1.4 and A.1.14b, whereas TE solutions are obtained using equations A.1.11 and A.1.14a.

TM solutions:

$$\vec{H} = \vec{\nabla} \times \vec{A} \tag{A.1.25a}$$

$$\vec{E} = \frac{1}{i\omega_0 \varepsilon} \vec{\nabla} \times \vec{H} \tag{A.1.25b}$$

TE solutions:

$$\vec{E} = \vec{\nabla} \times \vec{A} \tag{A.1.26a}$$

$$\vec{H} = -\frac{1}{i\omega_0 \mu} \vec{\nabla} \times \vec{E} \tag{A.1.26b}$$

An ideally cylindrical cavity is an evacuated cylinder with perfectly conducting walls in which electromagnetic waves can bounce back and forth. This theoretical model serves as a starting point for many real applications where of course many deviations from the ideal case must be introduced, at least the electromagnetic waves must somehow couple to the resonator via a coupling mechanism, which already alters the ideal shape and that in turn changes the *mode geometry*. Nevertheless the field equations of the theoretical model are still very useful for further analysis. Here we adapt the derivation procedure described in [Ung02] and [Wei08], although other approaches in the literature in principle lead to same results. The idea is to find a vector potential $\vec{A}$ that can be put in equations A.1.25 and A.1.26 to find the components of the electromagnetic fields inside the resonator [Ung89].

For TM waves we have:

$$E_r = C \frac{1}{j\omega_0 \varepsilon} \frac{\partial^2}{\partial r \partial z} A_z \tag{A.1.27a}$$

$$E_\varphi = C \frac{1}{j\omega_0 \varepsilon r} \frac{\partial^2}{\partial \varphi \partial z} A_z \tag{A.1.27b}$$

$$E_z = C \frac{1}{j\omega_0 \varepsilon} \left(\frac{\partial^2}{\partial z^2} + k^2 \right) A_z \tag{A.1.27c}$$

$$H_r = C \frac{1}{r} \frac{\partial}{\partial \varphi} A_z \tag{A.1.27d}$$

$$H_\varphi = -C \frac{\partial}{\partial r} A_z \tag{A.1.27e}$$

$$H_z = 0 \tag{A.1.27f}$$

For TE waves we have:

$$E_r = -C \frac{1}{r} \frac{\partial}{\partial \varphi} A_z \tag{A.1.28a}$$

$$E_\varphi = C \frac{\partial}{\partial r} A_z \tag{A.1.28b}$$

$$E_z = 0 \tag{A.1.28c}$$

$$H_r = C \frac{1}{j\omega_0 \mu} \frac{\partial^2}{\partial r \partial z} A_z \tag{A.1.28d}$$

$$H_\varphi = C \frac{1}{j\omega_0 \mu r} \frac{\partial^2}{\partial \varphi \partial z} A_z \tag{A.1.28e}$$

$$H_z = C \frac{1}{j\omega_0 \mu} \left(\frac{\partial^2}{\partial z^2} + k^2 \right) A_z \tag{A.1.28f}$$

The constant C is a scaling factor and can stand for E_0 and H_0, arbitrary amplitudes that define the intensity of the excitation and don't change the mode patterns. In numerical simulations it can be set to any value[4]. As we will see later, it will cancel out in the expression for the Q value. In real applications it simply depends on the driving section. The next step is to solve the wave equation A.1.9. In cylindrical coordinates, it can be solved by the method of separation of variables where it can be written as a multiplication of three functions that each depend only on r, φ or z. For that we take a vector potential that has a single component in z direction since this assumption leads to a well defined system of equations (cf. [MFH54] chapter 13.1).

$$\vec{A} = A_z \vec{e}_z = f(r)g(\varphi)h(z)\,\vec{e}_z \tag{A.1.29}$$

and the fact that $\Delta\vec{A} = \nabla^2\vec{A} = \nabla^2 A_z\,\vec{e_z}$, the vector valued (cf. A.1.5) wave equation reduces to a scalar wave equation. After substituting A_z in the wave equation and dividing both sides again by A_z, the wave equation becomes:

$$\frac{1}{rf(r)}\frac{\partial}{\partial r}\left(r\frac{\partial f(r)}{\partial r}\right) + \frac{1}{r^2 g(\varphi)}\frac{\partial^2 g(\varphi)}{\partial \varphi^2} + \frac{1}{h(z)}\frac{\partial^2 h(z)}{\partial z^2} + k^2 = 0 \tag{A.1.30}$$

The first two terms do not depend on z, so in order for the equation to be satisfied for arbitrary z, the third term must also be a constant, which we call $-k_z^2$.

$$\frac{1}{h(z)}\frac{\partial^2 h(z)}{\partial z^2} = -k_z^2 \tag{A.1.31}$$

Further we multiply both sides by r^2 and rewrite the equation as

$$\frac{r}{f(r)}\frac{\partial}{\partial r}\left(r\frac{\partial f(r)}{\partial r}\right) + \frac{1}{g(\varphi)}\frac{\partial^2 g(\varphi)}{\partial \varphi^2} + (k^2 - k_z^2)r^2 = 0 \tag{A.1.32}$$

Here again, the second term must be a constant for varying φ.

$$\frac{1}{g(\varphi)}\frac{\partial^2 g(\varphi)}{\partial \varphi^2} = -m^2 \tag{A.1.33}$$

After substitution and multiplication with $f(r)$ and renaming $k_r = k^2 - k_z^2$ we have:

$$r\frac{\partial}{\partial r}\left(r\frac{\partial f(r)}{\partial r}\right) + \left[(k_r r)^2 - m^2\right] f(r) = 0 \tag{A.1.34}$$

[4]For example a value of $E_0 = 1MV/m$ was chosen for the simulation section.

Summarizing the above mentioned interrelations between different wave numbers we have:

$$k^2 = k_r^2 + k_z^2 \tag{A.1.35}$$

Separation of variables helped us extract three ordinary differential equation A.1.31, A.1.33 and A.1.34 from the wave equation. The first two are harmonic oscillators with harmonic solutions, whereas thanks to the correct choice of the constants, the third can be identified as a BESSEL differential equation. It is known from the theory of differential equations ([Ung02]) that for a given order m, the general solution of the BESSEL differential equation is a linear combination of the BESSEL functions of the first and the second kind. The latter are also called NEUMANN or WEBER functions and are alternatively denoted as N_m. These are plotted in figure A.1.

$$f_m(r) = C' J_m(r) + C'' N_m(r) \tag{A.1.36}$$

where C' and C'' are some constants. Based on these and the existing boundary conditions on the walls of the cylinder, the vector potential in equation A.1.29 can be constructed.

$$A_z = f_m(k_r r) g(m\varphi) h(k_z z) \tag{A.1.37}$$

First we discuss boundary conditions with radial dependence. From the plots in figure A.1 it can be seen that if a region is enclosing the z axis, which is always the case for cylindrical cavities, then solutions are only allowed to consist of BESSEL functions of the first kind, since NEUMANN functions are not regular there. BESSEL and NEUMANN functions describe a standing wave pattern in the radial direction. Although not applicable to cylindrical resonators, it is worth mentioning that if there are no bounds in radial direction, the waves can propagate. For such waves, similar to the CARTESIAN case, where we construct an exponential function for the propagating waves using $\cos(x) \pm i \sin(x)$, we construct the HANKEL functions of the first and second kind $H_m(x) = J_m(x) \pm i N_m(x)$. These functions are used in *sector horn antennas*. Finally, BESSEL functions are generalized by the MATHIEU functions for cylinders with elliptic cross sections.

If the region is enclosing the whole $0 \leq \varphi \leq 2\pi$, which is again the case for a cylinder, then $g(\varphi)$ must satisfy $g(\varphi) = g(\varphi + 2\pi)$ so that the solution is unique for every point. An arbitrary choice of the origin can allow either a sine or a cosine term. Up to now, the r and φ dependencies of the vector potential are the same in both circular waveguides and

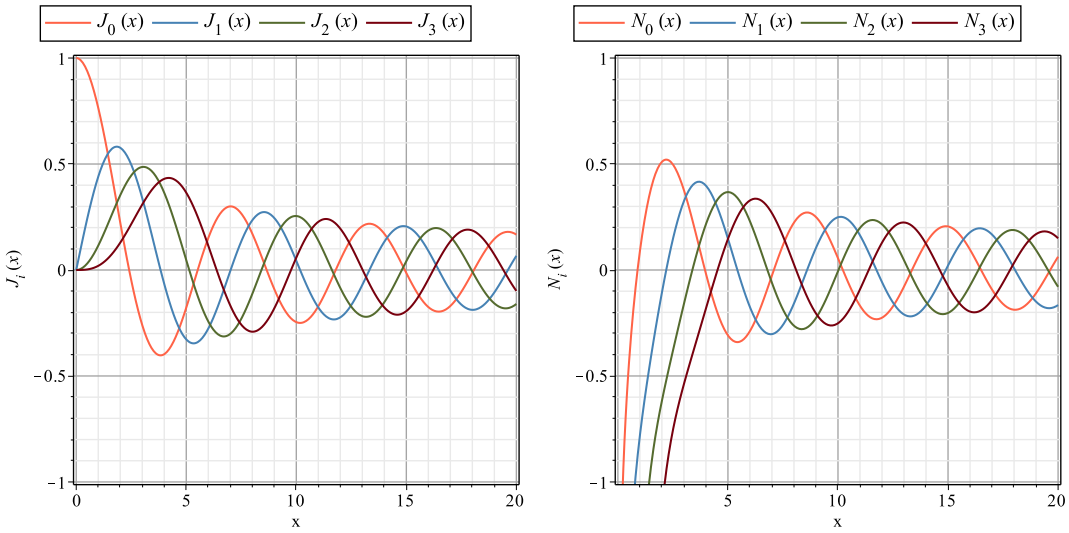

Figure A.1: First four Bessel functions of first and second kind.

circular cavities.

$$A = J_m(k_r r) \left\{ \begin{array}{c} \sin(m\varphi) \\ \cos(m\varphi) \end{array} \right\} h(k_z z) \tag{A.1.38}$$

Since the wave constructs an standing wave pattern along the z axis as described by equation A.1.31, the final solution is constructed by superimposing two *propagating* waves in in the direction of z and $-z$ axis with reversed amplitude and it is results in a sin or cos term. In other words two propagating waveguide modes are superimposed so that multiples of $\frac{\lambda_z}{2}$ fit inside the depth d of the resonator. With $d = p\frac{\lambda_z}{2}$, we have:

$$k_z = \frac{2\pi}{\lambda_z} = \frac{2\pi}{\frac{2d}{p}} = \frac{p\pi}{d} \tag{A.1.39}$$

Boundary conditions in equation A.1.24 state that the tangential electric field components (E_r and E_φ) must vanish at the end caps. For TE modes it is required that the z dependency of A_z causes E_r and E_φ to vanish. This is satisfied if we choose the z dependent term to be $\sin(k_z z)$. Simultaneously for TM modes, it is required that the *derivative* of the z dependency vanishes. We choose the z dependency to be $\cos(k_z z)$.

For the value of k_r we need to consider the two cases of TM and TE waves, so that finally two wave functions are obtained for TM and TE modes. Here again boundary conditions in equation A.1.24 state that the tangential electric field components (E_z and E_φ) must vanish at the walls, that is $r = \varrho$. For TM modes the responsible term is the r dependent part of the A_z which must vanish at $r = \varrho$ so that $J_m(k_r \varrho) = 0$. This situation is satisfied

if we choose $k_r = \frac{j_{mn}}{\varrho}$ where j_{mn} is the n^{th} zero of the m^{th} BESSEL function of the first kind (compare with figure A.1) so $J_m(k_r\varrho) = 0$. Same is with TE modes where E_z is zero anyway so we require E_φ to become zero which in turn requires that the derivative of the r dependency vanishes. That means $J'_m(k_r\varrho) = 0$ and it can be satisfied with $k_r = \frac{j'_{mn}}{\varrho}$ where j'_{mn} is the n^{th} zero of the first derivative of the m^{th} BESSEL function of the first kind. As a result of these considerations we obtain the following wave functions [Ung89]:

$$A^{TM}_{z,mnp} = J_m\left(\frac{j_{mn}}{\varrho}r\right)\begin{Bmatrix}\sin(m\varphi)\\ \cos(m\varphi)\end{Bmatrix}\cos\left(\frac{p\pi}{d}z\right) \qquad with\begin{cases} m = 0,1,2\cdots \\ n = 1,2,3\cdots \\ p = 0,1,2\cdots \end{cases} \tag{A.1.40a}$$

$$A^{TE}_{z,mnp} = J_m\left(\frac{j'_{mn}}{\varrho}r\right)\begin{Bmatrix}\sin(m\varphi)\\ \cos(m\varphi)\end{Bmatrix}\sin\left(\frac{p\pi}{d}z\right) \qquad with\begin{cases} m = 0,1,2\cdots \\ n = 1,2,3\cdots \\ p = 1,2,3\cdots \end{cases} \tag{A.1.40b}$$

By putting these expressions in equations A.1.27 and A.1.28, the resulting field components TM_{mnp} and TE_{mnp} can be obtained. The expression for E_z in eqaution A.1.27c simplifies to $E_z = C\frac{1}{i\omega_0\varepsilon}k_r^2 A_z$ by twice integrating with respect to z and using the relation in equation A.1.35. For TM modes we have:

$$E_r(r,\varphi,z) = -C\frac{1}{i\omega_0\varepsilon}\frac{p\pi}{d}\frac{j_{mn}}{\varrho}\left[\frac{m\varrho}{r\,j_{mn}}J_m\left(\frac{j_{mn}}{\varrho}r\right) - J_{m+1}\left(\frac{j_{mn}}{\varrho}r\right)\right]\begin{Bmatrix}\sin(m\varphi)\\ \cos(m\varphi)\end{Bmatrix}\sin\left(\frac{p\pi}{d}z\right) \tag{A.1.41a}$$

$$E_\varphi(r,\varphi,z) = -C\frac{m}{i\omega_0\varepsilon r}\frac{p\pi}{d}J_m\left(\frac{j_{mn}}{\varrho}r\right)\begin{Bmatrix}\cos(m\varphi)\\ -\sin(m\varphi)\end{Bmatrix}\sin\left(\frac{p\pi}{d}z\right) \tag{A.1.41b}$$

$$E_z(r,\varphi,z) = +C\frac{1}{i\omega_0\varepsilon}\left(\frac{j_{mn}}{\varrho}\right)^2 J_m\left(\frac{j_{mn}}{\varrho}r\right)\begin{Bmatrix}\sin(m\varphi)\\ \cos(m\varphi)\end{Bmatrix}\cos\left(\frac{p\pi}{d}z\right) \tag{A.1.41c}$$

$$H_r(r,\varphi,z) = +C\frac{m}{r}J_m\left(\frac{j_{mn}}{\varrho}r\right)\begin{Bmatrix}\cos(m\varphi)\\ -\sin(m\varphi)\end{Bmatrix}\cos\left(\frac{p\pi}{d}z\right) \tag{A.1.41d}$$

$$H_\varphi(r,\varphi,z) = -C\frac{j_{mn}}{\varrho}\left[\frac{m\varrho}{r\,j_{mn}}J_m\left(\frac{j_{mn}}{\varrho}r\right) - J_{m+1}\left(\frac{j_{mn}}{\varrho}r\right)\right]\begin{Bmatrix}\sin(m\varphi)\\ \cos(m\varphi)\end{Bmatrix}\cos\left(\frac{p\pi}{d}z\right) \tag{A.1.41e}$$

$$H_z(r,\varphi,z) = 0 \tag{A.1.41f}$$

For TE_{mnp} modes we have:

$$E_r(r,\varphi,z) = -C\frac{m}{r}J_m\left(\frac{j'_{mn}}{\varrho}r\right)\begin{Bmatrix}\cos(m\varphi)\\-\sin(m\varphi)\end{Bmatrix}\sin\left(\frac{p\pi}{d}z\right) \tag{A.1.42a}$$

$$E_\varphi(r,\varphi,z) = C\frac{j'_{mn}}{\varrho}\left[\frac{m\varrho}{r\,j'_{mn}}J_m\left(\frac{j'_{mn}}{\varrho}r\right) - J_{m+1}\left(\frac{j'_{mn}}{\varrho}r\right)\right]\begin{Bmatrix}\sin(m\varphi)\\\cos(m\varphi)\end{Bmatrix}\sin\left(\frac{p\pi}{d}z\right) \tag{A.1.42b}$$

$$E_z(r,\varphi,z) = 0 \tag{A.1.42c}$$

$$H_r(r,\varphi,z) = C\frac{1}{i\omega_0\mu}\frac{p\pi}{d}\frac{j'_{mn}}{\varrho}\left[\frac{m\varrho}{r\,j'_{mn}}J_m\left(\frac{j'_{mn}}{\varrho}r\right) - J_{m+1}\left(\frac{j'_{mn}}{\varrho}r\right)\right]\begin{Bmatrix}\sin(m\varphi)\\\cos(m\varphi)\end{Bmatrix}\cos\left(\frac{p\pi}{d}z\right) \tag{A.1.42d}$$

$$H_\varphi(r,\varphi,z) = C\frac{m}{i\omega_0\mu r}\frac{p\pi}{d}J_m\left(\frac{j'_{mn}}{\varrho}r\right)\begin{Bmatrix}\cos(m\varphi)\\-\sin(m\varphi)\end{Bmatrix}\cos\left(\frac{p\pi}{d}z\right) \tag{A.1.42e}$$

$$H_z(r,\varphi,z) = +C\frac{1}{i\omega_0\mu}\left(\frac{j'_{mn}}{\varrho}\right)^2 J_m\left(\frac{j'_{mn}}{\varrho}r\right)\begin{Bmatrix}\sin(m\varphi)\\\cos(m\varphi)\end{Bmatrix}\sin\left(\frac{p\pi}{d}z\right) \tag{A.1.42f}$$

The resonance frequency of each mode can be determined from the expression of the wave number in equations A.1.10 and A.1.35 for TM and TE modes with

$$k^2_{mnp} = |\vec{k}|^2 = \left(\frac{\omega_0}{c_0}\right)^2 = k_x^2 + k_y^2 + k_z^2 = k_r^2 + k_z^2 = \left(\frac{j_{mn}}{\varrho}\right)^2 + \left(\frac{p\pi}{d}\right)^2 \tag{A.1.43}$$

so that

$$f^{TM}_{0,mnp} = \frac{c_0}{2\pi}\sqrt{\left(\frac{j_{mn}}{\varrho}\right)^2 + \left(\frac{p\pi}{d}\right)^2} \tag{A.1.44a}$$

$$f^{TE}_{0,mnp} = \frac{c_0}{2\pi}\sqrt{\left(\frac{j'_{mn}}{\varrho}\right)^2 + \left(\frac{p\pi}{d}\right)^2} \tag{A.1.44b}$$

So for any given geometry an infinite set of possible modes exists. This is true for 1D (infinite parallel planes), 2D (waveguides) and 3D confinements (cavity resonators). In order to identify infinitely many modes of a time harmonic field, an index is used to determine how many half sinusoids of the field exist in a certain direction. In CARTESIAN coordinates, for a rectangular wave guide TM_{mn} corresponds to a wave propagating in z directions, with m wavelengths in x direction and n wavelengths in the y direction. Automatically this means that the z component of the magnetic field is zero and the wave can be described by 5 other components (E_x, E_y, E_z, H_x, H_y). The same naming convention

is used for cavities where a third index is added. If a cavity is perfectly symmetric, say a cube in CARTESIAN coordinates, it is arbitrary to choose which index belongs to which axis unless symmetry is broken in another way. For a cylindrical cavity it is convenient to align the depth of the cylinder along the z axis of the cylindrical coordinate system. In this case $TM_{mnp} = TM_{123}$ means a wave pattern with 5 components (E_r, E_φ, E_z, H_r, H_φ and $H_z = 0$) where 1 wavelength of the magnetic field fits in r and 2 wavelengths of it fit between 0 an 2π and 3 wavelengths of it fit in z direction. The first of these modes is called the *fundamental mode* and others are denoted as *higher order modes* (HOM). Waves with frequencies outside these discrete levels have real γ, their amplitude vanishes and they cannot propagate and become *evanescent*. In hollow waveguides the fundamental frequency is also denoted as the *cutoff* frequency. Frequencies below cutoff cannot propagate in the hollow waveguide. By contrast, a double conductor wave guide such as a coaxial cable can allow frequencies down to zero (i.e. DC Current) for obvious reasons. Finally Modes with the same characteristic frequency are called *degenerated*.

A.1.2 Fourier analysis in Hilbert space

The FOURIER series can be defined as a decomposition of a vector into an orthonormal basis of the HILBERT space. In order to better formulate this concept, a description of the main ideas is provided here whereas the interested reader is referred to advanced texts in Algebra, such as [Hel69]. The algebraic roots of the spectral analysis is one of the interesting topics in mathematics that also plays an important role in many areas of theoretical physics.

Algebraic spaces can have infinitely countable or uncountable dimensions. In the former case the spaces may also be finite dimensional. Vectors or functions are elements of such spaces, so they are called vector spaces or function spaces accordingly. The most intuitive vector space is the three dimensional EUCLIDEAN space that we use for our description of macroscopic world we deal with in daily life.

In linear algebra, a *linear form*, sometimes called a *linear functional* is a special case of linear mapping or function from V to K, where V is the vector space defined on the field of numbers (scalars) K. As a simple example we observe the vector $\vec{x}$ defined in the vector space $\mathbb{R}^3$ on the field of real numbers $\mathbb{R}$. Then a $f(\vec{x}) = a_1x_1 + a_2x_2 + a_3x_3$ is a linear form defined in the space $\mathbb{R}^3$ on the field of real numbers $\mathbb{R}$. A *bilinear form* is similar to a linear

form but it is a function that maps $V \times V$ onto the field K.

$$B(\vec{x}, \vec{y}) = \sum_{i,j=1}^{n} a_{ij} x_i y_j \tag{A.1.45}$$

The matrix B has dimensions $n \times n$. If the bilinear form is symmetric, i.e. $B(\vec{x}, \vec{y}) = B(\vec{y}, \vec{x})$ and the first and the second argument are referring to the same vector, one talks about a *quadratic form*. If the field of scalars is the field of complex numbers $\mathbb{C}$, one is often interested in a special bilinear form called *sesquilinear form*. In contrast to bilinear forms, which are linear to both sides, this form is linear for the right argument and anti-linear for the left argument, and maps $\bar{V} \times V \to \mathbb{C}$ where $\bar{V}$ is the complex conjugate of V.

A special class of bilinear forms may also be denoted as inner products. Especially in physics where A is usually chosen to be the identity matrix, they are written as $(\cdot, \cdot)$ or $\langle \cdot | \cdot \rangle$ and show the component of the first vector along the second. A *norm* can be defined if the associated bilinear form is symmetric and positive definite. Then the square root of the corresponding quadratic form is called *norm* or L^2-norm of the vector $\| \cdot \|$, e.g. $\|\vec{x}\| = \sqrt{(\vec{x}, \vec{x})} = \sqrt{\langle x | x \rangle}$. This also applies to a sesquilinear form, e.g. $\|\vec{x}\| = \sqrt{(\vec{x}^*, \vec{x})} = \sqrt{\langle x | x \rangle}$ where $\vec{x}^* = \langle x |$ is the dual of the vector $\vec{x}$. For the function space the inner product in the sesquilinear sense takes the form $\langle x, y \rangle = (x(t), y(t)) = \int \overline{x(t)} y(t)\, dt$ where t can be understood as a parameter or index which is taken to be time for signals in most physical applications.

A set of n linearly independent vectors e_n that span an n-dimensional vector space are called *basis*. If $e_1, \cdot e_n)$ is an orthonormal basis, then each of the basis vectors is orthogonal to another. An arbitrary vector in that vector space may be described as the sum of its projections along each of the basis vectors $\vec{e_k}$ so that

$$|x\rangle = \sum_{k=1}^{n} \langle x | e_k \rangle | e_k \rangle \tag{A.1.46}$$

Same is with an square integrable function in an infinite dimensional function space where

$$x(t) = \sum_{k=1}^{n} (x(t), e_k(t)) e_k(t) \tag{A.1.47}$$

The BESSEL inequality states that sum over the length of all projections is either smaller or equal to the norm of the vector itself, i.e.

$$\sum_{k=1}^{n} |\langle x | e_i \rangle|^2 \leq \|\vec{x}\|^2 \tag{A.1.48}$$

This inequality turns into an equality, called PARSEVAL's identity (a generalization of the PYTHAGOREAN theorem) for all orthogonal projections, that is, bilinear forms that are symmetric and positive definite.

For periodic functions with period T_0 it is of interest to study the projections of the function along the periodic vectors of the basis. This can be used to 'detect' periodicities. A suitable set of basis vectors are n orthonormal vectors $e_k(t) = \exp(i2\pi kt/T_0)$, where $k = 1, 2, \cdots, n$ and $i = \sqrt{-1}$. The dimensions of the space containing all these basis vectors is countably infinite. By making projections of the function/vector $x(t)$ in one interval T_0 of the parameter (usually time) along each of these basis functions/vectors starting by $k = 1$ then $k = 2$ and so on, we measure how large its components are along these axes. This projection is a measure of periodicity of the function at frequencies ω_0, $2\omega_0$, $3\omega_0$ and so on where $\omega_0 = 2\pi/T_0$, i.e. it gives frequency components of the original function that oscillate at these frequencies. The *longer* the signal oscillates with a frequency component in the interval T_0 is, the larger is its projection along a corresponding axis.

The resulting sesquilinear inner product with the basis vectors described earlier are the so called FOURIER coefficients c_k:

$$c_k = \frac{1}{T_0} \int_{-T_0/2}^{T_0/2} x(t)\, \mathrm{e}^{-ik\omega_0 t}\, dt \tag{A.1.49}$$

where the normalization is due to the finite integral limits, and the sum of all of them is the FOURIER *series*

$$x(t) = \sum_{k=-\infty}^{\infty} c_k\, \mathrm{e}^{ik\omega_0 t} \tag{A.1.50}$$

For $k = 0$ the above equation shows the first component of the discrete valued c_k sequence,

$$c_0 = \frac{1}{T_0} \int_{-T_0/2}^{T_0/2} x(t)\, dt \tag{A.1.51}$$

which shows the *average value of the signal over a period*. The coefficients c_k are in general complex valued. Their amplitude and phase can be plotted versus angular frequency ω to show their *amplitude* and *phase spectrum*. If $|c_k|^2$ are plotted versus the angular frequency, then the result is called *power spectrum*. In this case these spectra are not continuous because k is defined for integers only. So the spectrum of a periodic signal is discrete and all its components are to be found on k multiples of the fundamental (angular) frequency

ω_0 [Ran87]. Finally, the normalised[5] average power is calculated using:

$$P = \frac{1}{T_0} \int_{-T_0/2}^{T_0/2} |x(t)|^2 \, dt \tag{A.1.52}$$

Now the PARSEVAL's identity allows us to understand how the normalised average power or simply signal power is related to the coefficients c_k:

$$\frac{1}{T_0} \int_{-T_0/2}^{T_0/2} |x(t)|^2 \, dt = \sum_{k=-\infty}^{\infty} |c_k|^2 \tag{A.1.53}$$

Written out in words it means that the normalized average power of a periodic signal is equal to the sum of all of the components of its power spectrum. This is of course clear since the signal has only one specific energy content regardless of its representation. Finally it is possible to represent equation A.1.50 using real and imaginary parts:

$$x(t) = \frac{a_0}{2} + \sum_{k=1}^{\infty} \left(a_k \cos(k\omega_0 t) + b_k \sin(k\omega_0 t) \right) \tag{A.1.54}$$

with

$$a_k = \frac{2}{T_0} \int_{-T_0/2}^{T_0/2} x(t) \cos(k\omega_0 t) \, dt \tag{A.1.55}$$

$$b_k = \frac{2}{T_0} \int_{-T_0/2}^{T_0/2} x(t) \sin(k\omega_0 t) \, dt \tag{A.1.56}$$

In the FOURIER series decomposition the periodicity of the original signal is taken for granted. Although this might be the case for many signals originating from physics experiments, most signals are not periodic. In order to circumvent this limitation, the FOURIER transform is used. It can be shown [Hsu10] that the FOURIER series representation is still valid when we allow the signal to have an infinite period. The resulting form is a transition from the sums to integrals and is called the FOURIER transform $\mathscr{F}$[6] and is defined as follows:

$$X(\omega) = \mathscr{F}\{x(t)\} = \int_{-\infty}^{\infty} x(t) \mathrm{e}^{-i\omega t} \, dt \tag{A.1.57}$$

[5] Normalization can be achieved for example by calculating the power of the signal dissipated in a resistor with a value of 1Ω

[6] Also called the continuous time FOURIER transform

$$x(t) = \mathscr{F}^{-1}\{X(\omega)\} = \frac{1}{2\pi}\int_{-\infty}^{\infty} X(\omega)\mathrm{e}^{i\omega t}\, d\omega \tag{A.1.58}$$

Here the space of basis vectors $\exp(i\omega t)$ is uncountably infinite dimensional. By definition the transformation with the negative exponential power is called the forward FOURIER transform and the transformation with the positive power called the inverse FOURIER transform. The Pareval's theorem is also valid here, stating that

$$\int_{-\infty}^{\infty} |x(t)|^2\, dt = \int_{-\infty}^{\infty} |X(\omega)|^2\, d\omega \tag{A.1.59}$$

The most general form of the PARCEVAL's theorem is called PLANCHEREL's theorem which has a wide definition range and is applicable on other orthogonal bases as well such as spherical functions [Hel84].

In practice, signal processing is mostly done using the FOURIER transform, regardless of the fact whether the original signal is periodic or not. It is also important to note that the spectrum of a real valued signal is symmetric with respect to ordinate whereas for a complex valued signal this is not the case. Finally if the integration limits are bounded, that is, the signal under test is of finite duration, then one talks about *finite Fourier transform*. We now need a mechanism to convert signals to numbers so that they can be processed by FOURIER analysis in computers.

Signals and periodic sampling

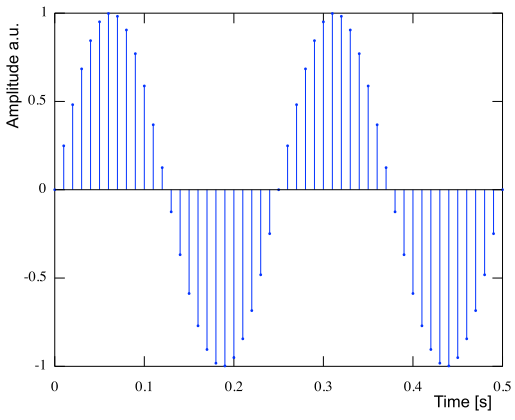

Figure A.2: A sampled sinusoidal signal.

In the previous section we justified the algebraic notation of FOURIER decomposition. In physics such vectors may represent a sequence of measured values of a physical observable in different times. They might also represent values that are functions of position, for example light intensity on the sensor of a digital camera. We use the term *signal* to denote such a vector of measured values. All signals that we encounter in this work are single functions of time. FOURIER analysis provides us with the means of analysing frequency contents of signals under test. Signals may be continuous

functions of time like the temperature of a green house at different times, or they may be defined on discrete values. One example might be values of stock market at the end of every day. Continuous signals can be converted to sequences of discrete data by means of *sampling* of the value of an observable at discrete times. Sampled signals can easily be processed in computers. Understanding them is of fundamental importance in experimental physics. Signals which are results of a measurements in experimental physics are real valued signals. Same is with signals that are given back to the experiment set-up, e.g. a desired value of temperature for a tungsten heater. Complex valued signals may arise naturally as results of signals processing in steps in between the input and output of a set-up. One such complex valued signal can easily be made from a real valued signal $x(t)$ in that we perform:

$$\tilde{x}(t) = x(t) + i\, x(t) \tag{A.1.60}$$

In practice this is achieved by adding a 90 degrees phase shifted version of the signal to itself. In computer terms, such a signal can be thought of as just two vectors of values instead of one. For a periodic signal with period T_0, no matter complex or real valued, the following functional equation is satisfied

$$x(t + T_0) = x(t) \tag{A.1.61}$$

T_0 is called the *fundamental period*, $f_0 = 1/T_0$ is called the *fundamental frequency* and finally $\omega_0 = 2\pi f_0 = \dfrac{2\pi}{T_0}$ is the *fundamental angular frequency*.

In experimental physics, signals can either be directly expressed in terms of voltages or currents or are observables that can be converted to them using suitable electronic devices such as *transducers* or *detectors*. This voltage can then be measured using voltage monitor (e.g. an oscilloscope) or a ampere meter. In order to make a sequence of values from a continuous signal, we should perform a periodic measurement. Mathematically this is equivalent to multiplying a sequence of DIRAC delta pulses

$$p(t) = \sum_{-\infty}^{\infty} \delta(t - nT_s) \tag{A.1.62}$$

with the original continuous time signal [Zou10]

$$x_s(t) = x_c(t)p(t) = \sum_{-\infty}^{\infty} x(n)\, \delta(t - nT_s) \tag{A.1.63}$$

Delta pulses extract the value of the signal at each sequential time, since according to the

definition we have

$$\int_{-\infty}^{\infty} x(t)\delta(t-t_0)\,dt = x(t_0) \tag{A.1.64}$$

An example is shown in figure A.2 where a 4 Hz sinusoidal signal with a duration of 500 ms is sampled at 100 samples per second. The stems are just a visualization that emphasize discrete data points. A consequence is that the FOURIER transform of a sampled signal is periodic in frequency domain with identical frequency content placed around multiples of sampling frequency. Following this concept, a phenomenon called *aliasing* is responsible for loss of information when a transition between continuous time and discrete time is made. If the number of sampled points is not large enough, then it may not be possible to unambiguously assign the resulting sequence to the original continuous signal. In other words, assuming we have a sequence of measured values, since we can not guess how the original signal behaved *between* the points, we may not identify the original signal unambiguously. There is a limit to this as explained by the NYQUIST or SHANNON theorem:

THEOREM 2 *The frequency of taking samples (sampling rate) must be at least 2 times faster than the fastest frequency component of the signal in order to avoid aliasing.*

This is of course true only for *band limited signals*, that is signals that have a signal content within a finite frequency band. It is not possible to avoid aliasing for a signal with infinite frequency content[7]. As an example, if an observable is converted to a voltage drop across a resistor and its values are recorded every 31.25 microseconds i.e. a sampling rate of 32 kilo samples per second (ksps), then we can only expect to reconstruct a signal with a maximum frequency content of 16 kHz. A sinusoidal signal with a frequency of 2 kHz can be unambiguously reconstructed, but if a signal has frequency components both below and above 16 kHz, then those components that lie above cause aliasing, whereas components below are reconstructed properly. The mentioned frequency is in fact the sampling frequency that was used during this work for some experimental results.

In many physical applications the relevant information of a signal is stored in its frequency shape. A shape can be a change in frequency for example a chirp signal which starts with a frequency f_1 and ramps up to the frequency f_2. Other examples are in communications like in modulations and in accelerator physics as in synchrotron side band signals. As stated above, in order to study such signals, one needs to sample them with an appropriate sampling frequency. For example if a sinusoidal signals changes its frequency from $f_1 =$

[7] e.g. a theoretical time signal that consists of one Dirac delta pulse

2.001 MHz to $f_2 = 2.002$ MHz, then we need to sample the signal with at least 4.22 mega samples per seconds (Msps). Since we are not interested in any frequency content below 2 MHz we may subtract that from our original signal so that the resulting frequencies are then $f_1' = 1$ kHz and $f_2' = 2$ kHz. So this signal can be easily analysed in a the system of our above example. The device which does this is called a *frequency mixer* and is denoted by a $\otimes$ in schematics. Internally it may contain active diodes or transistors depending on the specifications. Frequency mixing is an essential tool in many applications in accelerator physics and control.

Finally it should be mentioned that in practical applications not only the signal is discrete in time, but for processing in computers it is also needed that they are also discrete in amplitudes. The higher the number of amplitude steps, the higher the amplitude resolution of the signal. One usually talks about number of bits, e.g. 14-bit means a range of $-2^{13}+1$ to 2^{13}, including zero and allowing one bit for sign.

Discrete Fourier transforms and spectrogram

After obtaining a sequence of data $x[n]$ of a continuous signal $x(t)$, the signal can be further processed using the *discrete time Fourier transform* (DTFT). Since in practical applications a discrete signal has a finite length N, the sum is bounded and one defines the Discrete FOURIER Transform (DFT) as:

$$X[\kappa] = \frac{1}{N}\sum_{n=0}^{N-1} x[n]\, \mathrm{e}^{-i\frac{2\pi n\kappa}{N}} \tag{A.1.65}$$

$$x[n] = \frac{1}{N}\sum_{k=0}^{N-1} X[\kappa]\, \mathrm{e}^{i\frac{2\pi n\kappa}{N}} \tag{A.1.66}$$

The Parseval's theorem for the DFT is

$$\sum_{\kappa=0}^{N-1} |x[n]|^2 = \frac{1}{N}\sum_{\kappa=0}^{N-1} |X[\kappa]|^2 \tag{A.1.67}$$

Now we are ready to perform the transformation in a computer. For that we need to implement the expression in equation A.1.65. This involves nested loops and many multiplications which increases the computation time and is costly in sense of hardware resources specially when an on-the-fly transformation is needed (see e.g. [MV01] page 332). An efficient method called the *fast Fourier transform* short FFT exists which deals with such

difficulties. It is optimized as such that it reuses many multiplication terms that are results of symmetries in the equation, given that the length of the time signal[8] is 2^N. There are many implementations of the FFT algorithm. One of the most popular libraries that implements FFT is the FFTW [FFT11]. It is freely available and is already used in the core of many other free and even commercial applications.

Given a sequence of discrete time data $x[n]$, one can generate the spectrum $X[k]$ over the whole data length. In this case the frequency content of the signal is clearly visible. But if the signal under test is a non-stationary or a quasi-stationary signal that changes its frequency content with time, it will not be possible to detect *when* that change has happened by looking at the spectrum. Instead if the time signal is divided into smaller segments, then the spectrum of each segment is calculated, so it is possible to see in which segment a new spectral component has appeared. This is called a *spectrogram* and the results are usually displayed in a two dimensional color coded plot showing time, frequency and magnitude or power of the frequency components. In a real-time system, where signals or continuously being processed and immediately displayed, the plot may also be named a *waterfall diagram*. *The larger the number of time signals, the better the time resolution, but the worse is the frequency resolution.* This is due to the fact that there are fewer point available in each segment, over which the transformation in equation A.1.65 can be performed. Having this trade-off in mind, spectrograms specially when performed in real-time are one of the most indefensible tools in the experimental physics, by which particle trajectories can be monitored.

Instantaneous, average and RMS Power

Assuming a periodic source, the energy delivered to a resistor is:

$$W_R = \int_0^{T_0} p(t)\,dt \tag{A.1.68}$$

where

$$p(t) = u(t)i(t) = \frac{u^2(t)}{R} = i^2(t)R \tag{A.1.69}$$

is the *instantaneous power*. It is important to notice that the *average dissipated power* or the *heating power* in the resistor is <u>not</u> equal to the multiplication of average values of voltage

[8] Otherwise zeros are added to the end of the sequence. This is called *zero padding*

and current

$$\langle P \rangle \neq \langle U \rangle \langle I \rangle$$

but

$$\langle P \rangle = U_{rms}\, I_{rms} \tag{A.1.70}$$

RMS means root of the average of the squared value of the function, exactly in that order, i.e. $\sqrt{\langle f^2 \rangle}$. For a sinusoidal signal $u(t) = U_{peak} \sin(\omega t)$ we have for any interval:

$$\begin{aligned} U_{rms} = \sqrt{\langle u^2(t) \rangle} &= \sqrt{\frac{1}{T_2 - T_1} \int_{T_1}^{T^2} u^2(t)\, dt} \\ &= \sqrt{\frac{1}{T_2 - T_1} \int_{T_1}^{T_2} U_{peak}^2 \sin^2(\omega t)\, dt} \\ &= U_{peak} \sqrt{\frac{1}{T_2 - T_1} \int_{T_1}^{T_2} \left(\frac{1}{2} + \frac{1}{2} \cos(2\omega t) \right) dt} \\ &= U_{peak} \sqrt{\frac{1}{T_2 - T_1} \frac{T_2 - T_1}{2}} \\ &= \frac{1}{\sqrt{2}} U_{peak} \end{aligned} \tag{A.1.71}$$

where U_{peak} and U_{rms} are numbers in units of volts [V] that don't depend on time. The same relation exists between I_{peak} and I_{rms}. Also $\langle P \rangle$ is a constant of time. So for the special case of sinusoidal signals we have:

$$\langle P \rangle = I_{rms}^2 R = \frac{U_{rms}^2}{R} = \frac{1}{2} I_{peak}^2 R = \frac{1}{2} \frac{U_{peak}^2}{R} \tag{A.1.72}$$

The concept of RMS Power P_{rms} has no useful meaning, since it doesn't represent the dissipated power, except in the case of a DC current [Lew09].

A.1.3 Random processes and thermal noise

Apart from the deterministic signals, another class of signals are the so called stochastic or *random signals* or *random processes*. In order to define them, we first need to define *random variables*. A random variable $X(\zeta)$ is a single valued real function that assigns a real number $X(\zeta)$ to each outcome ζ of a random experiment. In other words, it is a number assigned to every outcome of an experiment ([Zou10],). $X(\zeta)$ is mostly written

as just X. An *event* $(X = x)$ is defined as

$$(X = x) = \{\zeta : X(\zeta) = x\}$$

and the probability of that event is defined as:

$$P(X = x) = P\{\zeta : X(\zeta) = x\}$$

A random variable can be characterized by its *cumulative distribution function* **(cdf)** defined as

$$F_X(x) = P(X \leq x)\ , -\infty < x < \infty$$

that means the probability of the event $(X \leq x)$. If the r.v. is continuous, then its *probability density function* (**pdf**) is defined as the derivative of its cdf.

$$\begin{gathered} f_X(x) = \frac{dF_X(x)}{dx} \\ \text{or} \\ F_X(x) = P(X \leq x) = \int_{-\infty}^{x} f_X(\xi)\, d\xi \end{gathered} \tag{A.1.73}$$

The pdf of a random variable is positive and the area under it is unity. Several quantities can be assigned to random variables, such as mean, variance and higher order moments. These are introduced in the following to avoid repetition.

A random process on the other hand describes signals with random properties, that is, a signal whose amplitude takes a random value at every point in time $X(t)$. So $X(t)$ is a r.v. variable for a fixed t. Such signals are not predictable, no matter how long the observation time is. But there are some properties that can be used to characterize such signals. The mean and variance of a random process are its first and second order moments functions and are defined as

$$\mu(t) = \mathbb{E}[X(t)] = \int_{-\infty}^{\infty} x(t) \cdot f_X(x;t)\, dx \tag{A.1.74}$$

$$\sigma_X^2(t) = \mathbb{E}[X(t)^2] - \mathbb{E}[X(t)]^2 = \int_{-\infty}^{\infty} x^2(t) \cdot f_X(x;t)\, dx \tag{A.1.75}$$

The *autocorrelation function* of the random process $X(t)$ is the second order moment func-

tion for two different times t_1 and t_2 and is defined as

$$\begin{aligned} r_{XX}(t_1;t_2) &= \mathbb{E}[X(t_1)X(t_2)] \\ &= \int_{-\infty}^{\infty}\int_{-\infty}^{\infty} x_1(t)x_2(t) f_{X_1X_2}(x_1(t),x_2(t);t_1,t_2)\,dx_1dx_2 \end{aligned} \tag{A.1.76}$$

For a complex random process, the equation will change to $r_{XX}(t_1;t_2) = E[X(t_1)X^\star(t_2)]$, where $\star$ denotes complex conjugate. Random processes are classified according to their properties. Two important classes are *stationary* and *ergodic* processes. A *stationary process*[9] is a random process whose statistical properties (F_X, f_X, μ, σ) don't change with time. In this case the time difference between the two points of interest so that $r_{XX}(\tau) = E[X(t)X^\star(t-\tau)]$. An ergodic process is a process whose time average is equal to its expectation. Every ergodic process is also stationary but not vice versa. Proof of ergodicity is usually very difficult since for a given process, it must be proved that time average of a sample function and the expectation of the process is equal up to *infinite order*, i.e. for the first, second, $\cdots$ and nth order functions. Most of the methods in the stochastic signal analysis assume stationary signals. The best example for a stochastic non-stationary signal is human speech. For non-stationary signals, specific processing methods are needed, but if the time evolution is slower than the rate of the change of the frequency content, then the signal could be considered as stationary in an specified range. A related quantity is the *central second order moment function* or *autocovariance function* where the mean of the signal is subtracted before taking the expectation

$$c_{xx}(t1;t2) = \mathbb{E}[(X(t_1) - \mathbb{E}[X(t_1)])(X(t_2) - \mathbb{E}[X(t_2)])] \tag{A.1.77}$$

Power spectral density (**PSD**) describes how the signal power of a signal is distributed in frequency domain. In section A.1.2 we saw that that the power spectrum of a periodic signal can be obtained by plotting the $|c_k|^2$ coefficients versus frequency. If a signal has a continuous frequency spectrum it is more convenient to talk about power spectral density. According to the WIENER–KHINCHIN theorem, the PSD can be obtained by taking the FOURIER transform of the autocorrelation function.

$$S_{XX}(\omega) = \int_{-\infty}^{\infty} r_{XX}(\tau)\mathrm{e}^{-i\omega\tau}\,d\tau \tag{A.1.78}$$

The FOURIER transform of the autocovariance function, $C_{xx}(\omega)$, is sometimes called the

[9] Also called a *strict-sense stationary process*

Spectrum in some literature, which is clearly equal to the PSD of a signal if the signal is zero mean.

A.1.4 Electrical resonators

RLC circuits are linear harmonic oscillator circuits which are also known as *electrical resonators* (see figure A.3), with quantities such as charge, current or voltage as system observables and inductors and capacitors as energy storage elements. Capacitors and inductors store energy in their electric and magnetic fields respectively whereas a resistor models all dissipations in the system and acts as damper. The dissipated energy is radiated away from the circuit in form of heat. The current that flows through the circuit elements R, L and C causes a voltage drop across them. Current and voltage are related by the following equations

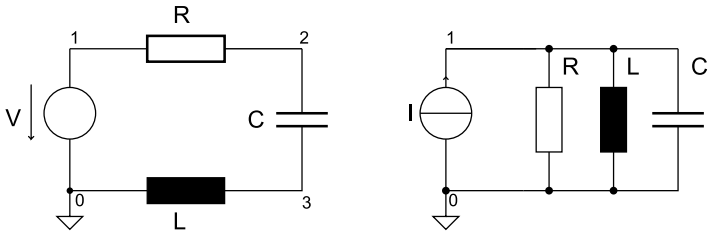

(a) (b)

Figure A.3: The RLC circuit in series (left) and parallel (right) configuration.

$$u(t) = R\,i(t) \qquad \text{or} \qquad i(t) = \frac{u(t)}{R} \tag{A.1.79}$$

$$u(t) = L\frac{di(t)}{dt} \qquad \text{or} \qquad i(t) = \frac{1}{L}\int_{t_0}^{t} u(\tau)\,d\tau + i(t_0) \tag{A.1.80}$$

$$u(t) = \frac{q(t)}{C} = \frac{1}{C}\int_{t_0}^{t} i(\tau)\,d\tau + u(t_0) \qquad \text{or} \qquad i(t) = C\frac{du(t)}{dt} \tag{A.1.81}$$

Using KIRCHHOFF's voltage law for the series RLC circuit in figure A.3(a) and assuming that the capacitor was not charged at $t = 0$, we have:

$$i(t)R + L\frac{di(t)}{dt} + \frac{1}{C}\int_{0}^{t} i(\tau)\,d\tau = u(t) \tag{A.1.82}$$

and using KIRCHHOFF's current law for the parallel RLC circuit in figure A.3(b) and assuming that at the current was switched on at $t = 0$, we have:

$$\frac{u(t)}{R} + C\frac{du(t)}{dt} + \frac{1}{L}\int_0^t u(\tau)\,d\tau = i(t) \tag{A.1.83}$$

If both sides of equation A.1.82 are divided by L, or both sides of equation A.1.83 for the parallel circuit is divided by C, then we obtain a coefficient which is denoted as ω_0^2, where

$$\omega_0 = \sqrt{\frac{1}{LC}} = \frac{1}{L}\sqrt{\frac{L}{C}} = \frac{1}{C}\sqrt{\frac{C}{L}} \tag{A.1.84}$$

which is known as the *fundamental angular resonance frequency* of the RLC circuit. The other resulting coefficient is different for series or parallel circuit and is called *damping constant* and is usually denoted as 2γ

$$\begin{aligned} 2\gamma &= \frac{R}{L} \quad \text{, for series circuit} \\ 2\gamma &= \frac{1}{RC} \quad \text{, for parallel circuit} \end{aligned} \tag{A.1.85}$$

It is measured in units of NEPERS per second [Np/s][10]. The damping constant causes the oscillatory motion to decrease in amplitude and settle the voltage or current to zero. A useful quantity often seen in the literature is known as *damping factor* which is dimensionless is defined as

$$\zeta = \frac{\gamma}{\omega_0} \tag{A.1.86}$$

Unloaded Q Value

It was mentioned that all power dissipations in the RLC circuit is modelled by the resistor. An ideal LC circuit can be obtained if R vanishes in the series RLC circuit of figure A.3(a) or if it grows to infinity for the parallel RLC circuit of figure A.3(b). So R is the element that dissipates energy out of the circuit and so reduces the *quality* of energy storage in the circuit. A consequence is the *Q value* or *Q factor* which is the a figure of merit for a resonant circuits. It is a measure of how much of the stored energy in the oscillator is lost due to dissipation of energy by the resistor in the electric circuit or by friction in the mechanical example. Thus the ideal LC oscillator would have an infinitely large Q value. It is defined as the ratio of the time averaged stored energy in the circuit in JOULES to the energy loss

[10] Np is not a SI unit, like dB it is a logarithmic unit of ratios. $\text{Np} = 20\log_{10} e$ dB

per second. The latter is also called the power loss P_L in units of WATTS $[W]$.

$$Q = 2\pi \frac{\text{Energy stored}}{\text{Energy lost per cycle}} = \omega_0 \frac{W}{P_L} = \omega_0 \frac{W}{\frac{-dW}{dt}} \tag{A.1.87}$$

In the above equation W is the stored energy in the system. At any given time the energy in system is either fully stored in the magnetic field or fully stored in the electric field or is shared between them. The energy stored in the magnetic field of the inductor and the electric field of the capacitor are [Wan11]:

$$\begin{aligned} W_L &= \int_0^{T_0} u(t) i(t)\, d\tau = \int_0^{T_0} L \frac{di(t)}{dt} i(t)\, d\tau \\ &= L \int_0^{I_{peak}} i(t)\, di(t) = \frac{1}{2} L I_{peak}^2 = L I_{rms}^2 \end{aligned} \tag{A.1.88}$$

$$\begin{aligned} W_C &= \int_0^{T_0} u(t) i(t)\, d\tau = \int_0^{T_0} C u(t) \frac{du(t)}{dt}\, d\tau \\ &= C \int_0^{U_{peak}} u(t)\, du(t) = \frac{1}{2} C U_{peak}^2 = C U_{rms}^2 \end{aligned} \tag{A.1.89}$$

where the *rms* value is equal to the peak value divided by $\sqrt{2}$ for sinusoidal signals (see section A.1.2). At the resonance frequency we have $W_L = W_C$, since:

$$W_{L,r} = L I_{rms}^2 = L \left| \frac{U_{rms}}{(i\omega_0 L)} \right|^2 = L \frac{U_{rms}^2 LC}{L^2} = C U_{rms}^2 = W_{C,r} \tag{A.1.90}$$

where the index r is added to emphasize the resonance condition. These relations are summarized again in the following equation:

$$W = W_L + W_C = \begin{cases} W_{L,max} + 0 = \frac{1}{2} L I_{peak}^2 \\ 0 + W_{C,max} = \frac{1}{2} C U_{peak}^2 \\ W_{L,r} + W_{C,r} = 2W_{L,r} = 2W_{C,r} = W_{L,max} = W_{C,max} \end{cases} \tag{A.1.91}$$

In the above equation, zero means that there is no contribution of that kind. For the calculation of the W_R which is the lost energy, one should be aware of the circuit topology and find out which quantity is constant among all participants of the circuit. In the series RLC circuit the current is the same through all elements whereas in the parallel RLC circuit

the voltage is the same. So we can take either I_{rms} or I_{peak} in the series circuit for the calculation of W_R and either U_{rms} or U_{peak} for the parallel RLC circuit and we should be consistent with our choice of voltage and current in W_L and W_C in equation A.1.90. So in the series circuit[11]

$$W_R = \int_0^{T_0} u(t)i(t)dt = I_{rms}^2 R T_0 \tag{A.1.92}$$

And in the parallel circuit:

$$W_R = \int_0^{T_0} u(t)i(t)dt = \frac{U_{rms}}{R} T_0 \tag{A.1.93}$$

The Q value of equation A.1.87 for the series and parallel RLC circuits are:

$$Q_s = 2\pi \frac{W_L}{\frac{P_L}{T_0}} = 2\pi \frac{W_L}{W_R} = 2\pi \frac{L I_{rms}^2}{I_{rms}^2 R T_0} = \frac{\omega_0 L}{R} = \frac{1}{R}\sqrt{\frac{L}{C}} = \frac{1}{\omega_0 RC} \tag{A.1.94a}$$

$$Q_p = 2\pi \frac{W_C}{W_R} = 2\pi \frac{C U_{rms}^2}{\frac{U_{rms}^2}{R} T_0} = \omega_0 RC = R\sqrt{\frac{C}{L}} = \frac{R}{\omega_0 L} \tag{A.1.94b}$$

It is now obvious that the Q value for the series circuit is proportional to the inverse of the resistance while it is directly proportional to the resistance for the parallel circuit. Finally, the Q value is related to damping constant and damping factor in the following way

$$\gamma = \frac{\omega_0}{2Q} \tag{A.1.95a}$$

$$\zeta = \frac{1}{2Q} \tag{A.1.95b}$$

Impedances

In the equations A.1.82 and A.1.83 one can see that there is a relationship between the current and voltage. The ratio of voltage to current is called *impedance* and its reciprocal is called *admittance*. Impedance and admittance are defined in frequency domain. But no matter if time domain or frequency domain representation is chosen, this physical phenomenon is responsible for power loss within the network. The time domain represen-

[11] Please refer to section A.1.2 as well.

tation of impedance is not practical for calculations. We will encounter the time domain representation in section 2.1.1.

Eequations A.1.82 and A.1.83 can be solved using the LAPLACE transform method (see e.g. [BC09]). The alternative approach is to LAPLACE transform the individual circuit components in equation A.1.81 and build the network afterwards in the LAPLACE domain. In the limit where the complex frequency in the LAPLACE domain is pure imaginary ($s \to i\omega$ the equations for impedance can be obtained.

Another easy method is to use the so called *phasor* notation. Assuming that the real input and output signals have the form

$$u(t) = U_p \cos(\omega t + \theta_u) \tag{A.1.96a}$$

$$i(t) = I_p \cos(\omega t + \theta_i) \tag{A.1.96b}$$

two conceptual signals are built that have the form

$$u(t) = U_p e^{i(\omega t + \theta_u)} = \underline{U_p} e^{i\omega t} \tag{A.1.97a}$$

$$i(t) = I_p e^{i(\omega t + \theta_i)} = \underline{I_p} e^{i\omega t} \tag{A.1.97b}$$

where $\underline{U_p} = U_p e^{i\theta_u}$ and $\underline{I_p} = I_p e^{i\theta_i}$ are the voltage and current phasors. Putting these conceptual time signals directly into the equations A.1.82 and A.1.83 and cancelling out will also result in the impedances of the series and parallel circuit. The impedances are:

$$Z_s = R + i\omega L + \frac{1}{i\omega C} = R(1 + iQ(\delta\omega)) \tag{A.1.98a}$$

$$Z_p(\omega) = \frac{1}{\frac{1}{R} + i\omega C + \frac{1}{i\omega L}} = \frac{R}{1 + iQ(\delta\omega)} \tag{A.1.98b}$$

where

$$\delta\omega = \frac{\omega}{\omega_0} - \frac{\omega_0}{\omega} \tag{A.1.99}$$

is known as the *detuning factor*. Here the definitions in equation A.1.94 were also used.

These complex impedances can be written in CARTESIAN or polar form

$$Z_s = R + iRQ(\delta\omega) = \left(R\sqrt{1+Q^2(\delta\omega)^2}\right)\exp\left[i\arctan(Q\delta\omega)\right] \tag{A.1.100a}$$

$$Z_p = \frac{R}{1+Q^2(\delta\omega)^2} - i\frac{RQ(\delta\omega)}{1+Q^2(\delta\omega)^2} = \left(\frac{R}{\sqrt{1+Q^2(\delta\omega)^2}}\right)\exp\left[-i\arctan(Q\delta\omega)\right] \tag{A.1.100b}$$

It is immediately possible to recognize that both complex impedances become real i.e. $Z = R$ whenever $\omega = \omega_0$. This is the point where the RLC system is said to be working in *resonance*. Beyond this point, the magnitude $|Z_s(\omega)|$ grows as ω approaches zero or infinity, whereas $|Z_p(\omega)|$ vanishes for these values of ω.

Transfer function

The voltage drop across the resistor in the series circuit and the current that goes through it in the parallel circuit can be determined using the voltage divider and current divider concept from basic circuit theory. The voltage divider law states

$$\frac{U_{part}}{U_{total}} = \frac{Z_{part}}{Z_{total}}$$

and the current divider law states that

$$\frac{i_{part}}{i_{total}} = \frac{Y_{part}}{Y_{total}}$$

Using these two we can find out the ratio of the output to input for the series circuit, i.e. u_R/u for the series circuit and i_R/i for the parallel circuit. This ratio is called the *transfer function* of the system which is dimensionless. After solving for the above mentioned ratio again using the LAPLACE transformed version of the equation A.1.81 and using proper substitutions from equation A.1.94 one obtains the **same** transfer function for **both** circuits.

$$H(\omega) = \frac{\omega_0\omega}{\omega_0\omega + i\omega^2 Q - i\omega_0^2 Q} = \frac{1}{1 - iQ(\delta\omega)} \tag{A.1.101}$$

The form in the middle is sometimes called the *canonical form* in the literature. The transfer function in the CARTESIAN and polar form is:

$$H(\omega) = \frac{1}{1+Q^2(\delta\omega)^2} + \frac{iQ(\delta\omega)}{1+Q^2(\delta\omega)^2} = \frac{1}{\sqrt{1+Q^2(\delta\omega)^2}} \exp\left[\arctan(Q(\delta\omega))\right] \quad \text{(A.1.102)}$$

By comparing this with the impedances in equation A.1.100 we find out

$$H(\omega) = R/Z_s(\omega) \quad \text{(A.1.103a)}$$

$$H(\omega) = Z_p(\omega)/R \quad \text{(A.1.103b)}$$

A plot of the transfer function of a parallel RLC circuit with $f_0 = 243.95\ [MHz]$. $Q = 1130$ and $Q = 565$ is depicted in figure A.4. At frequencies where $\angle Z_{s,p} = \pm\frac{\pi}{4}$ we have

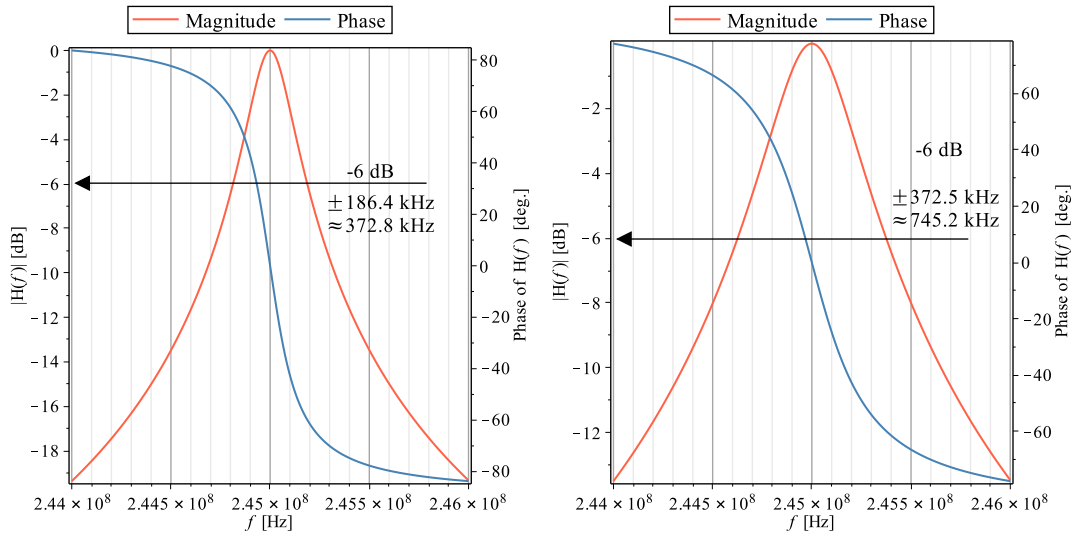

Figure A.4: Transfer function for $f_0 = 243.95\ [MHz]$. $Q = 1130$ (left) and $Q = 565$ (right).

$$\tan\frac{\pi}{4} = Q_{s,p}\left(\frac{\omega_c}{\omega_0} - \frac{\omega_0}{\omega_c}\right) = \pm 1 \quad \text{(A.1.104)}$$

which results in

$$|Z_s(\omega)| = R\sqrt{2} \quad \text{(A.1.105a)}$$

$$|Z_p(\omega)| = \frac{R}{\sqrt{2}} \quad \text{(A.1.105b)}$$

ω_c is called the *cut-off frequency* of the filter. In the power log scale, the desired point is

$-3\ [dB]$ and in the voltage log scale $-6\ [dB]$ lower than maximum. Following equation A.1.104 we have

$$Q_{s,p} = \frac{\omega_0 \omega_c}{\Delta\omega(\omega_c + \omega_0)} \approx \frac{\omega_0}{\mathrm{BW}} \tag{A.1.106}$$

for a high Q system ω_c is very close to ω_0 so we can safely assume $\omega_c + \omega_0 = 2\omega_c$. $BW = 2\Delta\omega$ is the bandwidth of the RLC filter and

$$\Delta\omega = \begin{cases} \omega_c - \omega_0 & , \omega_c > \omega_0 \\ \omega_0 - \omega_c & , \omega_0 > \omega_c \end{cases}$$

This definition of Q value is used to in practical measurement of high Q systems where the impedance curve is not deformed by other factors, such as coupling loops. The value of band width is also depicted in figure A.4 at $-6dB$ and $\pi/4$. The approximation A.1.106 is not suitable in this case.

Steady state output response

If the right hand sides of the equations A.1.82 and A.1.83 are set to zero, they form homogeneous differential equations. Their solutions show the behaviour of the undriven RLC circuit. The current needed must come from a capacitor that has been charged prior to the insertion into the circuit. A plot of these undriven solutions are depicted at the top rows of figures A.5 and A.6 on pages 138 and 139.

Instead, if these equations are driven periodically using input sources shown in equation A.1.96, after a transitory time and a sufficiently long time, the RLC circuit will finally oscillate at the drive frequency. The quality of this oscillation depends on the Q of the RLC circuit (i.e. on the damping factor/constant) and the frequency of drive and if it is close the the resonance or the RLC or not.

For the parallel circuit in figure A.3(b) and using the polar form of the impedance in equation A.1.100 and using complex multiplication of the conceptual signal A.1.97 and then going back to the real signal A.1.96 we have

$$u(t) = \frac{RI_p}{\sqrt{1 + Q^2(\delta\omega)^2}} \cos\left[\omega t - \arctan\left(\frac{Q\delta\omega\cos(\theta_i) - \sin(\theta_i)}{\cos(\theta_i) + Q(\delta\omega)\sin(\theta_i)}\right)\right] \tag{A.1.107}$$

where we can identify $\frac{RI_p}{\sqrt{1+Q^2(\delta\omega)^2}}$ as the peak output voltage $U_{p,out}$ where as the peak input voltage into the system $U_{p,in}$ is only RI_p. The phase reduces to those of equation A.1.100 in case $\theta_i = 0$. The same results can be achieved using the transfer function of the RLC circuit where for the real input current in equation A.1.96, we get an output current

$$i_{out} = |H(\omega)|I_p \cos(\omega t + \theta_i + \angle H(\omega)) \tag{A.1.108}$$

which we can use to calculate the output voltage.

In order to better visualise these relations, in dynamical analysis it is customary to recognize different *states* of a system. In the equations of the RLC circuit the observable and its first derivative are the *state variables*. In figure A.5 different solutions are solved numerically and plotted for the undamped case where closed orbits in the state space plot (also known as *limit cycles*) show oscillations. The second time series and state space plot shows a distorted pattern since it belongs to the case where the drive frequency is off the resonance frequency.

Once given an initial condition, the undriven undamped oscillator runs for ever. The state space curve shows no dispersion. If it is driven on its resonance frequency, then the amplitude of oscillation will grow to infinity. The state space plot also spirals out as its radius grows for ever. The plots in figure A.6 show the damped case for different damping factors ζ where ω_0 is either four times larger, equal to or one fourth of γ. These show that unlike the undamped case, in a damped system a transitory behaviour exists whose duration is related to the strength of power dissipation. In any case, the system oscillates with the drive frequency after a sufficiently long time. But it can be seen from the figure that the transitory oscillations vanish more quickly and the system oscillates with large amplitudes whenever the oscillator is operated on resonance. For a resonant pickup intended for few or single particle detection, this is the desired operation mode.

Using equations A.1.95a and A.1.95b we see that for almost all practical cases a resonator with moderate or high Q will always satisfy the condition of under-damped oscillation as shown in plots of figure A.6.

Steady state output power

From equation A.1.72 we know the relation for the average power. For this, we use the relation in the equation A.1.107

$$\langle P \rangle = \frac{1}{2R} U_{peak}^2 = \frac{1}{2R} U_{p,out}^2 = \frac{1}{2R} \left(\frac{R I_p}{\sqrt{1 + Q^2 (\delta\omega)^2}} \right)^2 \tag{A.1.109}$$

Same result can be obtained using the transfer function (cf. equation A.1.108). On the condition of resonance, this reduces to

$$\langle P \rangle = \frac{1}{2} R I_p^2 \tag{A.1.110}$$

Loaded Q value

So far there was no other elements in our resonance system other than the ideal L and C, a dissipating R and the source. If the circuit is connected to an external circuit, the impedance Z_l of that circuit will *load* the RLC circuit, so that the new Q will be smaller. Again if all dissipations of the external circuit can be modelled with a resistor R_l, then this resistor will be in parallel with the internal R of the RLC. Such a circuit is shown in figure A.7. This results in the *loaded Q value* Q_{loaded}[12] [Col00]:

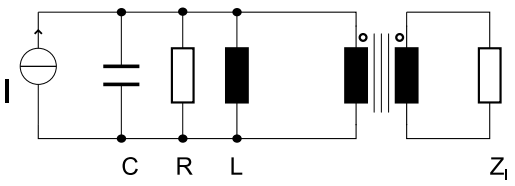

Figure A.7: A loaded RLC circuit.

$$Q_{loaded} = \frac{R R_l / (R + R_l)}{\omega_0 L} \tag{A.1.111}$$

Hypothetically removing R from the circuit and leaving only R_l leads to the *external Q value*.

$$Q_{ext} = \frac{R_l}{\omega_0 L} \tag{A.1.112}$$

The relationship between these are:

$$\frac{1}{Q_{loaded}} = \frac{1}{Q_{ext}} + \frac{1}{Q} \tag{A.1.113}$$

[12] Throughout this work Q is used as unloaded Q value.

Coupling factor

The coupling factor is a measure for the coupling of the RLC to the external circuit and is defined as:

$$k = \frac{Q}{Q_{ext}} = \frac{P_{L,ext}}{P_L} \tag{A.1.114}$$

In the second relation $P_{L,ext}$ is the dissipated power in the external circuit. Three cases can be differentiated where the system is either *loosly(weakly) coupled*, *critically coupled* or *over coupled* for values of $k < 1$, $k = 1$ or $k > 1$ respectively. Generally, for maximum power transfer between RLC and external circuit, the coupling factor must be as close as possible to unity (critically coupled). In a cavity this can be achieved by mechanical fine tuning the coupling loop or antenna.

Characteristic impedance R/Q

For the **parallel circuit**, the ratio R/Q is called the *characteristic impedance*.

$$\frac{R}{Q} = \sqrt{\frac{L}{C}} = \omega_0 L = \frac{1}{\omega_0 C} \tag{A.1.115}$$

It is important to note that this ratio does not depend on the R itself. It is a measure that describes the system regardless of its lossy behaviour. As we will see, for cavities, this ratio depends only on the geometry.

Equivalent circuit of cavities and power coupling

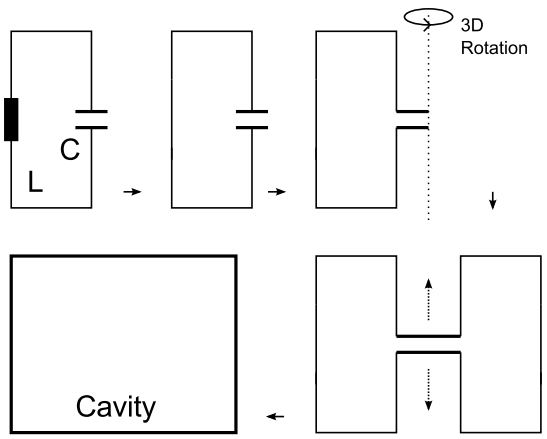

Figure A.8: Evolution of a an ideal LC circuit to a hollow cavity.

Every mode in an ideal cavity resembles an RLC resonator. A common way to illustrate this in the literature (see e.g. [Che89]) is to first imagine an ideal LC circuit. Start by unwinding the inductor L, then rotate to make a surface of revolution to form a cavity, or the other way round. This is shown in figure A.8. A real cavity is equivalent to infinitely many damped parallel RLC circuit due to the losses in the cavity. Whenever a cavity is excited, currents oscillate through

the walls. At the resonance cavity behaves like a real valued ohmic resistance, the so called *shunt impedance* . Shunt impedance will be discussed in chapter 2.1.2. The parameter that changes R is the surface conductivity of the cavity material. The distance d is responsible parameter for the capacitance C. By letting the beam pipe to penetrate into the cavity from either or both sides, d can be reduced so that higher values of C can be achieved. Since the whole cavity surface acts as one single turn of wire in an inductor, the only way to increase L is to build a larger cavity.

A.1.5 Relations and identities

Autocorrelation of the Schottky noise process

In the reference [Cha84] it is shown that the autocorrelation function of the SCHOTTKY process can be calculated using trigonometric manipulations. Here these manipulations are shown. The first thing that is needed is the decomposition of the cosine term

$$
\begin{aligned}
&\cos\left(m\omega_j(t+\tau)+m\Theta_j\right)\cos\left(n\omega_k t+n\Theta_k\right)=\\
&\frac{1}{2}\cos\left(-m\omega_j(t+\tau)-m\Theta_j+n\omega_k t+n\Theta_k\right)\\
&+\frac{1}{2}\cos\left(m\omega_j(t+\tau)+m\Theta_j+n\omega_k t+n\Theta_k\right)\\
&=\frac{1}{4}\mathrm{e}^{i\left(-m\omega_j(t+\tau)-m\Theta_j+n\omega_k t+n\Theta_k\right)}\\
&+\frac{1}{4}\mathrm{e}^{-i\left(-m\omega_j(t+\tau)-m\Theta_j+n\omega_k t+n\Theta_k\right)}\\
&+\frac{1}{4}\mathrm{e}^{i\left(m\omega_j(t+\tau)+m\Theta_j+n\omega_k t+n\Theta_k\right)}\\
&+\frac{1}{4}\mathrm{e}^{-i\left(m\omega_j(t+\tau)+m\Theta_j+n\omega_k t+n\Theta_k\right)}\\
&=\frac{1}{4}\frac{\mathrm{e}^{in\omega_k t}\mathrm{e}^{in\Theta_k}}{\mathrm{e}^{im\omega_j(t+\tau)}\mathrm{e}^{im\Theta_j}}\\
&+\frac{1}{4}\frac{\mathrm{e}^{im\omega_j(t+\tau)}\mathrm{e}^{im\Theta_j}}{\mathrm{e}^{in\omega_k t}\mathrm{e}^{in\Theta_k}}\\
&+\frac{1}{4}\mathrm{e}^{im\omega_j(t+\tau)}\mathrm{e}^{im\Theta_j}\mathrm{e}^{in\omega_k t}\mathrm{e}^{in\Theta_k}\\
&+\frac{1}{4}\frac{1}{\mathrm{e}^{im\omega_j(t+\tau)}\mathrm{e}^{im\Theta_j}\mathrm{e}^{in\omega_k t}\mathrm{e}^{in\Theta_k}}
\end{aligned}
\tag{A.1.116}
$$

Each of the exponential terms can be rewritten in the following form [Cha84]

$$e^{-i\left(m\Theta_j - n\Theta_k\right)} = e^{-\frac{1}{2}i(m+n)(\Theta_j-\Theta_k)}\, e^{-\frac{1}{2}i(m-n)(\Theta_j+\Theta_k)} \tag{A.1.117}$$

$$e^{i\left(m\Theta_j - n\Theta_k\right)} = e^{\frac{1}{2}i(m+n)(\Theta_j-\Theta_k)}\, e^{\frac{1}{2}i(m-n)(\Theta_j+\Theta_k)} \tag{A.1.118}$$

$$e^{-i\left(m\Theta_j + n\Theta_k\right)} = e^{-\frac{1}{2}i(m+n)(\Theta_j+\Theta_k)}\, e^{-\frac{1}{2}i(m-n)(\Theta_j-\Theta_k)} \tag{A.1.119}$$

$$e^{i\left(m\Theta_j + n\Theta_k\right)} = e^{\frac{1}{2}i(m+n)(\Theta_j+\Theta_k)}\, e^{\frac{1}{2}i(m-n)(\Theta_j-\Theta_k)} \tag{A.1.120}$$

$$\tag{A.1.121}$$

This enables us the following discussion: The expectation or averaging inside the autocorrelation causes the terms with $\Theta_j + \Theta_k$ to reduce to $\delta_{j,k}$. The terms with $\Theta_j - \Theta_k$ will oscillate to zero for all $j \neq k$. Only for the case of $j = k$ so that due to averaging the above equations reduce to

$$e^{-i\left(m\Theta_j - n\Theta_k\right)} = 1 \tag{A.1.122}$$

$$e^{i\left(m\Theta_j - n\Theta_k\right)} = 1 \tag{A.1.123}$$

$$e^{-i\left(m\Theta_j + n\Theta_k\right)} = 0 \tag{A.1.124}$$

$$e^{i\left(m\Theta_j + n\Theta_k\right)} = 0 \tag{A.1.125}$$

These can be then inserted in the original autocorrelation equation.

Used identities

Used FOURIER transform identities

$$x(t - t_0) \longleftrightarrow e^{-i\omega_0 t} X(\omega) \tag{A.1.126}$$

$$\sum_{m=-\infty}^{\infty} \delta(t - mT_0) \longleftrightarrow \omega_0 \sum_{m=-\infty}^{\infty} \delta(\omega - m\omega_0) \tag{A.1.127}$$

$$\frac{1}{\sigma\sqrt{2\pi}} \exp\left[-\frac{t^2}{2\sigma^2}\right] \longleftrightarrow \exp\left[-\frac{\omega^2\sigma^2}{2}\right] \tag{A.1.128}$$

The relationship between truncation in time and frequency resolution can be seen in the FOURIER transform of the rectangular window function, which shows that the signal has

been turned on for the duration of T_{on}

$$\text{rect}(t) = \begin{cases} A & : -T_{on}/2 < t \leq T_{on}/2 \\ 0 & : \text{otherwise} \end{cases} \quad \leftrightarrow AT_{on} \frac{\sin\left(\frac{\omega}{2}T_{on}\right)}{\frac{\omega}{2}T_{on}} = AT_{on}\text{sinc}\left(\frac{\omega}{2}T_{on}\right) \tag{A.1.129}$$

where this results in the unnormalised sinc function. This equation is similar to equation 2.2.35, but that one is written for discrete times. A plot is depicted in figure A.9. The zeros of the unnormalised sinc funcitons are non-zero integer multiples of π apart from each other. For the first zero crossing we have

$$\omega = \frac{2\pi}{T_{on}} = f = \frac{1}{T_{on}} \rightarrow \Delta f = \frac{2}{T_{on}} \tag{A.1.130}$$

This equation shows the relation between the length of the time window and a width of the frequency band.

Vector calculus identities in cylindrical coordinates (r, φ, z) for the vector $\vec{A} = A_r\vec{e_r} + A_\varphi\vec{e_\varphi} + A_z\vec{e_z}$ adapted from [Jac98] on the side cover

$$\vec{\nabla}\psi = \frac{\partial\psi}{\partial r}\vec{e_r} + \frac{1}{r}\frac{\partial\psi}{\partial\varphi}\vec{e_\varphi} + \frac{\partial\psi}{\partial z}\vec{e_z} \tag{A.1.131}$$

$$\vec{\nabla}\cdot\vec{A} = \frac{1}{r}\frac{\partial}{\partial r}(rA_r) + \frac{1}{r}\frac{\partial A_\varphi}{\partial\varphi} + \frac{\partial A_z}{\partial z} \tag{A.1.132}$$

$$\vec{\nabla}\times\vec{A} = \left(\frac{1}{r}\frac{\partial A_z}{\partial\varphi} - \frac{\partial A_\varphi}{\partial z}\right)\vec{e_r} + \left(\frac{\partial A_r}{\partial z} - \frac{\partial A_z}{\partial r}\right)\vec{e_\varphi} + \frac{1}{r}\left(\frac{\partial}{\partial r}(rA_\varphi) - \frac{\partial A_r}{\partial\varphi}\right)\vec{e_z} \tag{A.1.133}$$

$$\vec{\nabla}^2\psi = \frac{1}{r}\frac{\partial}{\partial r}\left(r\frac{\partial\psi}{\partial r}\right) + \frac{1}{r^2}\frac{\partial^2\psi}{\partial\varphi^2} + \frac{\partial^2\psi}{\partial z^2} \tag{A.1.134}$$

The derivative of Bessel function of first kind:

$$\frac{d}{dr}J_m(ar) = a\left(\frac{m}{ar}J_m(ar) - J_{m+1}(ar)\right) = a\frac{d}{d(ar)}J_m(ar) \tag{A.1.135}$$

where a is a constant. The following integral identities involving Bessel functions are needed for the calculation of the power loss and hence the Q value in a pillbox.

$$\int_0^\varrho r\,J_0^2\left(\frac{j_{01}}{\varrho}r\right)dr = \int_0^\varrho r\,J_1^2\left(\frac{j_{01}}{\varrho}r\right)dr = \frac{\varrho^2}{2}\,J_1^2(j_{01}) \tag{A.1.136}$$

A.2.1 Simulation settings

Boundary conditions

Solutions of electromagnetic problems can be simplified and performed faster using existing symmetries in the structure. Proper boundary conditions are needed to achieve correct results. Two of most frequently used boundary conditions are a perfect electric conductor (PEC) and a perfect magnetic conductor (PMC). According to equation A.1.24, at a PEC boundary only normal electric field and tangential (parallel) magnetic field components exist. The other two, i.e. parallel electric field and normal magnetic field components vanish. By contrast, at a PMC boundary, normal magnetic and parallel electric field components exist. The other two, i.e. parallel magnetic and normal electric field components vanish.

These options can be set in MWS® using the proper dialogue box, and in SUPERFISH using expressions for top, bottom, left and right side of the structure. In SUPERFISH a PEC is denoted as a DIRICHLET boundary and can be set with a value eqaul to 0. A PMC is a NEUMANN boundray in SUPERFISH and can be set with a value eqaul to 1 ([BY06], [Kra10]).

```
1 NBSLF= 1,     ; Left-side boundary condition
  NBSLO = 0,    ; Lower boundary condition
3 NBSRT  = 1,   ; Right-side boundary condition
  NBSUP = 1,    ; Upper boundary condition
```

Listing A.1: Example of setting boundary conditions in SUPERFISH

Table A.1 summarizes these options.

MWS®	SUPERFISH	Meaning
Electric (PEC)	DIRICHLET, value=0	$E_t = 0$, $H_n = 0$, $E_n \neq 0$, $H_t \neq 0$
Magnetic (PMC)	NEUMANN, value = 1	$E_t \neq 0$, $H_n \neq 0$, $E_n = 0$, $H_t = 0$

Table A.1: Summary of boundary conditions in SUPERFISH and MWS®

XY plane	electric $E_t = 0$
XZ plane	magnetic $H_t = 0$
YZ plane	magntic $H_t = 0$

Table A.2: Symmetry planes used in MWS for this work.

Symmetry planes

In standard mode SUPERFISH supports cylindrical symmetrical structures. This can be activated using the following line:

```
icylin=1,
```

Listing A.2: Activate cylindrical symmetry in SUPERFISH

In MWS, symmetry planes can be set in a dialogue box for in Cartesian coordinates. In order to simulate the structure in figure 2.4(a), where the pipe is extended in z direction, three symmetry planes can be used, so that only one eighth of the structure is simulated. The required configuration is listed in table A.2.

A.2.2 Circuit description

The circuit diagram is depicted in the next page. The low noise amplifier is of the type BNZ1034 model BZP102UB1. Figure A.10 shows the measured performance using a noise figure analyser ROHDE & SCHWARZ ZVA40 [Pes10]. Bandpass filters are used after the first and second amplification stages. A transistor circuit is used to control the RF switches that allow a third amplification stage. The control signal can either be controlled using the **ESR-MODI** or using **NODAL** in **VMS** system, where the resonant pickup has the nomenclature **E01DX_S**. Inside the program **fbsd**, the control circuit for the resonant pickup has the module number **3** and port number **19**. Then either bits can be set using *set data* or can be read out using *read data*. The power to the whole system can also be turned off using the control system. In the control system, the plungers have the following nomenclature: **EEXDR1IS** for the plunger which is located in the direction of the center of ESR, and **EEXDRAS** for the second one. They can have a value between **0** and **40,** where **0** is the minimum position and corresponds to the position closest to the center of the beam pipe. These can be set on the console directly, or by NODAL using the program **stepinfo**.

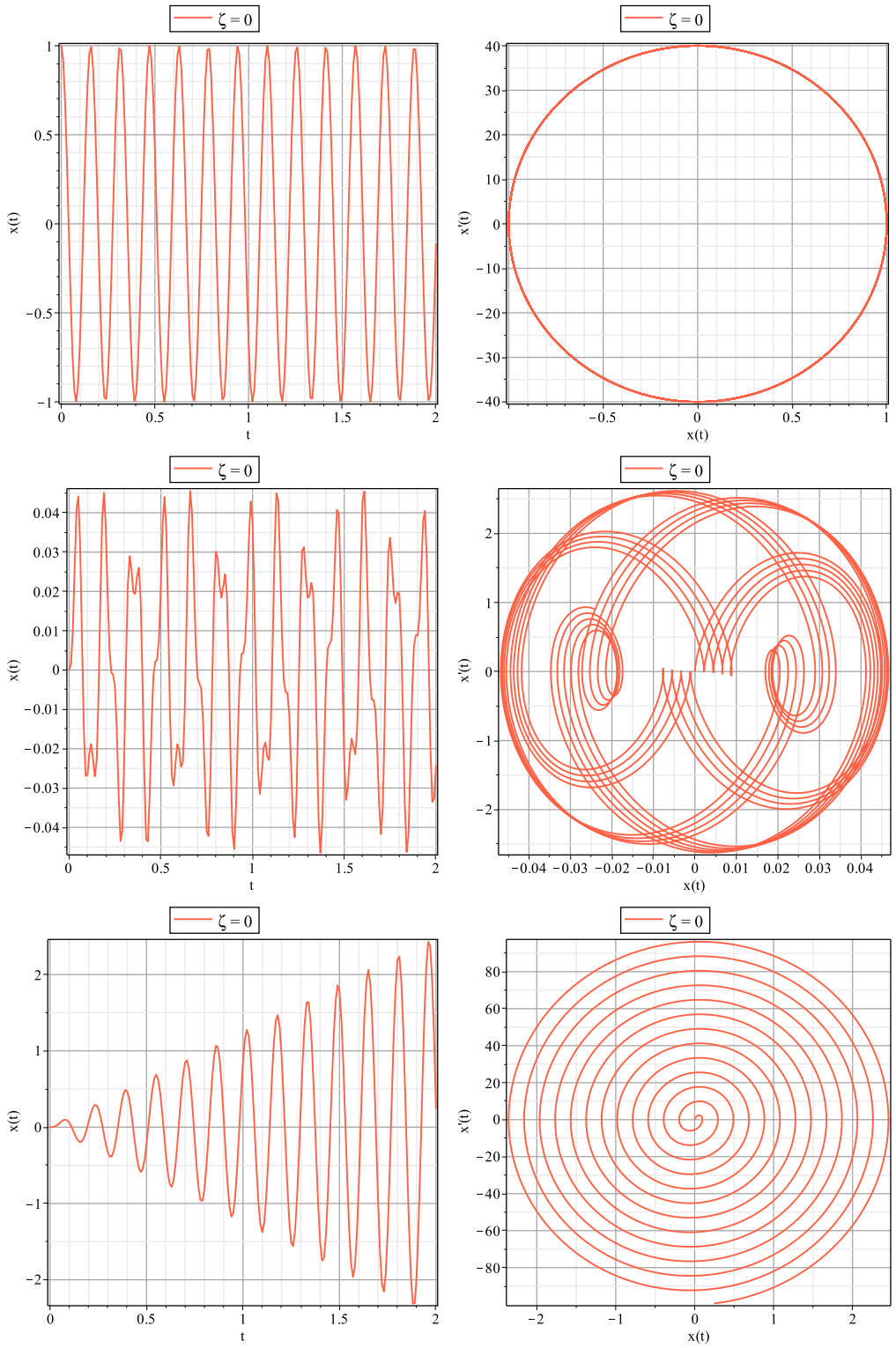

Figure A.5: Time series (left) and phase space plots (right) of undamped harmonic oscillator for undriven (top), driven off resonance (middle) and driven on resonance case for $\zeta = 0.25$, $\zeta = 1$ and $\zeta = 4$.

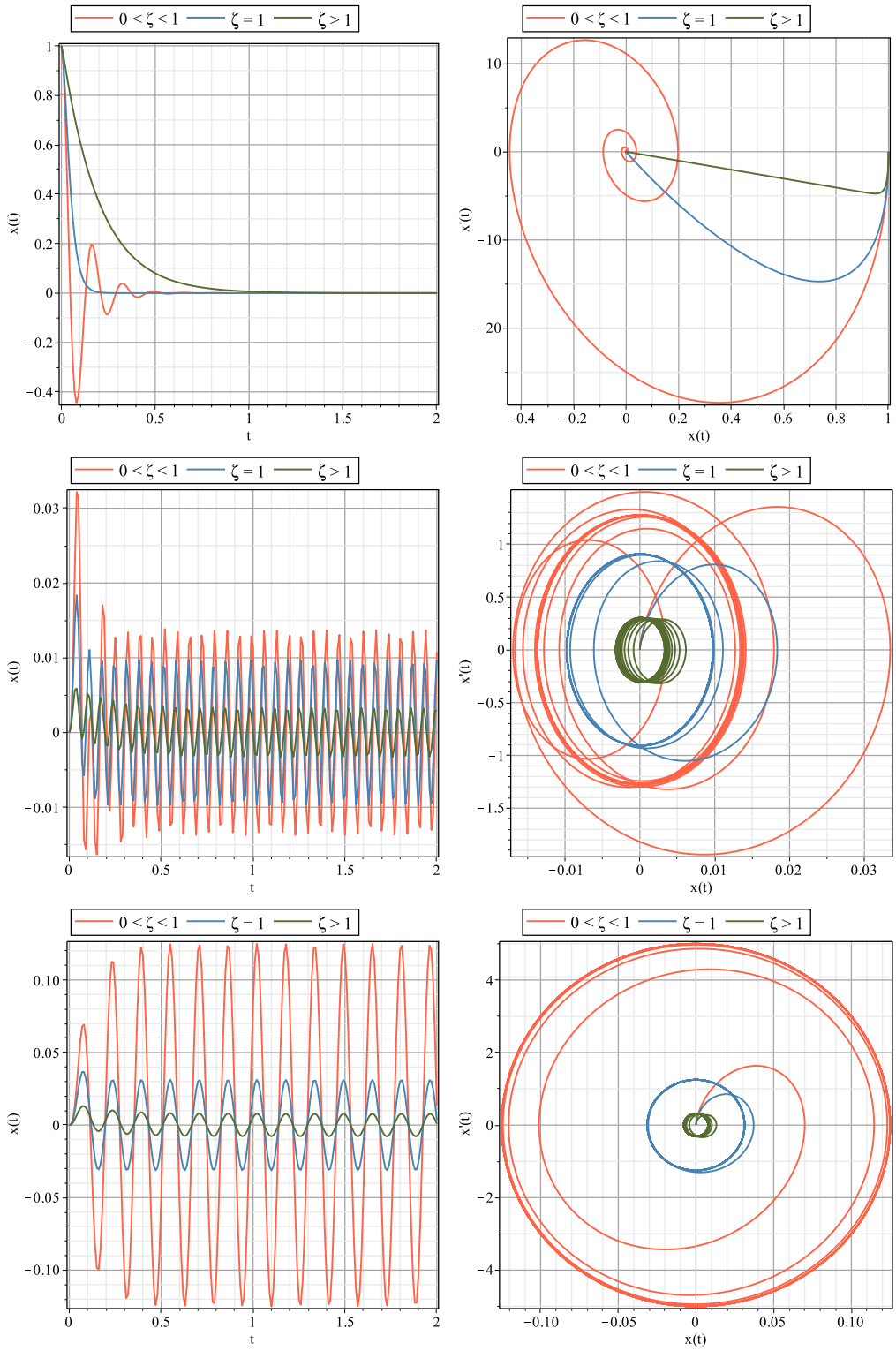

Figure A.6: Time series (left) and phase space plots (right) of damped harmonic oscillator for undriven (top), driven off resonance (middle) and driven on resonance case for different damping factors for $\zeta = 0.25$, $\zeta = 1$ and $\zeta = 4$.

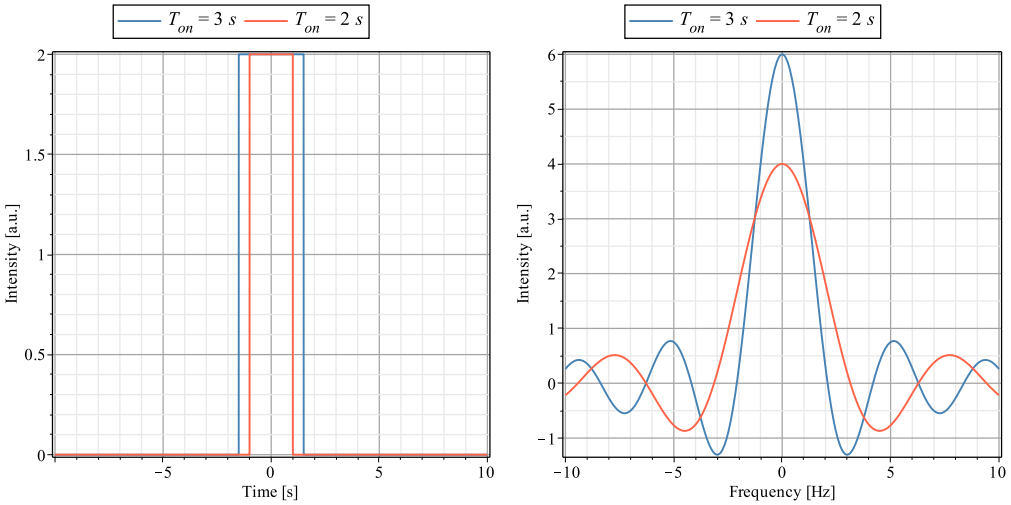

Figure A.9: Rectagular window and sinc function.

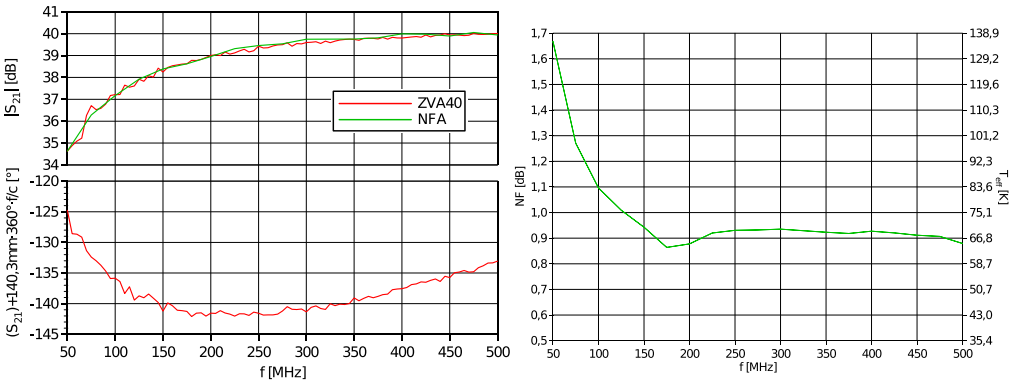

Figure A.10: Measurements on the LNA [Pes10].

Resonator Amplifier and Control

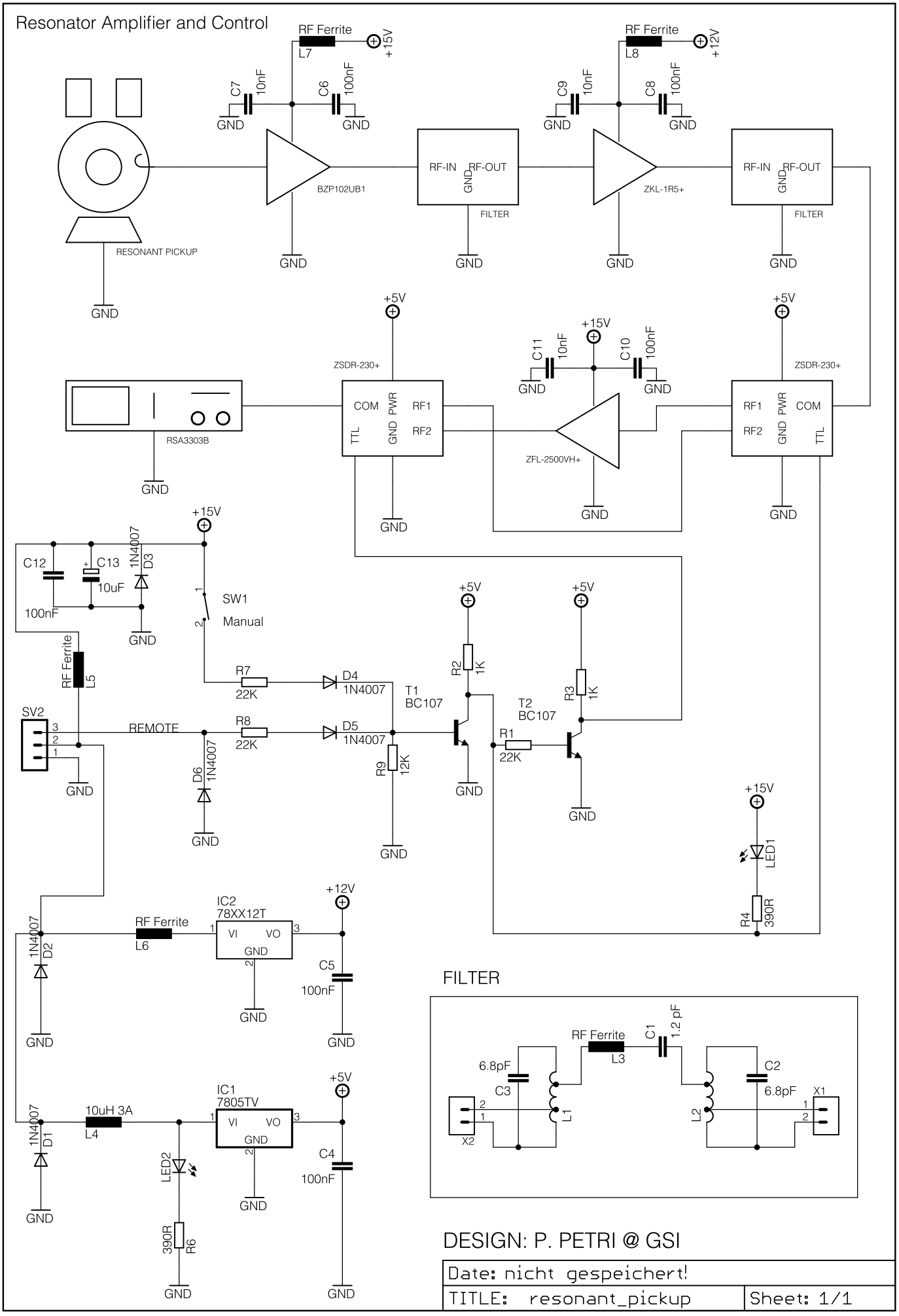

DESIGN: P. PETRI @ GSI

Date: nicht gespeichert!	
TITLE: resonant_pickup	Sheet: 1/1

List of Symbols, Figures and Tables

$\vec{a}$, $\vec{b}$	Vectors
a_i, b_i	Elements of vectors
A_i, A_s, A_1	Oscillation amplitudes
$\vec{A}$	Vector potential
$\vec{B}$	Magnetic flux density
BW	Band width
c_0, c_k	Complex Fourier coefficients
C	Capacitance
C', $C1$, $C2$	Constants
d	Depth of cavity
$\vec{D}$	Electric flux density (electric displacement) vector
$\vec{e_i}$, $e(x)$	Unit vectors
$\mathscr{E}$, W, ΔW	Energy and Work
$\vec{E}$	Electric field intensity vector
$E_{x,y,z,r,\varphi,z,t,n}$	Components of electric field
f , f_0, f_1, f_2, f_s, f_{rev}	Frequency

$\vec{F}$	Force
$f(x)$, $g(x)$, $h(x)$	Functions
$h(t)$	Impulse response in time domain
$H(\omega)$	Impulse response in frequency domain
$\vec{H}$	Magnetic field intensity
$H_{x,y,z,r,\varphi,z,t,n}$	Components of magnetic field
$i(t)$, $I(\omega)$, I_0	Electric current
i	Imaginary unit
j_{mn}	n^{th} zero of m^{th} of Bessel functions
J_m	m^{th} Bessel function
$\vec{J}$, $\vec{J}_s$	Current
k, κ	Loss parameter
$\vec{k}$, k_z, k_r	Wave vectors and its components
k	Wake loss factor (modal and overall)
L	Inductance
L_a, L_b and L_c	Elliptical integrals
m	Mode number
m	Mass
M	bead constant
n	Mode number
n	Discrete time
$\vec{n}$	normal vector
N	Number of points
N_m	m^{th} Neumann function

p	Mode number
P, P_L	Power, dissipated power
q, $q(t)$	Electric Charge
Q	Q value (Electromagnetic and Nuclear)
r	Radial distance in cylindrical coordinates
$\vec{r}$	Radial position vector
R, R_s, R_p, R_{sh}	Resistance
$\vec{s}$	Surface vector
t	Time
$t_{1/2}$	Half-life
T_0, T_s	Fundamental period
$u(t)$, $U(\omega)$, U, U_0	Electric voltage
$\vec{v}$	Speed
V, V_b, V_{rod} and dV	Volume, volume differential
$x(t)$, $y(t)$, $x[n]$, $y[n]$	Signals in time domain (Mechanical or Electrical)
$X(\omega)$, $Y(\omega)$, $X[k]$, $Y[k]$	Signals in frequency domain (Mechanical or Electrical)
Y_s	Series admittance
z	longitudinal distance in cylindrical coordinates
Z, Z_s, Z_p	Impedance
α, α_1, α_2	Constant, attenuation constant
β	Relativistic speed factor, phase constant
γ	Damping constant, propagation constant, relativistic factor
ε, ε_0, ε_r	Permittivity
ζ	Damping factor

η, η_0, η_r	Medium impedance
θ, ϑ	Angle
κ	coupling factor, discrete frequency
λ, λ_0	Wavelength
Λ	Transit time factor
μ, μ_0, μ_r	Permeability
ν	Sequential mode number
ρ	Charge density
ϱ	Radius
σ	Electric conductivity
τ	Integration variable for time
ϕ	Scalar potential
Φ	Magnetic flux
φ	Azimuthal distance in cylindrical coordinates
ψ	Constant
ω, ω_0, ω_c, ω_d	Angular frequency
Ω	Ohm (unit)

List of Figures

List of Tables

Bibliography

[B+74] J. Borer et al., *Non-destructive diagnostics of coasting beams with schottky noise*, 1974.

[B+96] F. Bosch et al., *Observation of bound-state beta- decay of fully ionized 187-re 187-os cosmochronometry*, Physical Review Letters **77** (1996), no. 26, 5190–5193.

[BC09] R. Bronson and G. Costa, *Schaum's outline of differential equations, 3ed*, 3 ed., McGraw-Hill, May 2009.

[Bet44] H. A. Bethe, *Theory of diffraction by small holes*, Physical Review **66** (1944), no. 7-8, 163–182.

[BL82] J. Bisognano and Ch. Leemann, *Stochastic cooling*, AIP Conference Proceedings **87** (1982), no. 1, 583–655.

[Bla06] K. Blaum, *High-accuracy mass spectrometry with stored ions*, Physics Reports **425** (2006), no. 1, 1–78.

[Bra00] C. Brandau, *Messungen zur Photorekombination hochgeladener lithiumähnlicher Ionen*, Ph.D. thesis, Justus-Liebig Universität Giessen, Gießen, 2000.

[Bry10] P. J. Bryant, *History and applications of accelerators i, II*, 2010.

[BS96] K. L.F Bane and M. Sands, *The short-range resistive wall wakefields*, AIP Conference Proceedings, 1996, p. 131–149.

[BY06] J. H. Billen and L. M. Young, *Poisson superfish handbook*, 2006.

[Car01] R. G Carter, *Accuracy of microwave cavity perturbation measurements*, IEEE Transactions on Microwave Theory and Techniques **49** (2001), no. 5, 918–923.

[Cas09] F. Caspers, *Schottky signals for longitudinal and transverse bunched-beam diagnostics*, 407–425.

[Cas10] ———, *RF engineering basic concepts: the smith chart*.

[CD85] F. Caspers and G. Dôme, *Precise perturbation measurements of resonant cavities and higher order mode identification*, Tech. report, CERN SPS/85-46, Geneva, Switzerland, 1985.

[Cha84] S. Chattopadhyay, *Some fundamental aspects of fluctuations and coherence in charged-particle beams in storage rings*, CERN, Geneva, 1984.

[Che89] D. K. Cheng, *Field and wave electromagnetics*, 2nd ed., Addison-Wesley, January 1989.

[Col00] R. E. Collin, *Foundations for microwave engineering*, 2 ed., Wiley-IEEE Press, December 2000.

[CW32] J. D. Cockcroft and E. T. S. Walton, *Experiments with high velocity positive ions. II. the disintegration of elements by high velocity protons*, Proceedings of the Royal Society of London. Series A **137** (1932), no. 831, 229 –242.

[D$^+$01] J. C Denard et al., *High accuracy beam current monitor system for CEBAF's experimental hall a*, Particle Accelerator Conference, 2001. PAC 2001. Proceedings of the 2001, vol. 3, 2001, p. 2326–2328.

[D$^+$06] H. Danared et al., *CRYRING machine studies for FLAIR*, this conference, 2006.

[Fal68] A. Faltens, *Radiation by a relativistic particle passing through a cavity*, 1968.

[Fet90] A. Fettweis, *Elemente nachrichtentechnischer Systeme*, Teubner Stuttgart, 1990.

[FFT11] FFTW, *FFTW home page*, http://www.fftw.org/, 2011.

[Fra85] B. Franzke, *Heavy ion storage rings for atomic physics*, Nuclear Science, IEEE Transactions on **32** (1985), no. 5, 3297–3301.

[Fra87] ———, *The heavy ion storage and cooler ring project ESR at GSI*, Nuclear Instruments and Methods in Physics Research Section B: Beam Interactions with Materials and Atoms **24-25** (1987), no. Part 1, 18–25.

[Fri44] H. T Friis, *Noise figures of radio receivers*, Proceedings of the IRE **32** (1944), no. 7, 419–422.

[G+87] D. A. Goldberg et al., *A high-frequency schottky detector for use in the tevatron*, Proc. 1987 USPAC (1987), 547.

[G+12] M. Grieser et al., *Storage ring at HIE-ISOLDE*, European Journal of Physics **207** (2012), 1–117.

[GL92] D. A. Goldberg and G. R. Lambertson, *Dynamic devices. a primer on pickups and kickers*, AIP Conference Proceedings **249** (1992), no. 1, 537–600.

[Gri99] D. J. Griffiths, *Introduction to electrodynamics*, 3 ed., Benjamin Cummings, January 1999.

[H+63] H. A. Haus et al., *Description of the noise performance of amplifiers and receiving systems*, Proc. IEEE **51** (1963), no. 3, 436–442.

[H+89] A. Hofmann et al., *Physical phenomena used in beam observation*, Frontiers of Particle Beams; Observation, Diagnosis and Correction, Lecture Notes in Physics, vol. 343, Springer Berlin / Heidelberg, 1989, pp. 367–379.

[H+12] M. Hansli et al., *Coupling methods for the highly sensitive cavity sensor for longitudinal and transverse schottky measurements*, Proceedings of BIW2012, Newport News, Virginia, USA (2012).

[Hel69] G. Helmberg, *Introduction to spectral theory in Hilbert space*, Amsterdam, London, 1969.

[Hel84] S. Helgason, *Groups and geometric analysis: Integral geometry, invariant differential operators, and spherical functions*, Academic Press, 1984.

[Hen85] H. Henke, *Charge passing off-axis through a cylindrical resonator with beam pipes*, IEEE Transactions on Nuclear Science **32** (1985), no. 5.

[Hen86] ———, *Point charge passing a resonator with beam tubes*, Electrical Engineering (Archiv fur Elektrotechnik) **69** (1986), no. 4, 271–277.

[Hen04] W. Henning, *FAIR-an international accelerator facility for research with ions and antiprotons*, Proceedings of EPAC, Lucerne, Switzerland **773** (2004), 3–5.

[Hsu10] H. P. Hsu, *Schaum's outline signals and systems*, McGraw-Hill, August 2010 (en).

[Hue92] P. Huelsmann, *Theoretische und experimentelle Untersuchungen zur Bestimmung der Transversalen Shuntimpedanz und Güte an störmodenbedämpften Beschleunigerresonatoren für lineare Kollider und Hochstrombeschleuniger im mittleren*

und hohen Energiebereichen, Ph.D. thesis, Johann Wolfgang Goethe-Universität, Frankfurt am Main, 1992.

[Hue01] ———, *Strahl-resonator-wechselwirkungen und deren geziehlte beeinflussung in linear collider-strukturen*, 2001.

[Isi24] G. Ising, *Prinzip einer Methode zur Herstellung von Kanalstrahlen hoher Voltzahl*, R. Friedländer & Sohn, 1924.

[Jac98] J. D. Jackson, *Classical electrodynamics third edition*, 3 ed., Wiley, August 1998.

[Joh28] J. B. Johnson, *Thermal agitation of electricity in conductors*, Physical Review **32** (1928), no. 1, 97–109.

[Jos10] Joseph, *iqtread.m*, 2010.

[KH11] O. Kester and P. Hülsmann, *Entwicklung von resonanten Pickups zur vollkinematischen Untersuchung von Reaktionen mit einzelnen gespeicherten Ionen*, 2011.

[KK64] O. A Kolpakov and V. I Kotov, *Radiation of a charge passing through a cylindrical cavity (Russian)*, Journal of Technical Physics **34** (1964), no. 8, 1387–1391.

[Kli10] H. Klingbeil, *Elektromagnetische feldtheorie: Ein lehr- und Übungsbuch*, 2 ed., Vieweg+Teubner, October 2010.

[Kra10] F. Krawczyk, *Private communication*, 2010.

[L$^+$05] Yu. A Litvinov et al., *Mass measurement of cooled neutron-deficient bismuth projectile fragments with time-resolved schottky mass spectrometry at the FRS-ESR facility*, Nuclear Physics A **756** (2005), no. 1-2, 3–38.

[Lam86] G. Lambertson, *Dynamic devices: Pickups and pickers*.

[Lam89] ———, *Electromagnetic detectors*, Frontiers of Particle Beams; Observation, Diagnosis and Correction (1989), 380–402.

[Law90] J. D. Lawson, *Radiation from a ring charge passing through a resonator*, Particle Accelerators, Gordon and Breach Science Publishers Inc. **25** (1990), 107–112.

[LB62] M. S. Livingston and J. P. Blewett, *Particle accelerators*, McGraw-Hill, 1962.

[LB11] Y. A Litvinov and F. Bosch, *Beta decay of highly charged ions*, Reports on Progress in Physics **74** (2011), 016301.

[Lew09] R. Lewallen, *RMS power*, 2009.

[Lin03] M. Lindroos, *Future plans at ISOLDE*, Nuclear Instruments and Methods in Physics Research Section B: Beam Interactions with Materials and Atoms **204** (2003), no. 0, 730–735.

[Lit03] Yu. A. Litvinov, *Basic nuclear properties of neutron-deficient nuclei investigated via high precision mass measurements in the element range of 36 $< z <$ 92*, Ph.D. thesis, Justus-Liebig Universität Gießen, Gießen, 2003.

[Lit08] S. Litvinov, *Investigation of the isochronous mode of the experimental storage ring (ESR) and the collector ring (CR). decay spectroscopy of highly charged stored 140Pr ions at the FRS-ESR facility*, Ph.D. thesis, Justus-Liebig Universitat Giessen, Gießen, 2008.

[Lit09] Yu. A. Litvinov, *Mass and lifetime measurement at the present ESR facility*, International Journal of Modern Physics E **18** (2009), no. 02, 323.

[LS70] P.M. Lapostolle and A.L. Septier, *Linear accelerators*, North-Holland, Amsterdam (1970).

[Lya12] J. R. Lyall, *Noise figure notes, EE 410 course schedule fall 2012*, http://pr.erau.edu/~lyallj/ee410/noise_fig.html, 2012.

[M$^+$79] D. Moehl et al., *Physics and technique of stochastic cooling*, Tech. Report CERN/PS/AA 79-23, July 1979.

[M$^+$89] D. Martin et al., *A resonant beam detector for tevatron tune monitoring*, Particle Accelerator Conference, 1989. Accelerator Science and Technology., Proceedings of the 1989 IEEE, 1989, p. 1486–1488.

[MFH54] P. M Morse, H. Feshbach, and E. L. Hill, *Methods of theoretical physics*, American Journal of Physics **22** (1954), 410.

[Mil05] J. Miles, *Cern accelerator school radio frequency engineering*, no. 3, CERN, 2005.

[MJS52] L. C. Maier Jr and J. C. Slater, *Field strength measurements in resonant cavities*, Journal of Applied Physics **23** (1952), no. 1, 68–77.

[Mor94] P. Morton, *Introduction to impedance for short relativistic bunches*, Frontiers of Particle Beams: Factories with e+ e-Rings (1994), 234–254.

[Mue39] J. Mueller, *Untersuchungen über elektromagnetische Hohlräume*, Zeitschrift für Elektrotechnik, Mitteilung aus dem Laboratorium der Telefunken G. m. b. H. (1939), 157–161.

[MV01] K. Meyberg and P. Vachenauer, *Hoehere Mathematik 2: Differentialgleichungen, Funktionentheorie, Fourier-Analysis, Variationsrechnung*, Springer, 2001 (de).

[N+00] F. Nolden et al., *Stochastic cooling at the ESR*, Nuclear Instruments and Methods in Physics Research Section A: Accelerators, Spectrometers, Detectors and Associated Equipment **441** (2000), no. 1–2, 219–222.

[N+05] P. Neumayer et al., *Status of PHELIX laser and first experiments*, Laser and Particle Beams **23** (2005), no. 03, 385–389.

[NHL+10] F. Nolden, P. Hülsmann, Yu. A. Litvinov, P. Moritz, C. Peschke, P. Petri, M. S. Sanjari, M. Steck, H. Weick, J.X. Wu, Y.D. Zang, S.H. Zhang, and T.C. Zhao, *A new resonant schottky pickup for the ESR at GSI*, 2010.

[NHL+11] ———, *A fast and sensitive resonant schottky pick-up for heavy ion storage rings*, Nuclear Instruments and Methods in Physics Research Section A (2011).

[Nol10] F. Nolden, *Private communication*, 2010.

[Nyq28] H. Nyquist, *Thermal agitation of electric charge in conductors*, Physical Review **32** (1928), no. 1, 110–113.

[P+03] L. Palumbo et al., *Wake fields and impedance*, Arxiv preprint physics/0309023 (2003).

[Pal87] R. B. Palmer, *A qualitative study of wake fields for very short bunches*, SLAC-PUB-4437 (1987).

[Pes95] C. Peschke, *Messungen und berechnungen zu longitudinalen und transversalen shuntimpedanzen einer elektronen-positronen- linearbeschleuniger-struktur*, 1995.

[Pes10] ———, *Private communication*, 2010.

[PP02] A. Papoulis and S. U. Pillai, *Probability, random variables, and stochastic processes*, 4th ed. international edition. ed., Mcgraw-Hill Publ.Comp., January 2002.

[PP05] W. K. H. Panofsky and M. Phillips, *Classical electricity and magnetism: Second edition*, 2 ed., Dover Publications, January 2005.

[Pur85] E. M. Purcell, *Electricity and magnetism*, vol. 2, McGraw-Hill, 1985.

[PW93] D. B. Percival and A. T. Walden, *Spectral analysis for physical applications: multitaper and conventional univariate techniques*, Cambridge University Press, 1993.

[R+73] S. Raman et al., *Energy levels in 142 nd*, Nuclear Physics A **201** (1973), no. 1, 21–40.

[R+00] T. Radon et al., *Schottky mass measurements of stored and cooled neutron-deficient projectile fragments in the element range of 57<=z<=84*, Nuclear Physics A **677** (2000), no. 1-4, 75–99.

[Ran87] R. B. Randall, *Frequency analysis*, 3 ed., Bruel & Kjaer, 1987.

[Roh07] F. Rohrlich, *Classical charged particles*, World Scientific, 2007 (en).

[RV68] A. G. Ruggiero and V.G. Vaccaro, *Solution of the dispersion relation for longitudinal stability of an intense coasting beam in a circular accelerator (application to the ISR)*, Rep. No. ISR-TH/68- Z (1968).

[S+06] D. Scott et al., *Longitudinal resistive wall wakefields for the ILC positron undulator vessel*.

[S+11] M. S. Sanjari et al., *Bead-pull measurement on the resonator pick-up at IMP, lanzhou*, 2011.

[S+12] ———, *A resonant schottky pickup for the study of highly charged ions in storage rings*, submitted to IOP Proceedings of 16th International Conference on the Physics of Highly Charged Ions, Heidelberg (2012).

[San10] C. A. Sanchez, *MTPSD library and octave extentions documentation*, http://www.eigenspectrum.com/, November 2010.

[Sch98] A. Schuster, *On the investigation of hidden periodicities with application to a supposed 26 day period of meteorological phenomena*, Terrestrial Magnetism **3** (1898), no. 1, 13–41.

[Sch18] W. Schottky, *Über spontane Stromschwankungen in verschiedenen Elektrizitätsleitern*, Annalen der Physik **362** (1918), no. 23, 541–567.

[Sch91] U. Schaaf, *Schottky-Diagnose und BTF-Messungen an gekühlten Strahlen im Schwerionen-Speicherring ESR*, Ph.D. thesis, Johann Wolfgang Goethe-Universität, Frankfurt am Main, 1991.

[Sch97] B. Schlitt, *Schottky mass spectrometry at the heavy ion storage ring ESR*, Ph.D. thesis, Ruprecht - Karls - Universität Heidelberg, Heidelberg, 1997.

[Shi92] T. Shintake, *The choke mode cavity*, Japanese Journal of Applied Physics **31** (1992), no. Part 2, No. 11A, L1567–L1570.

[Shu12] D. Shubina, *Schottky mass measurements of heavy neutron-rich nuclides in the element range 70<= z <=79 at the ESR*, Ph.D. thesis, Ruprecht - Karls - Universität Heidelberg, Heidelberg, 2012.

[Sim93] K. Simonyi, *Theoretische Elektrotechnik*, 10 ed., Wiley-VCH, September 1993.

[Sla46] J. C. Slater, *Microwave electronics*, Reviews of Modern Physics **18** (1946), no. 4, Page 81.

[Sle78] D. Slepian, *Prolate spheroidal wave functions, fourier analysis, and uncertainty. v-the discrete case*, AT T Technical Journal **57** (1978), 1371–1430.

[Ste66] C. W Steele, *A nonresonant perturbation theory*, IEEE Transactions on Microwave Theory and Techniques **14** (1966), no. 2, 70–74.

[Tay91] C. S. Taylor, *Microwave kickers and pickups*.

[Tec10] Agilent Technologies, *Fundamentals of RF and microwave noise figure measurements, application note 57-1*, 2010.

[Tek08] Tektronix, *Tektronix RTSA matlab functions*, 2008.

[Tho82] D. J Thomson, *Spectrum estimation and harmonic analysis*, Proceedings of the IEEE **70** (1982), no. 9, 1055–1096.

[Tho11] L. Thorndahl, *Private communication*, February 2011.

[Tul00] J.K. Tuli, *Nuclear data sheets for a = 142*, Nuclear Data Sheets **89** (2000), no. 3, 641–796.

[Ung89] H.-G. Unger, *Elektromagnetische Theorie für die Hochfrequenztechnik: Kugelwellen, Feldentwicklungen, Störungs- u. Variationsverfahren, Mikrowellenkreise.*, 2 ed., vol. 2, Hüthig, 1989.

[Ung02] ———, *Elektromagnetische Theorie für die Hochfrequenztechnik: Allgemeine Gesetze und Verfahren, Antennen und Funkübertragung*, 2 ed., vol. 1, Hüthig, 2002.

[Uns92] K. B. Unser, *The parametric current transformer, a beam current monitor developed for LEP*, AIP Conference Proceedings, vol. 252, 1992, p. 266.

[Wan08] T.P. Wangler, *RF linear accelerators*, Wiley Online Library, 2008.

[Wan11] R. Wang, *Quality factor, peak frequency and bandwidth*, http://fourier.eng.hmc.edu/e84/lectures/ch3/node7.html, 2011.

[Web00] R. C. Webber, *Tutorial on beam current monitoring*, AIP Conference Proceedings, vol. 546, 2000, p. 83.

[Web10] R. Weber, *Email correspondance, FRIATEC AG*, 2010.

[Wei08] T. Weiland, *Skriptum zu Teschnische Elektrodynamik*, 2008.

[WG82] P. B Wilson and J. E Griffin, *High energy electron linacs application to storage ring RF systems and linear colliders*, American Institute of Physics Conference Series, vol. 87, 1982, p. 450–555.

[Wil74] P.B. Wilson, *Beam loading in high-energy storage rings*, Proc. IXth Int. Conf. High Energy Accelerators (Stanford, USA, 1974), vol. 57, 1974.

[Wil78] P. B. Wilson, *Transient beam loading in electron-positron storage rings*, PEP Note-276, Dec (1978).

[Wil89] ———, *Introduction to wakefields and wake potentials*, SLAC-PUB-4547 (1989).

[Wil96] K. Wille, *Physik der Teilchenbeschleuniger und Synchrotronstrahlungsquellen. Eine Einführung*, 2., überarb. u. erw. a. ed., Teubner Verlag, 1996.

[Win09] N. Winckler, *Nuclear orbital electron capture of stored highly-ionized 140Pr and 142Pm ions*, Ph.D. thesis, Justus-Liebig Universität Gießen, Gießen, 2009.

[Wol87] H. Wollnik, *Laterally and longitudinally dispersive recoil mass separators*, Nuclear Instruments and Methods in Physics Research Section B: Beam Interactions with Materials and Atoms **26** (1987), no. 1–3, 267–272.

[WW92] T. Weiland and R. Wanzenberg, *Wake fields and impedances*, Frontiers of Particle Beams: Intensity Limitations (1992), 39–79.

[X+02] J. W. Xia et al., *The heavy ion cooler-storage-ring project (HIRFL-CSR) at lanzhou*, Nuclear Instruments and Methods in Physics Research Section A: Accelerators, Spectrometers, Detectors and Associated Equipment **488** (2002), no. 1-2, 11–25.

[Y+08] Y. Yamaguchi et al., *Rare-RI ring project at RIKEN RI beam factory*, Nuclear Instruments and Methods in Physics Research Section B: Beam Interactions with Materials and Atoms **266** (2008), no. 19–20, 4575–4578.

[Z+11] Y.D. Zang et al., *Simulation and measurement of the resonant schottky pickup*, Chinese Physics C **35** (2011), no. 12, 1124–1129.

[ZK98] B. W. Zotter and S. A. Kheifets, *Impedances and wakes in high-energy particle accelerators*, World Scientific, June 1998 (en).

[ZO04] F. Zimmermann and K. Oide, *Resistive-wall wake and impedance for nonultrarelativistic beams*, Physical Review Special Topics - Accelerators and Beams **7** (2004), no. 4, 044201.

[Zou10] A. M. Zoubir, *Manuscript digital signal processing*, 2010.

Acknowledgements

This work would not have been possible without help and guidance of many individuals that contributed to the project in different ways.

I am thankful to Prof. Dr. Alwin Schempp for accepting me as PhD student and for his support, recommendations and constructive criticism.

I would like to thank PD Dr. Peter Hülsmann for his encouragement, guidance and wise supervision that he provided throughout the course of this work. Many of my efforts would have been in vain without his insightful comments.

I express my sincerest gratitude to PD Dr. Yuri Litvinov for his invaluable scientific advices and for involving me in storage ring experiments.

I am grateful to Prof. Dr. Fritz Bosch for the scientific insights that he shared and for all the patience he had with my diverse questions in astrophysics and cosmology.

I thank Dr. Nicolas Winckler for his teachings in advanced topics of mathematics and for the explanation of statistical methods. Dr. Daria Shubina for her outstanding help with the experimental data of the 2010 beam time and for philosophical discussions at the coffee time.

It gives me pleasure to acknowledge Dipl.-Ing. Peter Petri for his unfailing help and support in construction of electronics, Dr. Fritz Nolden for his help in multitaper analysis and coordination of the project and Prof. Dr.-Ing. Harald Klingbeil for his recommendations and his support as a member of my HGS-HIRe PhD committee.

I acknowledge Mr. Michael Sam for his bright and practical ideas and assistance in preparing mechanical prototypes and Dipl.-Ing. Ina Schurig for her precious help with the mechanical design of the resonator.

I am thankful to members of the RF and ESR department, especially Dipl. Ing. Peter Moritz for his explanations on RF devices, Dr. Claudius Peschke for his explanations on noise and related RF concepts, Dipl. Ing. Michal Zelensky for his explanations on mechanical constructions, Dr. Klaus-Peter Ningel for his concern about me and Dipl. Ing. Robert Balß, Dipl.-Ing. Rainer Hettrich, Dipl.-Ing. Wolfgang Maier, Dipl. Ing. Stefan Schäfer, Dr. Markus Steck, Prof. Dr. Thomas Stöhlker and Dipl. Ing. Christoph Thielmann for providing a pleasant working atmosphere.

I thank Dipl. Phys. Pierre-Michel Hillenbrand, Prof. Dr. Robert DuBois, Dr. Siegbert

Hagmann, Dr. Günter Weber, Dr. Danyal Winters and Dr. Michael Bussmann for their invaluable help during the beam time of Aug 2012.

I am grateful to Prof. Dr. XinWen Ma and his colleagues at Institute of Modern Physics (IMP) for inviting me to Lanzhou in August 2011 and their hospitality, in particular Dr. JunXia Wu, Dr. YongDong Zang, Dr. XiaoLin Tu, Mr. XinLiang Yan from Institute of Modern Physics, Mr. ChenLei Guo from Beihang University, Beijing, and Dr. MinJin Ma from University of Lanzhou.

Many thanks goes to the administrators of Helmholtz Graduate School for Hadron and Ion Research (HGS-HIRe) for the perfect coordination of courses and the structured PhD studies: Prof. Dr. Henner Büsching, Ms. Johanna Dilley, Ms. Helena Correa dos Santos, Ms. Sylke Schneider, Dr. Sascha Vogel and particularly Dr. Gerhard Burau for his special concern regarding my academic requirements and for the "Snowball fight"!

I thank my brother Dr. Mohammad Ali Sanjari for his explanations on non-linear dynamical systems and chaos, Dipl.-Inf. Siniša Đukanović for his comments on computer programming and Dipl.-Ing. Christian Fiederling for reviewing the German abstract.

I am thankful to my mother for her patience and my father for his encouragements.

I dedicate this work to my wife, Marina. I appreciate her help with the translation of the Russian paper [KK64], but above all, I am thankful for her patience and support during the preparation of this thesis and her loving care for our two daughters.

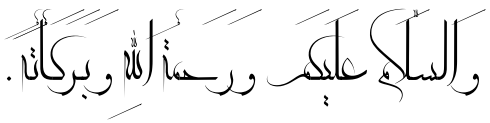

Peace and God's blessings be upon you.

Academic Tutors

Goethe Universität Frankfurt am Main

Professors

H. Appelshäuser, H. Büsching, B. Deiss, C. Greiner, P. Hülsmann , H.-J. Lüdde, U. Müller-Nehler, O. Philipsen, D. Rischke, A. Schempp, S. Schramm, K. Sonnabend, J. Stroth and J. Struckmeier.

Helmholtz Graduate School

Professors

K. Blaum, Yu. A. Litvinov, M. Pignatari, H. Simon, A. Surzhykov and D. Winters.

Technische Universität Darmstadt

Professors

H. Alber, H. Eveking, H. Geschka, M. Glesner, R. Jakoby, A. Klein, H. Klingbeil, U. Konigorski, P. Meissner, M. Mühlhäuser, D. Pavlidis, S. Roch, H. Schlaak, A. Schürr, U. Schwalke, R. Steinmetz, T. Weiland, H. Wipf and A. M. Zoubir.